NUMERICAL PREDICTION OF TURBULENT GAS-SOLID AND LIQUID-SOLID FLOWS USING TWO-FLUID MODELS

A Thesis

Submitted to the College of Graduate Studies and Research

in Partial Fulfillment of the Requirements for the Degree of

Master of Science

in the Department of Mechanical Engineering at the

University of Saskatchewan

Saskatoon, Canada

By

Ajay Kumar Yerrumshetty

PERMISSION TO USE

In presenting this thesis in partial fulfillment of the requirements for a Master of Science degree from the University of Saskatchewan, I agree that the Libraries of this University may make it freely available for inspection. I further agree that permission for copying this thesis in any manner, in whole or in part, for scholarly purposes may be granted by the professor or professors who supervised my thesis work or, in their absence, by the Head of the Department or the Dean of the College in which my thesis work was done. It is understood that any copying, publication, or use of this thesis or parts thereof for financial gain shall not be allowed with out my written permission. It is also understood that due recognition shall be given to me and to the University of Saskatchewan in any scholarly use which may be made of any material in my thesis.

Requests for permission to copy or to make other use of material in this thesis in whole or part should be addressed to:

Head of the Department of Mechanical Engineering
University of Saskatchewan
Engineering Building, 57 Campus Drive
Saskatoon, Saskatchewan S7N 5A9
Canada

ABSTRACT

The prediction of two-phase fluid-solid (gas-solid and liquid-solid) flow remains a major challenge in many engineering and industrial applications. Numerical modeling of these flows is complicated and various studies have been conducted to improve the model performance. In the present work, the two-fluid model of Bolio *et al*. (1995), developed for dilute turbulent gas-solid flows, is employed to investigate turbulent two-phase liquid-solid flows in both a vertical pipe and a horizontal channel.

Fully developed turbulent gas-solid and liquid-solid flows in a vertical pipe and liquid-solid (slurry) flow in a horizontal channel are numerically simulated. The momentum equations for the fluid and solid phases were solved using the finite volume technique developed by Patankar (1980). Mean and fluctuating velocities for both phases, solids concentration, and pressure drop were predicted and compared with the available experimental data. In general, the mean velocity predictions for both phases were in good agreement with the experimental data for vertical flow cases, considered in this work.

For dilute gas-solid vertical flows, the predictions were compared with the experimental data of Tsuji *et al*. (1984). The gas-phase fluctuating velocity in the axial direction was significantly under-predicted while the results for the solids fluctuating velocity were mixed. There was no data to compare the solids concentration but the profiles looked realistic. The pressure drop was observed to increase with increasing Reynolds number and mass loading when compared with the data of Henthorn *et al*. (2005). The pressure

drop first decreased as particle size increased and then started increasing. This behaviour was shown by both experimental data and model predictions.

For the liquid-solid flow simulations the mean velocity profiles for both phases, and the liquid-phase turbulence kinetic energy predictions (for dilute flow case), were in excellent agreement with the experimental data of Alejbegovic *et al*. (1995) and Sumner *et al*. (1990). The solids concentration profiles were poorly predicted, especially for the lighter particles. The granular temperature profiles, accounting for the solids velocity fluctuations, for the dilute flow case failed to agree with the data, although they captured the overall trend. The liquid-solid pressure drop predictions, using the present model, were only successful for some particles.

The solids concentration predictions for the horizontal flow case were similar to the experimental measurements of Salomon (1965), except for a sharp peak at the bottom wall and the opposite curvature. The mixture velocity profiles were asymmetric, due to the addition of particles, and were similar to the experimental data, though only a partial agreement was observed between the predictions and the data.

A conclusion from this work is that the present model, which was developed for dilute gas-solid flows, is inadequate when liquid-solid flows are considered. Further improvements, such as including the interstitial fluid effects while computing the liquid-phase stress, are needed to improve the predictive capability of this two-fluid model.

ACKNOWLEDGEMENTS

I would like to express my earnest gratitude and appreciation to my respected supervisor, Dr. Donald J. Bergstrom, for his invaluable guidance, support and encouragement throughout my work during this graduate program. His critical appraisal and suggestions have been priceless at every stage of this research.

I would like to extend my acknowledgement to my advisory committee members Dr. J. D. Bugg, Dr. R. S. Sanders and Dr. D. Sumner for their valuable suggestions and feedback.

I take this opportunity to thank my research colleague F. N. Krampa-Morlu for his guidance and my friends, other colleagues and staff at the Department of Mechanical Engineering for making my stay at the University of Saskatchewan a memorable one.

Furthermore, I would like to thank Dr. Bergstrom, NSERC and Syncrude Canada Ltd. for providing the financial support for this research work.

DEDICATED TO

My parents, brother and sister for their unwavering guidance, support and motivation.

TABLE OF CONTENTS

LIST OF FIGURES

LIST OF TABLES

LIST OF SYMBOLS

c_s	Solids concentration/volume fraction
C_D	Drag coefficient
C_0	Solids concentration at closed packing (=0.65)
d_{p}	Particle diameter (mm)
D	Pipe diameter (mm)
e	Coefficient of restitution for particle-particle collisions
e_{w}	Coefficient of restitution for particle-wall collisions
f_g	Single-phase Fanning friction factor
F_{pw}	Solids pipe friction
g	Acceleration due to gravity (=9.81 ms^{-2})
H	Height of the channel (mm)
i_{m}	Frictional head loss for liquid-solid flow
k	Fluid-phase turbulence kinetic energy ($\mathrm{m}^2\mathrm{s}^{-2}$)
L	Length over which pressure measurement is made for a gas-solid flow (mm)
m	Mass loading
p	Pressure supplied to the fluid-phase
r	Radial co-ordinate
R	Radius of the pipe (mm)
Re	Pipe Reynolds number
Re_d	Particle Reynolds number
R_{t}	Turbulent Reynolds number
T	Granular temperature
u	Mean velocity (ms^{-1})
w	Total mass flow rate (kgs^{-1})
y	Wall-normal distance (mm)
z	Axial co-ordinate (mm)

Greek Symbols

β	Interphase drag correlation ($\mathrm{kgm^{-3}s^{-1}}$)
ε	Dissipation rate of the fluid-phase turbulence kinetic energy ($\mathrm{m^2s^{-3}}$)
ϕ	Specularity co-efficient
γ	Dissipation rate of granular temperature due to inelastic inter-particle collisions
μ	Dynamic viscosity ($\mathrm{kgm^{-1}s^{-1}}$)
ν	Kinematic viscosity ($\mathrm{m^2s^{-1}}$)
θ	Angle of inclination to the horizontal
ρ	Density ($\mathrm{kgm^{-3}}$)
σ	Stress in the particle phase ($\mathrm{kgm^{-1}s^{-2}}$)
τ	Stress in the fluid phase ($\mathrm{kgm^{-1}s^{-2}}$)

Subscripts

b	Bulk value
f	Fluid phase
m/mix	Mixture
r	Radial direction
s/p	Solid/particle phase
t	Turbulent
w	Wall
z	Axial direction

Superscripts

$\bar{}$	Mean part
/	Fluctuating part
~	Instantaneous part
+	Dimensionless form

1 INTRODUCTION AND LITERATURE REVIEW

1.1 Motivation

Two-phase flow refers to a system consisting of two different phases, such as gas and liquid, gas and solid or liquid and solid flowing together as a mixture. Although the two phases interact with each other, they usually have different velocities, densities, viscosities, etc. Two-phase turbulent flows, mainly gas-solid and liquid-solid flows, are relevant to many engineering and industrial applications including hydro-transport of slurries in pipelines, circulating fluidized beds, pneumatic transport of granular materials such as coal, and sediment transport in rivers. As a result of the inherent complexity of two-phase flows, numerical modeling of these flows is difficult. Predictions for the mean and fluctuating velocity and concentration fields for both phases along with pressure drop remain a major challenge. In recent years, considerable effort has been invested in the study of these flows in an attempt to improve predictive capability.

In this chapter, a general background on two-phase flow involving fluid and solid phases is presented. Select numerical studies by different research groups, along with the experimental data available to evaluate the model performance are discussed. An in-house algorithm was used to analyze the gas-solid and liquid-solid flows in this work; the reasons for preferring an in-house algorithm over commercial software are also

discussed. Finally, a statement of the thesis objectives, scope and methodology are presented.

1.2 Two-phase flow

As noted above, two-phase flow refers to a system containing two different kinds of coexisting matter, for example gas-liquid, gas-solid and liquid-solid flows. The present research considers only gas-solid and liquid-solid flows. Models for such flows can be classified as follows (Comer, 1998):

1. Mixture model
    a. Homogeneous model
    b. Drift flux model
2. Separated model
    a. Two-fluid model (Eulerian-Eulerian)
    b. Particle trajectory model (Eulerian-Lagrangian)

Among these models, the Eulerian-Eulerian two-fluid model has been widely employed for two-phase flow analysis. As reported by Anderson and Jackson (1967), the flow becomes more complicated when dense fluid-solid flows, i.e. flows with high particle-concentration, are considered. Hence, they proposed a technique in which the point variables of the fluid and particle phases were replaced by their local mean averages and the particle phase was treated as a fluid-like phase. This approach, where the fluid and the particle phases are treated as interpenetrating continua with interactions between them is known as the two-fluid model. In this formulation, the micro-scale interfacial structure is not considered, and both the phases co-exist and occupy a fraction of the

total volume. In most cases, the two phases have different velocities, densities and concentrations. A number of models (e.g. Bolio *et al.*, 1995 and Zhang and Reese, 2003) for dilute fluid-solid flows have been developed using the two-fluid model. In these models, the momentum equations for the disperse phase (i.e. particles) are written in a form similar to the momentum equations for the fluid phase.

1.3 Numerical and experimental studies

Numerical modeling of two-phase fluid-solid flows is complicated and remains a major challenge for engineers. Extensive research has been carried out in an attempt to more accurately predict such features as the mean and fluctuating velocity and concentration for both phases and pressure gradient. Additional complexity due to inter-particle collisions is introduced when dense particulate flows are considered. A granular flow model, which is analogous to kinetic theory of molecular collisions, is often employed to account for the particle-particle and particle-wall collisions.

1.3.1 Mean and fluctuating velocity

The application of kinetic theory for a gas-solid flow was first used by Sinclair and Jackson (1989). They investigated fully developed laminar gas-solid flows with inter-particle and particle-wall collisions in a vertical tube. Solid-phase stresses were modelled from granular kinetic theory by treating the particle-phase as a rapid granular flow and forming an analogy with kinetic theory of dense gases. Note that even though the flow is laminar, there are fluctuations in the particle phase, due to inter-particle and

particle-wall collisions. Sinclair and Jackson (1989) predicted velocity profiles for both phases over a wide range of concentrations and volume flow rates. However, laminar flows rarely occur; instead the majority of flows encountered in real-life situations are turbulent in nature. Hence, efforts were made to study the turbulent flow behaviour.

Louge *et al*. (1991) extended the laminar flow model of Sinclair and Jackson (1989) by including turbulence in the gas-phase. A high Reynolds number, one-equation turbulence closure was employed for the gas-phase and a turbulent gas-solid flow for low particle concentrations was modelled. The mean velocities for both phases and the fluctuating velocity for the gas phase were predicted. The simulation results were compared with the experimental data of Tsuji *et al*. (1984) who measured the mean and fluctuating velocities of a gas-solid flow in a vertical pipe using Laser-Doppler Velocimetry (LDV). They transported polystyrene spheres ($\rho_s = 1020\,\mathrm{kgm}^{-3}$) of sizes ranging from $200\,\mu\mathrm{m}$ to 3 mm in a vertical glass pipe of diameter 30.5 mm. Reasonable agreement was found to exist between the predictions and the data for the mean velocity profiles, but the gas-phase fluctuating velocities significantly under-predicted the experimental data.

Bolio *et al*. (1995) further expanded on the work of Louge *et al*. (1991) and incorporated a two-equation, low Reynolds number $k-\varepsilon$ model originally developed for single-phase flow by Myong and Kasagi (1990). Their model was modified to include the effect of the particle-phase and was used to calculate the gas-phase turbulence. The selection of this particular model was based on the study of Hrenya *et al*. (1995), who

compared ten different low Reynolds number turbulence models for single-phase flows and indicated that the best predictions for a fully developed flow case were obtained with the $k-\varepsilon$ turbulence model of Myong and Kasagi (1990). As before, the solids-phase stresses were calculated from granular kinetic theory where, the solids phase is also considered as a continuum and described with Navier-Stokes equations.

Simulations for a dilute upward flow of a gas-solid mixture were performed, and the mean and fluctuating velocities for both phases were analysed. The effects of particle size and mass loading on the velocity profiles (mean and fluctuating) were examined and the predictions were compared with the experimental measurements of Lee and Durst (1982) and Tsuji *et al*. (1984); both the experiments were performed using LDV. Lee and Durst (1982) conducted experiments in a vertical glass pipe of diameter 41.8 mm for glass particles of density $\rho_s = 2590\,\mathrm{kgm}^{-3}$ while Tsuji *et al*. (1984) transported polystyrene particles of different sizes with density $\rho_s = 1020\,\mathrm{kgm}^{-3}$ in a vertical glass pipe of diameter 30.5 mm. The numerical simulation results compared reasonably well with the experimental data except for the turbulence intensity predictions of the gas-phase. The fluctuating velocities of the gas-phase were significantly under-predicted compared to the data for all flow conditions.

Turbulence in two-phase flow determines the extent of mixing and hence the transfer of momentum and thermal energy in the fluid phase. However, the presence of particles can alter the overall level and structure of the fluid-phase turbulence. This process is known as turbulence modulation. The effect of particles is accounted for via the drag

force term in the fluid-phase momentum equation, and the turbulence interphase term in the turbulence model equations. A strong influence of particles exists on turbulence when the mean solids concentration is greater than 10^{-3}. Elgobashi (1991) indicated that under these conditions, particle-particle collisions take place and the particle regime depends on the turbulence and also alters it. Also, many experimental (e.g. Tsuji *et al.*, 1984) and numerical studies (Zhang and Reese, 2001 & 2003) have shown that larger particles, i.e. particles with large particle Reynolds number ($Re_d \geq 70$), cause an additional production of turbulence kinetic energy, while particles with smaller Reynolds numbers increase the dissipation of turbulence kinetic energy.

According to Bolio and Sinclair (1995), the model of Bolio *et al*. (1995) failed to capture the experimental gas-phase turbulence kinetic energy because of the presence of only dissipative terms, due to particle drag, in their turbulence model equations. An alternative model which depends on the mean slip velocity was proposed by Yuan and Michaelides (1992). It assumes that particle wakes are responsible for turbulence augmentation while the turbulence is attenuated by the work done on the particles by the fluid-phase. Bolio and Sinclair (1995) investigated turbulence modulation using the mechanistic model of Yuan and Michaelides (1992) in the turbulence model equations, but retained the model of Bolio *et al*. (1995) for all the remaining terms. They predicted turbulence augmentation for larger $500\,\mu m$ particles, but failed to reproduce the observed augmentation for the smaller $200\,\mu m$ particles at higher mass loadings.

Following Koch (1990), Sinclair and Mallo (1998) replaced the turbulence interaction closure used in the model of Bolio *et al*. (1995), with an expression that depends on the local fluctuating velocity of the gas and particle phases, i.e. the turbulence kinetic energy and granular temperature, respectively. They also argued that studies which compared their numerical predictions with the experimental data of Tsuji *et al*. (1984) could be misleading since the measurements for the fluid-phase velocity fluctuations were made only in the stream-wise direction. Sinclair and Mallo (1998) compared their predictions with the experimental data of Sheen *et al*. (1993) who measured the gas-phase velocity fluctuations in both the stream-wise and radial directions. Sheen *et al*. (1993) carried out their experiments in a 52 mm ID vertical stainless steel pipe for polystyrene particles of sizes ranging from 225 to 800 μm using LDA. The measurements of Sheen *et al*. (1993) illustrate that significant anisotropy exists in the fluctuating velocity components.

The two-fluid model studies of Bohnet and Treiesch (2003), Cao and Ahmadi (1995) and Zhang and Reese (2001, 2003) have all considered turbulence modulation. Crowe and co-workers (Crowe, 2000, Kenning and Crowe, 1997 and Gore and Crowe, 1989) argued that the deficiency in predicting the turbulence modulation lies in the manner in which the transport equation for the turbulence kinetic energy is derived. A study of turbulence modulation in the context of a two-fluid model approach using three different models (Bolio and Sinclair, 1995, Sinclair and Mallo, 1998 and Zhang and Reese, 2001) was performed by Krampa-Morlu *et al*. (2006). They reported that the modified model of Zhang and Reese (2001) was able to reproduce much of the observed turbulence modulation.

An improved two-fluid model was proposed by Hadinoto *et al*. (2004). They expanded the work of Bolio *et al*. (1995) by including interstitial fluid effects on the random particle motion in addition to particle wake effects. Improved model predictions for the mean and fluctuating velocities for the gas-solid flows were obtained by Hadinoto *et al*. (2004).

Most of the existing numerical studies have investigated turbulent gas-solid flows (e.g. Bolio *et al*., 1995, Cao and Ahmadi, 1995 and Zhang and Reese, 2003). In comparison, very few studies have concentrated on liquid-solid flows e.g. Ding *et al*. (1993), Krampa-Morlu *et al*. (2004) and Hadinoto *et al*. (2004). Hadinoto *et al*. (2004) investigated liquid-solid flow in a vertical pipe and compared the predictions with the experimental data of Alejbegovic *et al*. (1994) for solids concentrations ranging from approximately 1% to 4%. Their measurements were made for co-current up-flow of a mixture of water and ceramic and expanded polystyrene particles (of spherical shape with a diameter of approx. 2 mm) in vertical pipe of diameter 30.6 mm. The ceramic particles ($\rho_s \approx 2443\,\mathrm{kgm}^{-3}$) were heavier than water ($\rho_s = 997\,\mathrm{kgm}^{-3}$) while the expanded polystyrene particles ($\rho_s \approx 32\,\mathrm{kgm}^{-3}$) were lighter. The mean and fluctuating velocities for the liquid phase were in good agreement with the experimental data, while the solids-phase velocity was under-predicted and the solids fluctuating velocity was significantly over-predicted. The work of Krampa-Morlu *et al*. (2004) concentrated on cases where the solids volume fraction was 10% and more. The numerical simulation results were compared with the data of Sumner *et al*. (1990) who measured the mean

solids velocity and concentration for five different particles transported through vertical acrylic plastic pipes of diameters 25.8 and 40 mm, at concentrations ranging from 10 – 50%. The mean solids-phase velocities were in good agreement with the experimental data while the solids volume fraction predictions were mixed.

Experimental measurements of liquid-solid flows in horizontal channels were performed by Salomon (1965). A horizontal flow is much different from a vertical flow. For example, the flow is axi-symmetric with respect to velocity and concentration for both phases for a vertical orientation whereas the horizontal flow is asymmetric. Also, the body force term appears in the wall-normal momentum balance for a horizontal flow, while for the vertical flow case, it appears in the axial momentum balance.

Salomon (1965) reported the distribution of solid particles ranging in diameter from 1.58 mm to 2.03 mm and densities of 2632 to 10,838 kgm^{-3} transported in a horizontal rectangular channel. The mixture velocities were measured by the use of a "flow divider", as described by Salomon (1965), at different heights above the channel bed. The flow divider separates the flow into two streams, and the values of mixture velocity were determined by measuring the volume flow rate of the lower stream at different heights above the channel bed. The solids concentration was measured using a gamma-ray densitometer. The study presents a large database of experimental data for the distribution of mixture velocity and solids concentration along the channel cross-section. A packed bed resulted when bulk mixture velocities were very low, i.e. of the order

$0.40\,\mathrm{ms}^{-1}$ and for solid particles with high density (e.g. nickel with density 8874 kgm^{-3} and lead with density 10,838 kgm^{-3}).

1.3.2 Pressure drop

For designing solid transport systems such as fluidized beds and hydro-transport of slurries in pipelines, knowledge of the pressure drop is required. A minimum value of pressure drop that ensures effective transport of particles without settling is preferred.

A number of studies, both numerical and experimental, have been performed to analyse pressure drop. Recently, Henthorn *et al*. (2005) investigated pressure drop for a gas-solid flow in a vertical pipe for a variety of flow conditions. They studied the effects of Reynolds number, mass loading, particle size and particle shape on the pressure drop predictions using both experimental and numerical studies. Encouraging predictions for the pressure drop were presented, and further improvements related to such issues as particle shape, solids stress models for highly nonspherical particles and the behaviour of gas-phase in particle wakes at high particle Reynolds numbers were suggested.

The pressure drop was observed to increase with increasing mass loading and Reynolds number according to the observations made by Konno and Saito (1969) and Singh (1982). However, Marcus *et al*. (1990) and Klinzing (1981) indicated (as mentioned in Henthorn *et al*., 2005) that the pressure drop may reduce initially with increasing mass loading for particles ranging in size from 20 to $75\,\mu\mathrm{m}$ for a mass loading between 0.5 and 4.0 and Reynolds number between 15,000 and 40,000. Henthorn *et al*. (2005)

attributed this decrease in pressure drop to the interaction of particles with turbulent eddies which results in the reduction of the gas-phase stresses. This is an important issue to consider in analyses of model performance.

Nieuwland *et al.* (1997) showed that for glass spheres ranging in size from 275 to $655\,\mu m$, the pressure drop increased with increasing particle size. A similar observation was also made by Wang *et al.* (2000). They observed that the pressure drop increased with increasing particle size at higher Re (>12,500), but decreased at lower Re.

The effect of particle-phase density on the pressure drop was investigated by Plasynski *et al.* (1994). They transported solid particles of different densities (glass beads and coal particles of densities 2400 and $1200\,kgm^{-3}$, respectively) through a gas medium in a vertical pipe. Their data showed that the pressure drop for the higher density particles was only slightly higher than that for lower density particles. According to Plasynski *et al.* (1994), flow parameters such as solids velocity, friction and volume fraction were responsible for this small difference in pressure drop, although the density difference was quite large (factor of 2).

Two-phase liquid-solid flow pressure gradient analysis was reported in detail by Shook and Bartosik (1994) and Matousek (2002). The pressure gradients for different particles with different sizes and concentrations were measured in vertical pipes for two different diameters (26 and 40 mm) by Shook and Bartosik (1994). They reported that pressure gradients increase with increasing particle diameter, density, concentration and mean

flow velocity. It was also shown that the increase in pressure gradient with solids concentration is non-linear. Matousek (2002) conducted experiments in a 150 mm pipe for three different orientations (vertical, horizontal and -35^{o} descending) and transported sand particles of sizes 0.12, 0.37 and 1.85 mm. The distribution of mean mixture velocity and solids concentration and the frictional pressure drop were measured for the transport of individual particles and mixtures of two particles. They concluded that a suspended flow resulted when 0.12-mm particles were transported in a horizontal pipe at velocities above the bed deposition limit. The flow for 0.37-mm particles was partially stratified (deposited) at lower velocities (closer to the deposition limit threshold) and fully suspended at higher solids velocities.

A review of the literature suggests that the investigation of fully developed gas-solid flows has been successful in vertical pipes. The mean and fluctuating velocities for both phases and pressure drop were predicted that were in good agreement with experimental data. The physics of turbulence modulation, i.e. augmentation and attenuation is unclear and needs to be addressed. Note that the solution procedure for developing flows is quite different compared to that for the fully developed flow case. Most existing studies investigated dilute gas-solid flows for a limited range of bulk solids concentrations. In comparison, relatively fewer studies have considered liquid-solid flow analysis in vertical pipes. The models used for the liquid-solid flow analysis have been unable to reproduce the profiles shown by the experimental measurements. The behaviour of the solids concentration and granular temperature is still not understood. Very little modeling work has been done for two-fluid modeling of dense horizontal flows.

1.4 Objectives

The overall goal of this research is to investigate the application of existing two-fluid models for vertical and horizontal liquid-solid flows. This is part of a larger research program funded by an NSERC CRD grant supported by Syncrude Canada Limited. More specifically, the objectives of this research are:

1. To develop an in-house algorithm for predicting fully-developed turbulent flows for dense coarse particle slurry (liquid-solid flows) in a vertical pipe and a horizontal channel;
2. Assess the model performance by comparing the liquid-solid flow predictions with the experimental data from the literature (Salomon, 1965, Sumner *et al.*, 1990, and Shook and Bartosik, 1994);
3. It is not expected that the present models will be able to predict the horizontal flow case. One of the contributions of the present study will be to identify deficiencies in the model used for the horizontal channel flow cases, and propose the next step towards obtaining better predictions.

1.5 Advantages of an in-house algorithms

In this research, an in-house algorithm was preferred over commercial software since it has certain advantages. The user has significantly more control over the program with an in-house algorithm than with commercial Computational Fluid Dynamics (CFD) software such as CFX and FLUENT. Details regarding implementation of the boundary conditions employed in commercial software are often not known; furthermore, some boundary conditions are pre-defined and cannot be altered. An in-house algorithm is far

more flexible. This does not imply that commercial software is not useful. At this stage of the research, the advantages of an in-house algorithm are emphasized over the commercial software from the viewpoint of readily implementing new models and solution techniques.

Contribution of the author

A single-phase flow code with a low Reynolds number $k-\varepsilon$ turbulence model was provided. The code was extended by the author to consider two-phase gas-solid and liquid-solid flows in vertical pipes and horizontal channels.

1.6 Approach

The first step towards the development of a computational code for predicting turbulent slurry flow is to understand the underlying principles and the physics of the flow. This was followed by solving a fully developed single phase turbulent duct flow using the low Reynolds number (LRN) $k-\varepsilon$ model of Nagano and Tagawa (1990). This was done in order to gain some knowledge and experience of turbulence and its modelling, and to understand the code originally written by Prof. D. J. Bergstrom. An alternative two equation model ($k-\omega$ model of Wilcox, 1993) was also implemented as an exercise in understanding the algorithm and modifying the code. Predictions were obtained for both models, i.e. the LRN $k-\varepsilon$ model of Nagano and Tagawa (1990) and the $k-\omega$ model of Wilcox (1993).

The next step in developing the algorithm was to solve fully developed two phase gas-solid flow involving particle-particle interactions and fluid phase turbulence (Bolio *et al*., 1995). First, a fully developed two phase laminar flow with particle-particle interactions (Sinclair and Jackson, 1989) was studied, to avoid any complication due to turbulence. Many of the equations were non-linear and therefore still challenging to solve. The laminar flow was solved and the predictions of Sinclair and Jackson (1989) were reproduced.

The laminar flow model was then extended to consider a turbulent flow case, following the dilute gas-solid flow model of Bolio *et al*. (1995), by solving additional transport equations for turbulence and modifying the laminar flow model equations to include turbulence. The turbulent flow model predictions were compared to the experimental data of Lee and Durst (1982) and Tsuji *et al*. (1984), as well as the predictions of Bolio *et al*. (1995).

The next step was to solve liquid-solid flow in a vertical pipe using the two-fluid model of Bolio *et al*. (1995). The predictions for the liquid-solid flow were compared with the experimental measurements of Alejbegovic *et al*. (1994) and Sumner *et al*. (1990).

The final step in this work was to investigate liquid-solid flow in a horizontal channel. The momentum equations for both phases were modified for horizontal flow. The closure expressions for the solids-phase stress and granular temperature were adopted from the dilute gas-solid flow model of Bolio *et al*. (1995) with the turbulence

interaction closure of Sinclair and Mallo (1998). The predictions were compared with the data of Salomon (1965).

1.7 Scope of this work

In the present work, fully developed two-phase gas-solid and liquid-solid flow cases were investigated, in vertical pipes and horizontal channels using limited number of models. This research mainly focuses on the models of a single group (Sinclair). Gas-solid flow was predicted in vertical pipe for dilute cases whereas liquid-solid flow was predicted in vertical pipes and horizontal channels. An investigation of pressure drop was also carried out for gas-solid and liquid-solid flows in vertical pipes.

1.8 Outline of thesis

The model equations for both phases along with the closures and boundary conditions and the numerical solution procedure are described in Chapter 2. In Chapter 3, gas-solid flow in vertical pipes is considered. Predictions for the mean and fluctuating velocity for both phases and pressure gradient analysis are reported. Liquid-solid flows in vertical pipes are discussed in Chapter 4. The distribution of the mean and fluctuating velocities for both phases and solids concentration profiles across the pipe cross-section are presented. Chapter 5 discusses horizontal channel flows for liquid-solid mixtures for different sand particles and solids concentrations. The experimental measurements used to assess the model predictions are also discussed for each flow in their respective

chapters. A summary of the research, conclusions, some deficiencies of the present model and steps to improve the predictions (future work) are reported in Chapter 6.

2 MODEL EQUATIONS AND SOLUTION METHOD

This chapter presents the mathematical model equations governing fluid-solid flows and their solution procedure for fully-developed vertical duct flow. In the context of this work, gas-solid flows were first investigated followed by liquid-solid flows. The flow is steady, incompressible, fully-developed vertical duct flow.

2.1 Model equations

This section presents the transport equations for the fluid-phase axial momentum balance and turbulence model equations, particle-phase axial and radial momentum balance, and a separate transport equation for the granular temperature which accounts for the particle-phase stresses. The various closure coefficients and boundary conditions used in the model are also discussed in detail. In general, the fluid-phase satisfies the Navier-Stokes equations at each point, while the particle-phase (i.e. each particle) satisfies the Newtonian equation of motion. In the two-fluid models considered, the fluid and particle phases are treated as inter-penetrating continua with interactions between them. A two-fluid fluid-particle flow is typically described by continuity and momentum conservation equations for both phases, and a separate transport equation for the granular temperature which includes particle-phase stresses. The continuity and momentum equations are given below.

2.1.1 Continuity equations

For steady flow, the continuity equations for both the phases are written as follows:

Fluid phase

$$\rho_f \frac{\partial(c_f u_f)_i}{\partial x_i} = 0 \tag{2.1}$$

Solid phase

$$\rho_s \frac{\partial(c_s u_s)_i}{\partial x_i} = 0 \tag{2.2}$$

In the above equations, u_f and u_s, ρ_f and ρ_s, and c_f and c_s are the fluid- and the particle-phase velocities, densities and concentrations, respectively.

For the flow conditions assumed in this work, i.e. steady and fully developed flow, the continuity equations for both the phases are satisfied. The continuity equations are not used explicitly to calculate the solids concentration since the flow is fully developed. Instead, the momentum equation for the solids phase in the radial direction is used to compute the solids concentration. Note that this is not possible for developing flow.

2.1.2 Momentum equations

The momentum equations for the fluid and solid phases are written following Bolio *et al.* (1995) based on the assumptions given in the previous section. The fluid parameters such as velocity, concentration, etc., in the momentum equations for both phases are time averaged so that the instantaneous values of the parameters are replaced by their

local mean values. For example, if velocity is considered, then the instantaneous value of the velocity is expressed as,

$$\tilde{u}_i = u + u_i' \tag{2.3}$$

where $\tilde{u}_i$ is the instantaneous value, u is the mean component and u_i' is the fluctuating component of the velocity.

The momentum equations are written for a vertical pipe, shown in Figure 2.1, with an upward flow of a fluid and solid phase.

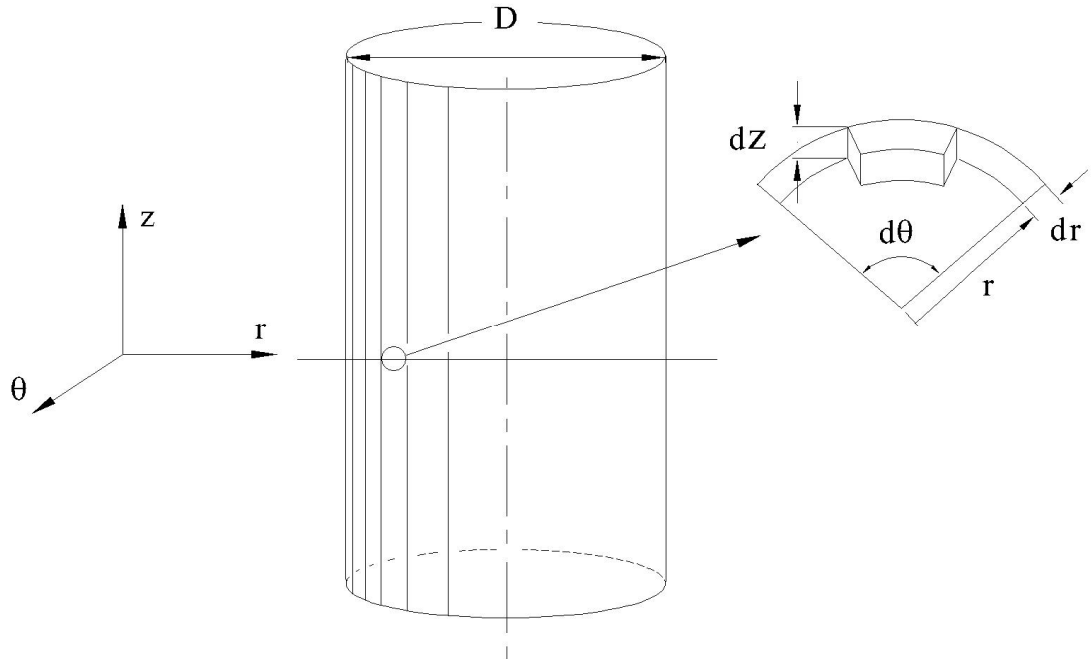

Figure 2.1 Pipe geometry and differential fluid element

Fluid phase

The momentum equation for the fluid phase in the axial direction is given as follows:

$$0 = \frac{1}{r}\frac{\partial}{\partial r}\left(r\tau_{rz}^{T}\frac{\partial u_f}{\partial r}\right) - \frac{\partial p}{\partial z} - \beta\left(u_f - u_s\right) - \rho_f c_f g \qquad (2.4)$$

where, τ_{rz}^{T} is the fluid-phase stress tensor, $\partial p/\partial z$ is the fluid pressure gradient, β is the interphase drag correlation, g is the acceleration due to gravity and z, r and θ represent the axial, radial and azimuthal directions, respectively.

The fluid-phase stress tensor is given by the following relation,

$$\tau_{rz}^{T} = \mu_f \frac{\partial u_f}{\partial r} - \rho_f \overline{u'_{fr} u'_{fz}}, \qquad (2.5)$$

where, $-\rho_f \overline{u'_{fr} u'_{fz}}$ is a component of the fluid-phase Reynolds stress tensor, which can be modelled as follows,

$$-\rho_f \overline{u'_{fr} u'_{fz}} = \mu_t \frac{\partial u_f}{\partial r} \qquad (2.6)$$

In the above equations, μ_f and μ_t are the fluid-phase molecular and eddy viscosities, respectively. The eddy viscosity is calculated using a modified two-equation low Reynolds number $k-\varepsilon$ turbulence model, where k is the turbulence kinetic energy of the fluid-phase per unit mass and ε is the dissipation rate of k. For the present work, the turbulence model of Myong and Kasagi (1990), modified by Bolio *et al.* (1995) to include the effect of the particle-phase, was used to calculate the eddy viscosity. The model of Myong and Kasagi (1990) is typically regarded as one of the better low

Reynolds number turbulence models (Hrenya *et al.*, 1995). The eddy viscosity is calculated as follows,

$$\mu_t = \frac{c_\mu f_\mu \rho_f k^2}{\varepsilon} \tag{2.7}$$

where,

$$k = \frac{1}{2}\overline{u'_{fi} u'_{fi}} \tag{2.8}$$

$$\varepsilon = \frac{\mu_f}{\rho_f}\overline{\left(\frac{\partial u_f}{\partial r}\right)\left(\frac{\partial u_f}{\partial r}\right)} \tag{2.9}$$

In equation (2.7), c_μ is a model constant and f_μ is a damping function.

The drag correlation β is calculated following the expression employed by Bolio *et al.* (1995), as follows:

$$\beta = \frac{3\rho_f C_D c_s \left| u_f - u_s \right|}{4 d_p (1 - c_s)^{2.65}} \tag{2.10}$$

where d_p is the particle diameter and C_D is the drag coefficient which is calculated as follows:

$$C_D = \frac{24\left(1 + 0.15 Re_d^{0.687}\right)}{Re_d} \tag{2.11}$$

In equation (2.11), Re_d is the particle Reynolds number which is calculated as follows:

$$Re_d = (1 - c_s) d_p \left| u_f - u_s \right| \frac{\rho_f}{\mu_f} \tag{2.12}$$

Turbulence model equations

The turbulence kinetic energy and its dissipation rate, used to compute the eddy viscosity (equation 2.7), are calculated by solving two separate transport equations.

Turbulence kinetic energy, k

$$0 = \frac{1}{r}\frac{\partial}{\partial r}\left\{ r c_f \left(\mu + \frac{\mu_t}{\sigma_k} \right) \frac{\partial k}{\partial r} \right\} + c_f \mu_t \left(\frac{\partial u_f}{\partial r} \right)^2 - \rho_f \varepsilon c_f + \Pi_f \qquad (2.13)$$

Dissipation rate of turbulence kinetic energy, ε

$$0 = \frac{1}{r}\frac{\partial}{\partial r}\left\{ r c_f \left(\mu + \frac{\mu_t}{\sigma_\varepsilon} \right) \frac{\partial \varepsilon}{\partial r} \right\} + c_{\varepsilon 1} f_1 \frac{\varepsilon}{k} c_f \mu_t \left(\frac{\partial u_f}{\partial r} \right)^2 - c_{\varepsilon 2} f_2 \rho_f c_f \frac{\varepsilon^2}{k} + c_{\varepsilon 3} \Pi_f \frac{\varepsilon}{k} \qquad (2.14)$$

where, f_1 and f_2, and $c_{\varepsilon 1}, c_{\varepsilon 2}$ and $c_{\varepsilon 3}$, are the low-Reynolds number model functions and constants, respectively; σ_k and σ_ε are the respective turbulent Prandtl numbers for *k* and ε; and Π_f is the turbulence interaction or interphase term. The values for the model constants are given in Table 2.1.

Table 2.1 Model constants in the low-Reynolds number turbulence model

c_μ	$c_{\varepsilon 1}$	$c_{\varepsilon 2}$	$c_{\varepsilon 3}$	σ_k	σ_ε
0.09	1.4	1.8	1.2	1.4	1.3

The damping function, f_μ, in equations (2.7) is calculated as follows:

$$f_\mu = \left(1 + \frac{3.45}{\sqrt{R_t}}\right)\left(1 - \exp\left[-\frac{y^+}{70}\right]\right) \tag{2.15}$$

The quantities y^+ and R_t are given by

$$y^+ = \frac{y u_\tau}{\nu_f}; \quad R_t = \frac{k^2}{\nu_f \varepsilon}, \tag{2.16}$$

where the terms y, y^+, R_t, u_τ, and ν_f are the wall normal distance, dimensionless wall normal distance using inner coordinates, turbulent Reynolds number, friction velocity and fluid-phase kinematic viscosity, respectively.

The two other damping functions are given by:

$$f_1 = 1.0 \tag{2.17}$$

$$f_2 = \left(1 - \frac{2}{9}\exp\left\{-\left[\frac{R_t}{6}\right]^2\right\}\right)\left(1 - \exp\left(-\frac{y^+}{5}\right)\right)^2 \tag{2.18}$$

The model constants and functions (given in Table 2.1) used in this work are the same as those in the single-phase $k-\varepsilon$ turbulence model of Myong and Kasagi (1990). A value of 1.2 was used for the model constant $c_{\varepsilon 3}$ in the additional source term in the ε-equation following Bolio *et al.* (1995), who adopted it from Elgobashi and Abou-Arab (1983).

A main disadvantage of the $k-\varepsilon$ turbulence model lies in the calculation of the fluid-phase velocity fluctuations. By solving its transport equation, the fluid-phase turbulence kinetic energy is obtained. If the fluid-phase fluctuating velocity is assumed to be equal

in all three directions, i.e. the velocity fluctuations are isotropic, then the fluid phase velocity fluctuations can be calculated as follows:

$$< u_f^{'2} >^{1/2} = \sqrt{\frac{2}{3}k} \tag{2.19}$$

This assumption is generally not true especially in the near-wall region where the fluctuations in the axial direction are larger than those in the other two directions (Sheen *et al*., 1993).

Particle phase

The solids phase axial and radial momentum balance equations are solved to obtain the mean solids-phase velocity u_s and the solids volume fraction/concentration c_s, respectively.

Axial force balance

$$0 = -\frac{1}{r}\frac{\partial}{\partial r}\left(r\sigma_{rz}\right) + \beta\left(u_f - u_s\right) - \rho_s c_s g \tag{2.20}$$

Radial force balance

$$0 = \frac{1}{r}\frac{\partial}{\partial r}\left(r\sigma_{rr}\right) - \frac{\sigma_{\theta\theta}}{r} \tag{2.21}$$

In equations (2.20) and (2.21), σ is a stress tensor which accounts for the shear stresses and collisions in the solids phase. The closure correlations for the shear and normal stress tensor components used in equations (20) and (21) are taken from Bolio *et al*. (1995) and calculated as follows:

$$\sigma_{rz} = -\mu_s(\omega g_1 + g_2)\frac{\partial u_s}{\partial r} \tag{2.22}$$

$$\sigma_{rr} = \sigma_{\theta\theta} = \rho_s\left(\omega c_s + 4\eta c_s^2 g_0\right)T \tag{2.23}$$

$$\mu_s = \frac{5\sqrt{\pi}\, d_p \rho_s \sqrt{T}}{96} \tag{2.24}$$

In the above equations, μ_s is the solids phase viscosity, and T is the solids granular temperature which accounts for the solids phase velocity fluctuations, i.e.

$$T = \frac{1}{3} < u_s'^2 > \tag{2.25}$$

The term η, defined as $\eta = (1+e)/2$, introduces the coefficient of restitution (e) for inter-particle collisions. The coefficient of restitution (e) is defined as the difference in the velocities of two particles before and after collision. The value of e = 1 occurs when the collision between particles is perfectly elastic, while for perfectly inelastic or plastic collisions e = 0. Kinetic theory predicts that the stress tensors in the radial and azimuthal direction are equal (Lun *et al.*, 1984). The other parameters i.e. ω, g_0, g_1 and g_2 are closure correlations defined as follows. First, following Bolio *et al*. (1995),

$$\omega = \frac{1}{1+\lambda/R} \tag{2.26}$$

where λ is the mean free path of the particles which is defined as the mean distance travelled by a particle before it collides with another particle. It is calculated as follows:

$$\lambda = \frac{d_p}{6\sqrt{2}\, c_s} \tag{2.27}$$

The other closure parameters are given as follows:

$$g_0 = \frac{C_0^{1/3}}{C_0^{1/3} - c_s^{1/3}} \tag{2.28}$$

$$g_1 = \frac{1}{\eta(2-\eta)g_0}\left[1 + \frac{8}{5}\eta c_s g_0 (3\eta - 2)\right] \tag{2.29}$$

$$g_2 = \frac{8 c_s}{5(2-\eta)}\left[1 + \frac{8}{5}\eta c_s g_0 (3\eta - 2)\right] + \frac{768 c_s^2 g_0 \eta}{25\pi} \tag{2.30}$$

In equation (28), C_0 (= 0.65) is the maximum solids volume fraction. A packed bed is formed when the solids concentration is equal to C_0 and the particles are in contact with each other such that the mean free path λ is approximately equal zero.

Solids phase granular temperature

The solids phase stresses (given above) are modelled from granular kinetic theory by treating the particle-phase as a rapid granular flow and forming an analogy with the kinetic theory of dense gases. A separate transport equation is written for the solids granular temperature to calculate the stresses associated with the solids phase as follows:

$$0 = -\frac{1}{r}\frac{\partial}{\partial r}(r q_{PT}) - \sigma_{rz}\frac{\partial u_s}{\partial r} - \gamma + \beta(< u'_{fi} u'_{si} > - 3T) \tag{2.31}$$

The above equation has been adopted from the work of Bolio *et al*. (1995). The term q_{PT} was defined in Bolio *et al*. (1995) as the pseudo-thermal energy (*T*) flux vector, while γ is the dissipation rate of pseudo-thermal energy due to inelastic particle-particle collisions. The term $< u'_{fi} u'_{si} >$ is known as the particle turbulence interaction

correlation and is discussed in the next section. The closure correlations for the parameters q_{PT} and γ are given as follows:

$$q_{PT} = -\lambda\left(\omega g_3 + g_4\right)\frac{\partial T}{\partial r} \tag{2.32}$$

where

$$\lambda = \frac{25\sqrt{\pi}d_p\rho_s\sqrt{T}}{128}, \tag{2.33}$$

$$g_3 = \frac{g}{\eta\left(41-33\eta\right)g_0}\left[1+\frac{12}{5}\eta^2 c_s g_0\left(4\eta-3\right)\right], \tag{2.34}$$

$$g_4 = \frac{96c_s}{5\left(41-33\eta\right)}\left[1+\frac{12}{5}\eta^2 c_s g_0\left(4\eta-3\right)+\frac{16}{15\pi}\eta c_s g_0\left(41-33\eta\right)\right] \tag{2.35}$$

$$\gamma = \frac{48}{\sqrt{\pi}}\eta\left(1-\eta\right)g_0 c_s^2\frac{\rho_s}{d_p}T^{3/2} \tag{2.36}$$

It is interesting to note that when the particle-particle collisions are perfectly elastic, the term γ vanishes and hence there is no dissipation of energy.

Turbulence modulation

The last term Π_f in equations (13) and (14) is known as the turbulence interaction or interphase term, and is used to account for the effect of particles on the fluid-phase turbulence (i.e. turbulence modulation). This term was modeled by Bolio *et al*. (1995) as follows:

$$\Pi_f = -\beta c_f\left(2k-<u'_{fi}u'_{si}>\right) \tag{2.37}$$

The term $< u'_{fi} u'_{si} >$ in equation (2.37) was previously identified as the particle-turbulence interaction correlation. The expression adopted for this term following Louge *et al*. (1991) was

$$< u'_{fi} u'_{si} >= \frac{4}{\sqrt{\pi}} \frac{d_p}{\rho_s} \frac{\beta}{c_s} \frac{\left(u_f - u_s\right)^2}{\sqrt{T}} \tag{2.38}$$

Sinclair and Mallo (1998) proposed a different expression for the term $< u'_{fi} u'_{si} >$ given by

$$< u'_{fi} u'_{si} >= \sqrt{2k}\sqrt{3T} \tag{2.39}$$

Note that, whereas the expression for $< u'_{fi} u'_{si} >$ given by equation (38) depends on the local slip between the two phases, the closure used in equation (39) relies on the product of the two (isotropic) fluctuation fields. Equation (39) was used for the liquid-solid flow analysis as better predictions were obtained with it compared to those obtained using equation (38).

2.1.3 Boundary conditions

Boundary conditions for phases must be specified at the wall and the centreline for the vertical pipe flow. The wall boundary conditions used in this work for the vertical pipe flow are as follows:

Gas phase

a) **Mean velocity,** u_f : At the wall, a no-slip boundary condition is specified for the mean velocity.

$$u_f\big|_{\text{wall}} = 0 \tag{2.40}$$

b) **Turbulence kinetic energy,** *k*: At the wall, a value of zero is set for the turbulence kinetic energy.

$$k\big|_{\text{wall}} = 0 \tag{2.41}$$

c) **Dissipation rate of *k*, ε**: The boundary condition for ε has been formulated following Myong and Kasagi (1990), who calculated ε at the wall by solving the transport equation for *k* in the near-wall region.

$$\varepsilon\big|_{\text{wall}} = \nu_f \left.\frac{\partial^2 k}{\partial r^2}\right|_{wall} \tag{2.42}$$

Particle phase

Neither the mean velocity nor the granular temperature of solid particles is zero at the wall (refer to Bolio *et al*., 1995). Instead, the wall boundary conditions for the particle phase are formulated following Sinclair and Jackson (1989) whose expressions were based on the boundary conditions developed by Hui *et al*. (1984) and Johnson and Jackson (1987).

a) ***Mean velocity,*** u_s: The wall boundary condition for the particle velocity is computed by equating the shear or tangential stress in the particle assembly in the region adjoining the wall to the momentum flux transmitted from the particle to the wall due to particle-wall collisions, as described by Sinclair and Jackson (1989) and Bolio *et al*. (1995).

$$\sigma_{rz} = \frac{\rho_s \pi c_s \phi \sqrt{T}}{2\sqrt{3}\left(\frac{C_0}{c_s} - \frac{C_0^{2/3}}{c_s^{2/3}}\right)} \tag{2.43}$$

The expression for the solids phase shear stress (equation 22) was substituted in the above equation and the boundary condition was employed as a gradient of the solids velocity at the wall, i.e.,

$$\left.\frac{\partial u_s}{\partial r}\right|_{wall} = -\frac{48\sqrt{\pi}\phi\, c_s g_0 u_s|_{wall}}{5\sqrt{3} d C_0 (\omega g_1 + g_2)} \tag{2.44}$$

In the above equation, ϕ is the specularity coefficient, and it is a function of the wall surface. The specularity coefficient ranges from zero, when the collisions are specular (smooth wall surface), to unity, when the collisions are diffuse (rough wall surfaces). In this case, a value of ϕ=0.002 was used following Bolio *et al*. (1995).

b) ***Granular temperature*** *T*: The wall boundary condition for the granular temperature is reported by Sinclair and Jackson (1989) and Bolio *et al*. (1995) and is obtained by equating the energy conducted to the wall due to inter-particle collisions to the energy lost at the wall by particle-wall collisions and the energy generated by specular particle-wall collisions.

$$q_{PT_r} = \frac{\sqrt{3}\rho_s \pi (1 - e_w^2) T^{3/2}}{4\left(\frac{C_0}{c_s} - \frac{C_0^{2/3}}{c_s^{2/3}}\right)} - \frac{\rho_s \pi c_s^2 \phi \sqrt{T}}{2\sqrt{3}\left(\frac{C_0}{c_s} - \frac{C_0^{2/3}}{c_s^{2/3}}\right)} \tag{2.45}$$

The boundary condition for *T* is employed by substituting the expression for $q_{PT\,r}$ and rewriting it as the gradient of *T* at the wall as follows:

$$\left.\frac{\partial T}{\partial r}\right|_{wall} = \left(\frac{\phi u_s^{old}\big|_{wall} u_s\big|_{wall}}{\sqrt{3}} - \frac{\sqrt{3}(1-e_w^2)T\big|_{wall}}{2} \right) \frac{64\sqrt{\pi}\, c_s g_0}{25 C_0 d(\omega g_3 + g_4)} \qquad (2.46)$$

where e_w is the coefficient of restitution for particle-wall collisions. In this work, a value of 0.7 was assigned to e_w following the study of Bolio *et al.* (1995).

The boundary conditions for the particle velocity and granular temperature at the wall are non-linear: they depend on the velocity of the solids phase, the solids concentration, the granular temperature and other variables such as the shear stress in the particle assembly.

At the centre of the pipe, the gradient of all parameters is zero, since the flow is axisymmetric. Therefore, at the centreline all the parameters have the following boundary condition:

$$\frac{\partial \varphi}{\partial r} = 0 \qquad (2.47)$$

where φ can be any parameter such as fluid or particle velocity, granular temperature, etc.

2.2 Numerical Solution Method

The numerical solution for the model is obtained by solving five coupled partial differential equations for u_f, u_s, k, ε and T and one algebraic equation for c_s. The coupled transport equations (eqs. 4, 13, 14, 20 and 31) and the algebraic equation (eq. 21) were solved simultaneously employing the finite-volume technique developed by Patankar (1980) to obtain the equations in a discretised form (refer to Appendix A for a

description of the discretisation method). The pipe domain was divided into 60 non-uniformly distributed control volumes in the radial direction with a high concentration of control volumes near the wall. The solution was demonstrated to be grid independent (refer to Appendix B) when 60 control volumes were used. The boundary conditions described above were implemented at the wall and the centre of the pipe. A Tri-Diagonal Matrix Algorithm (TDMA) was used to solve the equations and a pseudo-transient solution method was adopted, i.e. the solution produced was iterated in time until a converged solution field was obtained. The following convergence criterion was adopted:

$$\frac{\varphi_n - \varphi_{n-1}}{\varphi_{n-1}} < 10^{-4} \tag{2.48}$$

where φ_n is the value of a variable at the present time step and φ_{n-1} is its value at the previous time step.

The fluid-phase pressure gradient and centreline solids volume fraction were used as inputs, and iterated until the bulk conditions that match the experimental data were obtained. The following algorithm provides details of the solution method, which is also described by the flow chart given in Figure 2.2.

1. Initialize the field values (at time t = 0) for the fluid and particle phase velocities (u_f and u_s, respectively), fluid-phase turbulence parameters (k and ε), solids volume fraction (c_s) and granular temperature (T).
2. Compute the closure coefficients based on the initial guesses.
3. Solve the fluid phase momentum eqation (eq. 4) and calculate the fluid velocity.

4. Calculate the fluid-phase turbulence kinetic energy and the rate of dissipation from their respective equations (eqs. 13 and 14) and compute the eddy viscosity.
5. Solve the axial momentum equation for the particle phase velocity (eq. 20).
6. Calculate the integration constant I_C.
7. Solve for the particle granular temperature (eq. 31).
8. Determine c_s from the particle phase radial force balance equation (eq. 21) using the Newton-Raphson method.
9. Check convergence (for each parameter).
    a. If all the parameters satisfy the convergence criteria, stop iterating.
    b. If not, assign the present field to the old field and compute the new value of the parameter. Repeat this until the convergence criteria are satisfied.
10. Check the Reynolds number: if it is not equal to the desired value, modify the pressure gradient and repeat the steps 2-10 until the specified value is obtained.

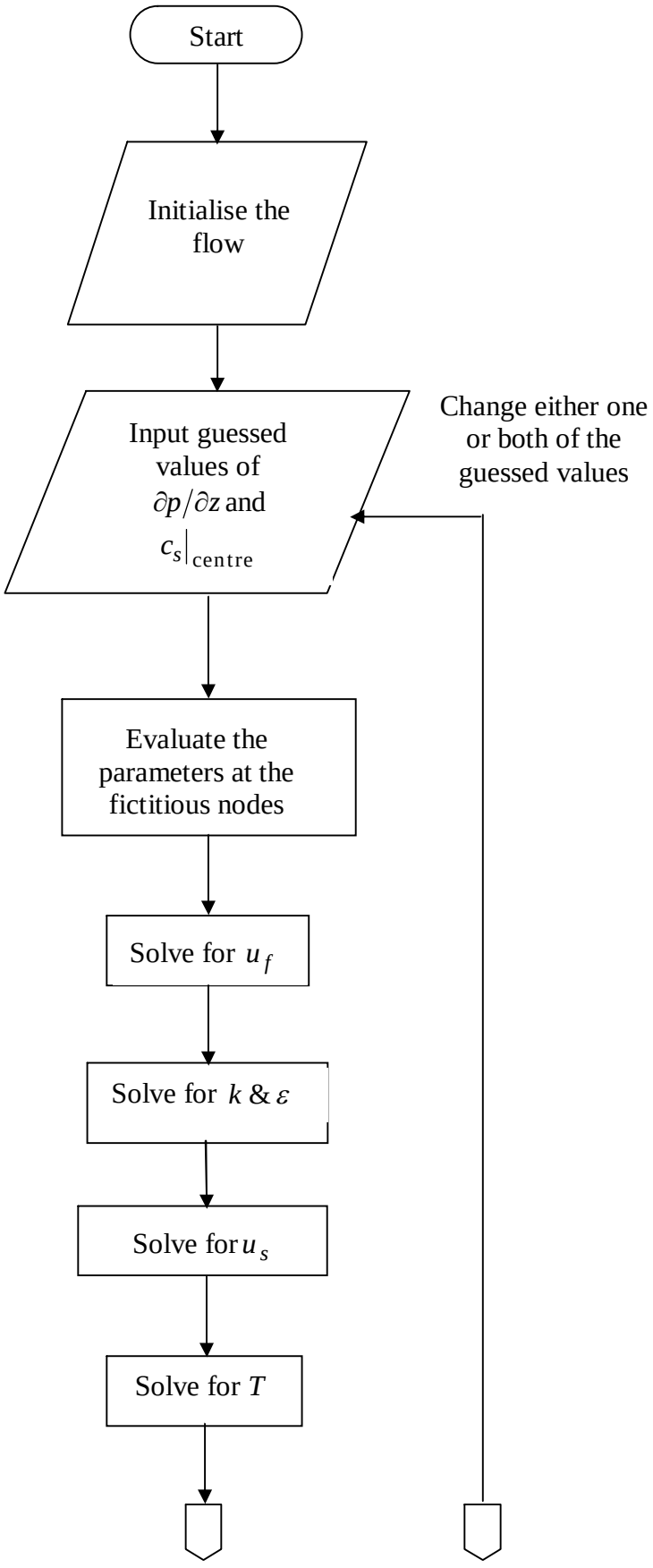
Start
Initialise the flow
Input guessed values of $\partial p/\partial z$ and $c_s|_{centre}$
Change either one or both of the guessed values
Evaluate the parameters at the fictitious nodes
Solve for u_f
Solve for k & ε
Solve for u_s
Solve for T

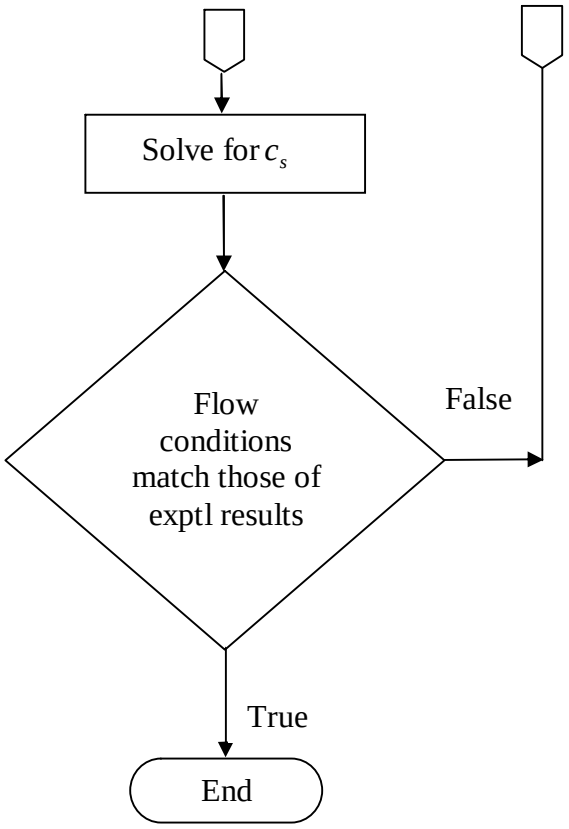

Figure 2.2 Flow chart describing the solution procedure for a two-phase turbulent fluid-solid flow

3 TWO-PHASE GAS-SOLID FLOWS

Introduction

This chapter reports the prediction of two-phase laminar and turbulent vertical gas-solid flows. Simulations were performed using the gas-solid flow model of Bolio *et al*. (1995) and the behaviour of the mean and fluctuating velocities for the gas and solid phases, solids volume fraction and the turbulent flow case pressure drop predictions were investigated. Laminar gas-solid flow predictions involved solid particles of diameter $d_p = 150\,\mu m$ and Reynolds number Re = 1010 for bulk solids concentrations of $c_{s,b} =$ 0.18. Solid particles ranging from $d_p = 100$ to $400\,\mu m$ and Re = 16000 to 40000 for $c_{s,b} = 0.001$ - 0.007 were investigated for the turbulent flow case. The numerical results were compared to the predictions of Sinclair and Jackson (1989) for the laminar flow case, and the experimental measurements of Lee and Durst (1982), Tsuji *et al.* (1984), and Henthorn *et al*. (2005) for the turbulent flow case. In general, the mean velocity predictions were found to be in close agreement with the data.

3.1 Laminar flow

Laminar flow was investigated for vertical pipe flow using the model proposed by Sinclair and Jackson (1989). A laminar flow was investigated initially, since it is a

relatively simpler case to compute, yet provides an understanding of the momentum equations for both phases. Even though the flow is laminar, many of the equations are non-linear and therefore challenging to solve. The flow parameters are given in Table 3.1.

Table 3.1 Flow properties for the laminar case

1. Density of the fluid, $\rho_f = 0.52\ \text{kgm}^{-3}$
2. Density of the particles, $\rho_p = 2500\ \text{kgm}^{-3}$
3. Viscosity of the fluid, $\mu_f = 0.0000365\ \text{Nsm}^{-2}$
4. Pressure gradient $= 10000\ \text{Nm}^{-3}$
5. Pipe radius, $R = 0.015$ m
6. Particle size, $d_p = 150\ \mu\text{m}$
7. Particle terminal velocity, $U_t = 1.29\ \text{ms}^{-1}$
8. Particle-particle coefficient of restitution, $e = 0.95$
9. Particle-wall coefficient of restitution, $e_w = 0.90$
10. Specularity factor, $\phi = 0.5$
11. Close packed volume fraction for solids, $C_{s0} = 0.65$

Figure 3.1 shows the radial variation of the phasic mean velocities, normalized with the terminal velocity of a single particle, U_t , the solids concentration and the solids velocity fluctuations calculated from the relation, $u_s' = \sqrt{3T}$, normalised with U_t. A dense gas-solid flow, with a bulk solids concentration of 0.18 and bulk gas and solids volumetric flow rates of 1.277×10^{-3} and 9.8×10^{-5} $m^3 s^{-1}$, respectively, was considered for the present simulation. The mean velocity profiles for both phases, shown in Figure 3.1 (a), are in good agreement with the predictions of Sinclair and Jackson (1989). Another interesting observation from Figure 3.1 (a) is the behaviour of the gas-phase velocity in the near-wall region: the gas velocity was zero at the wall but had a finite value in the immediate vicinity of the wall. Even though the point velocity of the gas-phase is zero at the wall, for situations such as fluidized beds, the velocity of the gas may vary markedly with radial position when moving away from the wall (Sinclair, 1989). It can be observed from Figure 3.1 (b) that a high concentration of particles exists at the pipe wall. This effect, as a result of the weight, was evident from Figure 3.1 (a), where both the velocity profiles assumed a characteristic concave shape near the wall.

Figure 3.1 (c) shows the radial distribution of solids velocity fluctuations. Note that even though the flow is laminar there are fluctuations in the solids velocity field. However, the magnitude of the solids velocity fluctuations is not high enough to create turbulence in the gas-phase. The model predicts higher fluctuations at the core of the pipe which is a region with lower solids volume fraction. A comparison between the granular temperature and the solids volume fraction is relevant due to the inverse relation that exists between the two quantities (refer to equation 2.37).

The mean velocity predictions for two-phase laminar gas-solid flow are more or less similar to the single-phase laminar flow predictions except in the near-wall region. The solids volume fraction is maximum at the wall for these flows while the granular temperature, which is a measure of the fluctuations in the solids phase, is maximum at the centre of the pipe. Laminar flow was helpful in developing competence with the momentum equations for the fluid and particle phases which were non-linear. An understanding of the solids-phase radial momentum balance and its solution method was accomplished from laminar flow investigation. The study also highlighted the solids velocity fluctuations that were not clearly driven by turbulence. On the whole, laminar flow was a way in to solve turbulent flow.

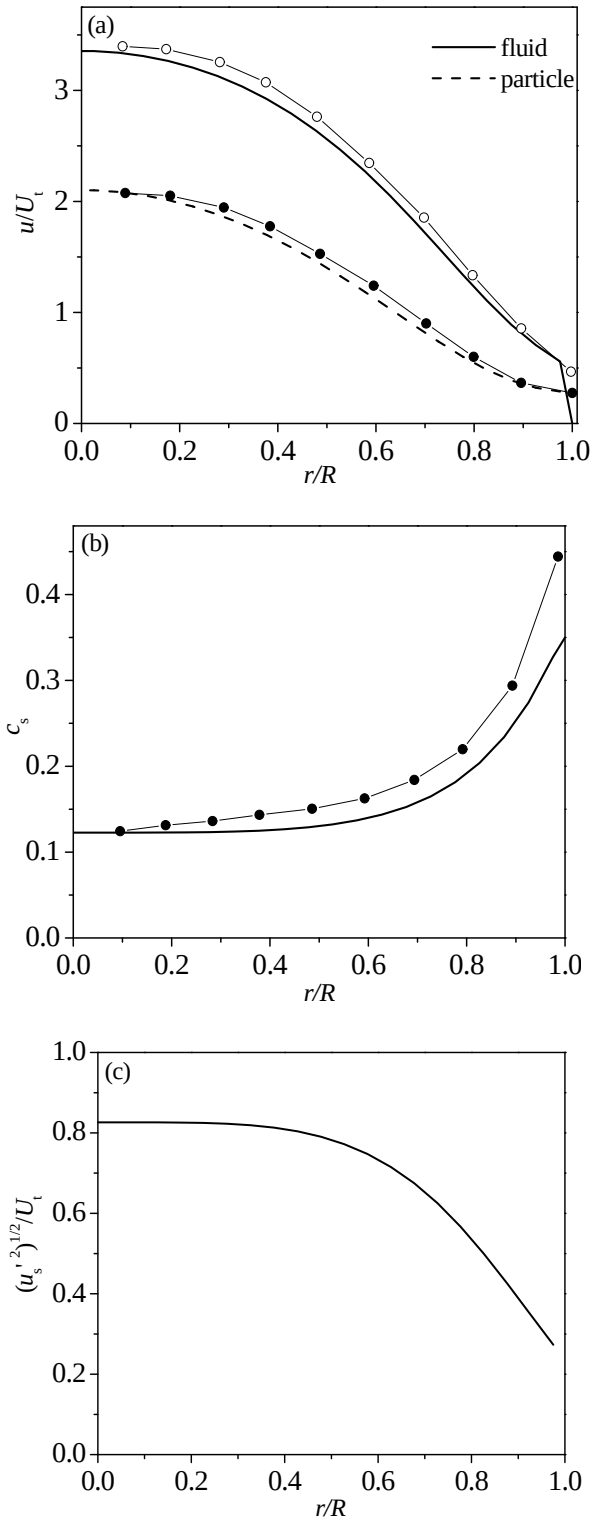

Figure 3.1 Radial variation of (a) mean velocity profiles for both phases, (b) solids volume fraction and (c) solids velocity fluctuations for laminar gas-solid flows. Circles with lines represent the predictions of Sinclair and Jackson (1989), where open and closed symbols represent fluid and solid phases, respectively.

3.2 Turbulent flow

The turbulent flow model proposed by Bolio *et al*. (1995) was subsequently investigated. The physical properties and the flow parameters used for this flow are given in Table 3.2.

Table 3.2 Physical properties for the turbulent flow case

1. Density of the fluid, ρ_f = 1.205 kgm^{-3}
2. Density of the particles, ρ_p = 2590 and 1020 kgm^{-3}
3. Viscosity of the fluid, μ_f = 0.000018 Nsm^{-2}
4. Pipe radius, D = 0.0209 and 0.01525 m
5. Particle sizes, d_p = 100, 200, and 400 μm
6. Particle-particle coefficient of restitution, e = 0.94
7. Particle-wall coefficient of restitution, e_w = 0.94
8. Specularity factor, $\phi = 0.002$
9. Close packed volume fraction for solids, C_0 = 0.65

3.2.1 Velocity profiles

First, the behaviour of the mean velocity profiles for particles with different diameters was investigated in order to examine the particle size effects at similar operating conditions. Figure 3.2 compares the predicted mean velocity profiles (for both phases) for 100, 200 and 400 μm spherical glass particles with the experimental data of Lee and

Durst (1982) and also the simulated results of Bolio *et al*. (1995). To obtain the mean velocity profiles, the code was iterated until the desired mass loading, *m* and the pipe Reynolds number, Re that match the experimental results, were achieved. The mass loading and Reynolds number are calculated as follows:

$$m = \frac{\int \rho_s c_s u_s \mathrm{d}A}{\int \rho_f (1 - c_s) u_f \mathrm{d}A} \tag{3.1}$$

$$\mathrm{Re} = \frac{\rho_f u_f D}{\mu_f} \tag{3.2}$$

where d*A* is the area of the pipe.

The mass loadings and Reynolds numbers for all cases are approximately, 1.3 and 16800, respectively. A progressive increase in the slip of the particle velocity is clearly evident from the figure as the particle size increases. The best agreement with the experimental data was observed for the $400\,\mu\mathrm{m}$ particles. Both numerical simulations (the present case and Bolio *et al*., 1995) predict mean gas-phase velocity profiles which follow the trend shown by the experimental values, i.e. the gas velocity exhibits an almost constant velocity profile in the outer region, and a sharp decrease in the near-wall region. However, both simulations predicted gas velocity profiles with a noticeably narrower near-wall region than was evident in the data. The solids mean velocity profiles were more or less constant across the pipe test section.

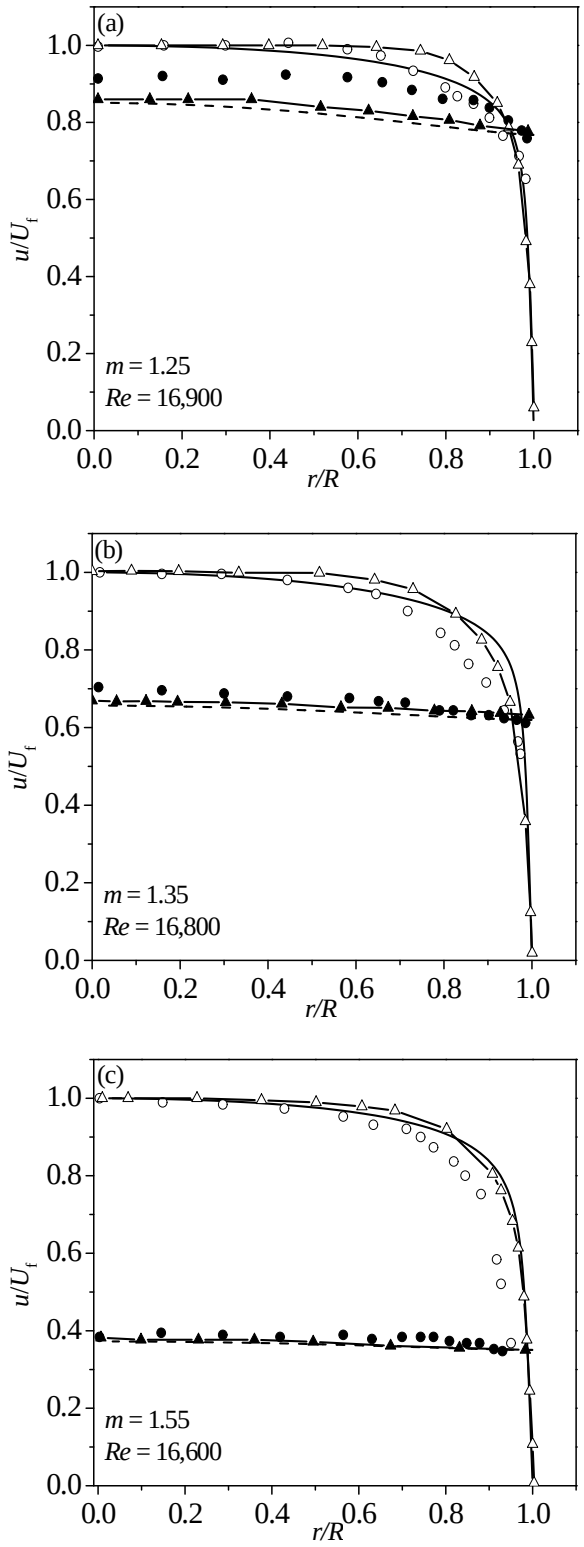

Figure 3.2 Radial variation of mean velocity profiles for (a) 100 µm, (b) 200 µm and (c) 400 µm particles. Circles represent the data of Lee and Durst (1982) and triangles with lines represent the predictions of Bolio *et al*. (1995). Open and closed symbols represent fluid and solid phases, respectively.

3.2.2 Concentration profiles

Figure 3.3 illustrates concentration profiles for particles of different sizes and different mass loadings. Figure 3.3 (a) shows the concentration predictions for the 100 and 400 µm particles, at a mass loading (*m*) of 1.25 and a Reynolds number (*Re*) of 16,900. The concentration profiles for both particles were fairly uniform across the pipe, with the 400 µm particles producing a higher concentration compared to the 200 µm particles. The concentration profiles for the 200 µm particles for two different mass loadings and Reynolds numbers are shown in Figure 3.3 (b) and (c). Figure 3.3 (b) shows the concentration profile for m = 1.0 and Re = 39,600. The profiles were almost constant across the pipe as was the case with the predictions of Bolio *et al*. (1995). In Figure 3.3 (c), the solids concentration predictions for a higher mass loading, m = 4.2 and Re = 30,600 are shown. A higher value for the solids concentration was observed at the core of the pipe. The solids concentration predictions were compared only with the numerical results of Bolio *et al*. (1995), since no experimental results were available for comparison.

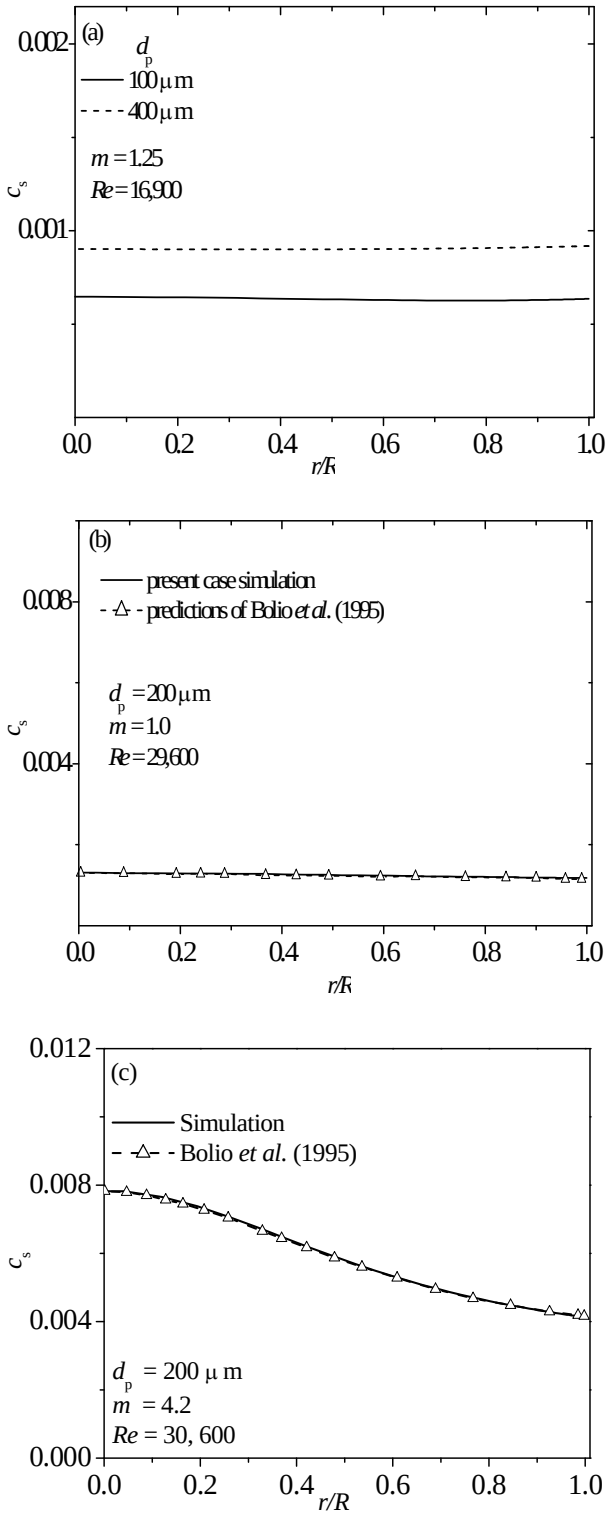

Figure 3.3 Radial variation of solids volume fraction for (a) 100 and 400 μm particles at m = 1.25 and Re = 16,900, (b) 200 μm particles at m = 1.0 and Re = 39,600 and (c) 200 μm particles at m = 4.2 and Re = 30,600. The triangles represent predictions of Bolio *et al*. (1995).

3.2.3 Solids-phase fluctuating velocity profiles

In Figure 3.4 (a), the predicted solids velocity fluctuations u_s', calculated from granular temperature T, for the 100 and 400 μm particles at m = 1.25 and Re = 16,900 are compared. The solids velocity fluctuation is calculated from the following relation:

$$u_s' = \sqrt{3T} \tag{3.3}$$

The profiles were almost uniform across the pipe test section with the 400 μm particles predicting lower values of the fluctuating velocity. Figure 3.4 (b) and (c) compare the predictions of the solids velocity fluctuations at m = 1.0 and 4.2, and Re = 39,600 and 30,600, respectively, with the unpublished data of Tsuji (1993), extracted from Bolio *et al*. (1995), and the numerical results of Bolio *et al*. (1995). The numerical results, both the present simulations and the predictions of Bolio *et al*. (1995), under predict the case of m = 1.0 and over predict the case of m = 4.2. Note that, the behaviour of the solids velocity fluctuation is inverse to that of the solids volume fraction profiles (compare Figures 3.3 and 3.4).

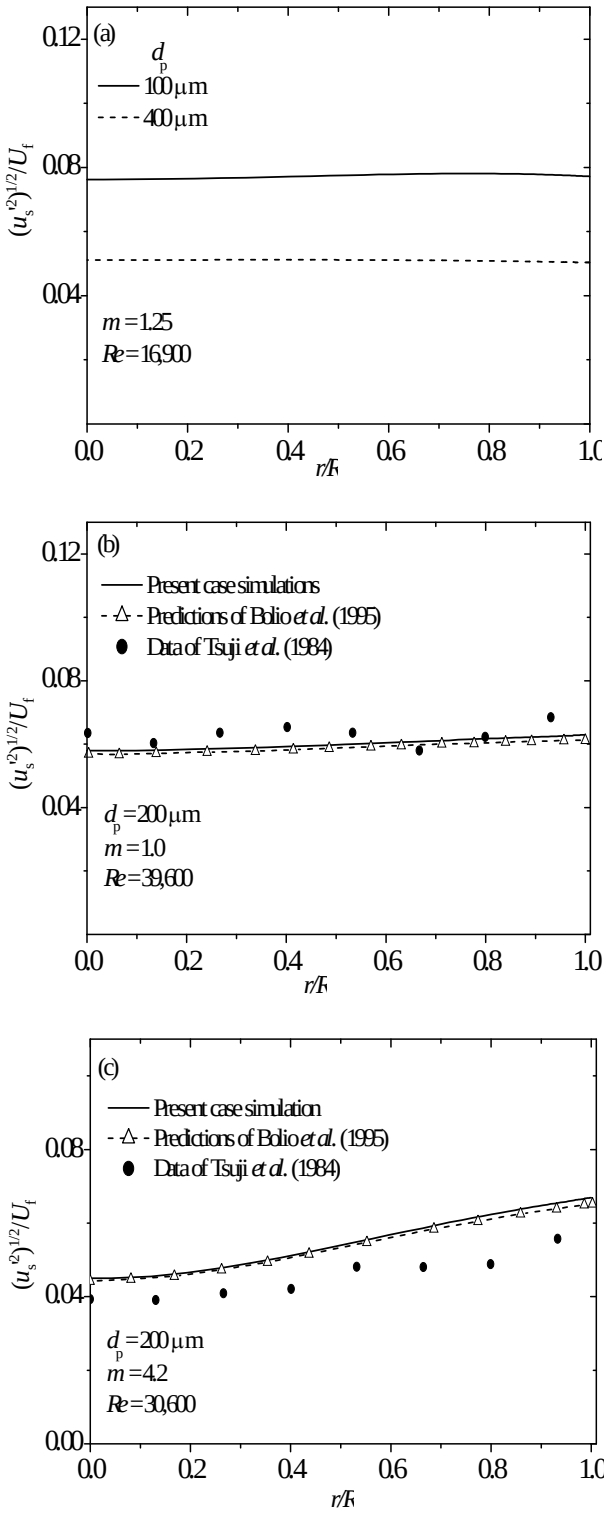

Figure 3.4 Radial variation of solids velocity fluctuations for (a) 100 and 400 μm particles at m = 1.25 and Re = 16,900, (b) 200 μm particles at m = 1.0 and Re = 39,600 (c) 200 μm particles at m = 4.2 and Re = 30,600.

3.2.4 Gas-phase velocity fluctuations

Figure 3.5 shows the gas-phase velocity fluctuations for particles of different sizes and mass loadings compared with the data of Tsuji *et al*. (1984). Figure 3.5 (a) compares the predictions for the radial variation of the axial gas velocity fluctuations for 100 and 400 μm particles with single-phase flow. It demonstrates that small particles (100 μm) added to single-phase flow at lower mass loading (m = 1.25), result in turbulence suppression. In Tsuji *et al*. (1984), it was shown that smaller particles suppress turbulence throughout the pipe, while larger particles (of the order 3 mm) enhance it for higher mass loadings. When the particle size was increased to 400 μm for the same mass loading and Reynolds number (Re = 16,900), it was seen from Figure 3.5 (a) that both turbulence enhancement (in the near-wall region) and suppression (at the centre) were observed in the pipe section, compared with the 100 μm particles. This behaviour is consistent with the analysis of Tsuji *et al*. (1984), who found that for medium sized particles (about 500 μm), both enhancement and suppression of turbulence is observed at different locations along the pipe section. Note that in Figure 3.5 (a), the prediction is still consistently below level of the single phase prediction.

In Figure 3.5 (b) and (c), the turbulence intensity of the gas-phase for 200 μm particles at mass loadings of m = 0.9 and 3.2, and Reynolds numbers of Re = 26,900 and 22,700, respectively, are compared with the experimental data of Tsuji *et al*. (1984) and the predictions of Bolio *et al*. (1995). The present simulations, while in good agreement with the numerical results of Bolio *et al*. (1995), significantly under predicted the turbulence intensity values compared to the experimental data especially in the

core/centre region of the pipe. The experimental data of Tsuji *et al*. (1984) involve the gas-phase velocity fluctuations in the stream-wise direction alone. However, in the model, the gas-phase velocity fluctuations are considered to be isotropic in nature i.e. the gas phase is considered to have equal fluctuations in all the three directions (axial, radial and azimuthal). Therefore, the comparison of isotropic model predictions with the an-isotropic data may be inadequate.

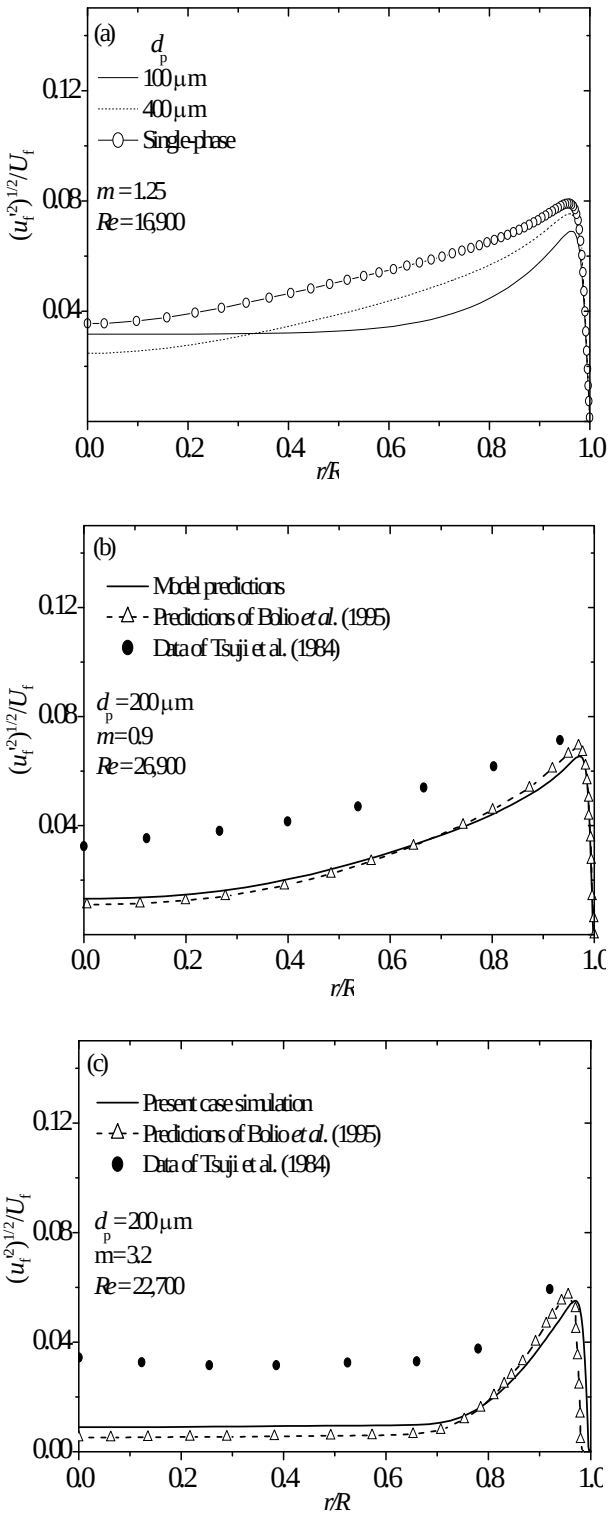

Figure 3.5 Radial variation of axial gas velocity fluctuations for (a) 100 and 400 μm particles at m = 1.25 and Re = 16,900; (b) 200 μm particles at m = 1.0 and Re = 39,600; (c) 200 μm particles at m = 4.2 and Re = 30,600.

3.2.5 Eddy viscosity profiles

Figure 3.6 (a) shows predictions for the eddy viscosity for the 100 and 400 µm particles at m = 1.25 and Re = 16,900, compared with single-phase flow results. It can be seen from the figure that as the particle size was increased for the same mass loading and Reynolds number, there was a reduction in the eddy viscosity compared to the single-phase flow. The shape of the profile for the 100 µm particles is different compared to the other two profiles. This behaviour is an artefact of the turbulence kinetic energy which is used to calculate the eddy viscosity. Figure 3.6 (b) and (c) show the eddy viscosity profiles for 200 µm particles for mass loadings of 0.9 and 3.2, respectively. The profiles become flatter with increasing mass loading for the same particle size (200 µm) in addition to the reduction in viscosity levels. Note that particles reduce turbulent transport in the gas phase. It is interesting to note that for m = 0.9, the eddy viscosity is maximum in the near-wall region (at r/R ~ 0.73), i.e. the wall production dominates. However, for the case of higher mass loadings, the maximum value for the eddy viscosity is observed to shift towards the centre of the pipe as shown in Figure 3.6 (c).

It can be concluded from this section that the model was successful in predicting the mean velocity profiles for both phases, and to some extent the solids fluctuating velocities. The predicted gas-phase velocity fluctuations followed the trend exhibited by the data but were significantly under-predicted. The model responded well to changes in particle size and mass loading.

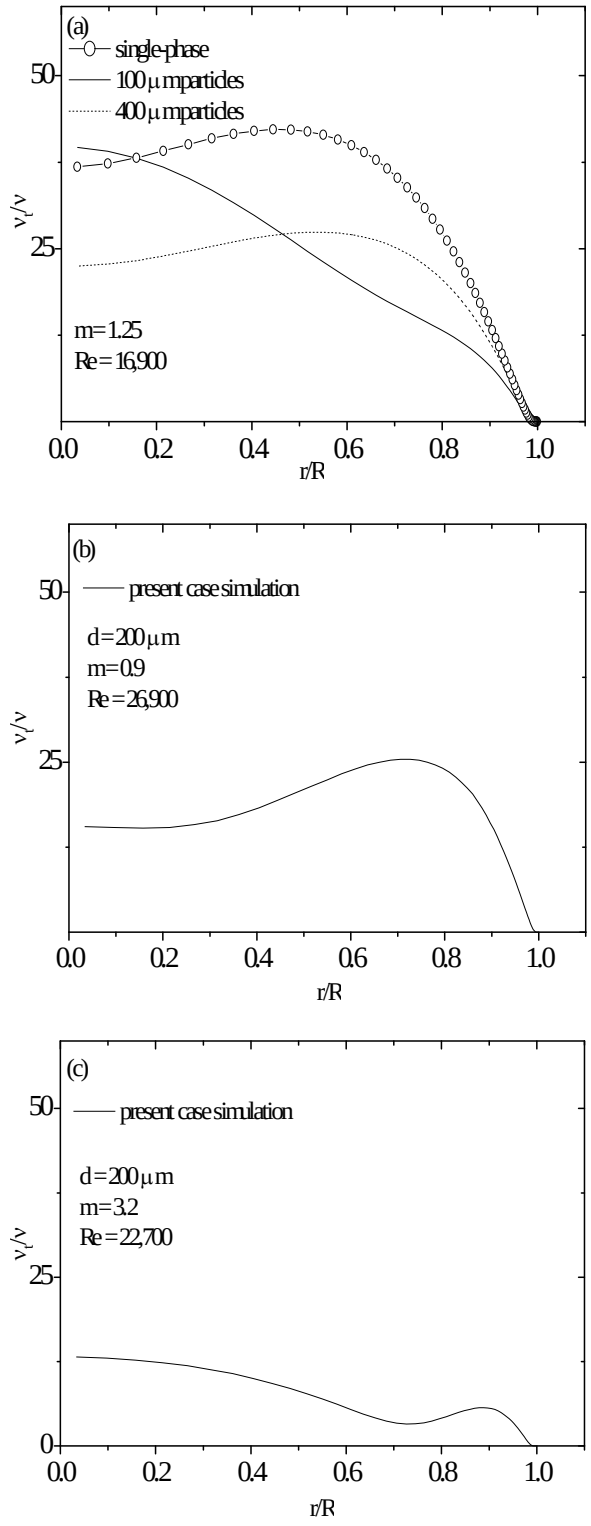

Figure 3.6 Radial variation of eddy viscosity for (a) 100 and 400 μm particles at m = 1.25 and Re = 16,900, (b) 200 μm particles at m = 1.0 and Re = 39,600 (c) 200 μm particles at m = 4.2 and Re = 30,600.

3.3 Pressure gradient predictions

The pressure drop in fully developed turbulent gas-solid flow was also investigated using the two-fluid model of Bolio *et al*. (1995). The numerical predictions for the pressure drop were validated with the experimental data of Henthorn *et al.* (2005). In the experiments carried out by Henthorn *et al*. (2005), solid particles (glass, sand and mica) of different sizes were transported in a vertical copper tube of diameter 2.54 cm. Pressure drop measurements were made for both single- and two-phase flows for different mass loadings, Reynolds numbers, and particle sizes.

The predictions and the data for the pressure gradient were also compared with the results obtained using an experimental correlation. The correlation used to calculate the approximate total pressure drop in gas-solid flow, which results from the contributions of both phases (Henthorn *et al.*, 2005) is given by,

$$\Delta P_T = \underset{(1)}{\frac{f_g \rho_f u_f^2 L}{2D}} + \underset{(2)}{F_{pw} L} + \underset{(3)}{\rho_f L (1 - c_s) g \sin\theta} + \underset{(4)}{\rho_p L c_s g \sin\theta} \qquad (3.4)$$

where terms (1) and (2), and (3) and (4), represent gas- and particle-phase stress, and weight, respectively. In equation (3.4), θ represents the angle of inclination of the pipe to the horizontal; L is the length over which the pressure measurement is made, f_g is the single-phase Fanning friction factor, and F_{pw} is the solids pipe friction.

The expression for the solids pipe friction, F_{pw}, used in Henthorn *et al*. (2005) was proposed by Konno and Saito (1969) and is given by,

$$F_{pw} = 0.057 m \rho_p u_s \sqrt{\frac{g}{D}} \tag{3.5}$$

where m is the mass loading for the gas-solid flow. For a fully developed gas-solid flow in a vertical pipe, the pressure gradient correlation takes the following form:

$$\frac{\Delta P_T}{L} = \frac{f_g \rho_f u_f^2}{2D} + 0.057 m \rho_p u_s \sqrt{\frac{g}{D}} + \rho_f \left(1 - c_s\right) g + \rho_p c_s g \,, \tag{3.6}$$

while for a single-phase flow, the pressure gradient correlation takes the form,

$$\frac{\Delta P_T}{L} = \frac{f_g \rho_f u_f^2}{2D} + \rho_f g \tag{3.7}$$

In the present work, the friction factor, f_g, was calculated from the Colebrook correlation which for a smooth wall is given as follows:

$$\frac{1}{f_g^{1/2}} = -2.0 \log\left(\frac{2.51}{Re\, f_g^{1/2}} \right) \tag{3.8}$$

The friction factor can also be calculated from the friction velocity u_τ.

3.3.1 Effect of Reynolds number

The effect of Reynolds number on the pressure drop for both single- and two-phase flows in a vertical pipe flow is first considered. Single-phase flow pressure drop predictions for Reynolds numbers ranging from 6,000 to 20,000 are shown in Figure 3.7 (a). The predictions were compared with the experimental data of Henthorn *et al.* (2005) and the correlation given in equation (3.4). It can be seen from the figure that the pressure drop increases with increasing Reynolds number. The model predictions, the data, and the correlation results are all in close agreement with each other.

Figure 3.7 (b) shows two-phase flow pressure drop predictions for 70 µm particles at a constant mass loading of 2.0 over a range of Reynolds numbers. The model predictions were compared with the results obtained using the correlation given in equation (3.4) and the numerical predictions of Hadinoto *et al*. (2004), who considered the effects of interstitial fluid in their model. It is seen from the figure that both models (Bolio *et al*., 1995 and Hadinoto *et al*., 2004) over-predict the pressure drop compared to the correlation. The difference between the predictions and the correlation is also seen to be increasing with increasing Reynolds number. According to Henthorn *et al*. (2005), the reason for the over prediction of pressure drop by the models is mainly due to the gas-phase stress term. In the correlation, the gas-phase stress is independent of the presence of the particles and therefore a single-phase Fanning friction factor is used for the calculation of the stress. The effect of particles on the gas-phase is included in modelling the gas-phase stress term in both models. The particles dampen the gas-phase turbulence and therefore, a higher pressure drop is required when the particles are included.

It is further seen from Figure 3.7 (b) that under similar flow conditions the pressure drop required for a two-phase flow is higher than that of a single-phase flow, which may be due to the weight of the particles. The model predictions were slightly higher than the numerical results of Hadinoto *et al*. (2004) at larger Reynolds numbers.

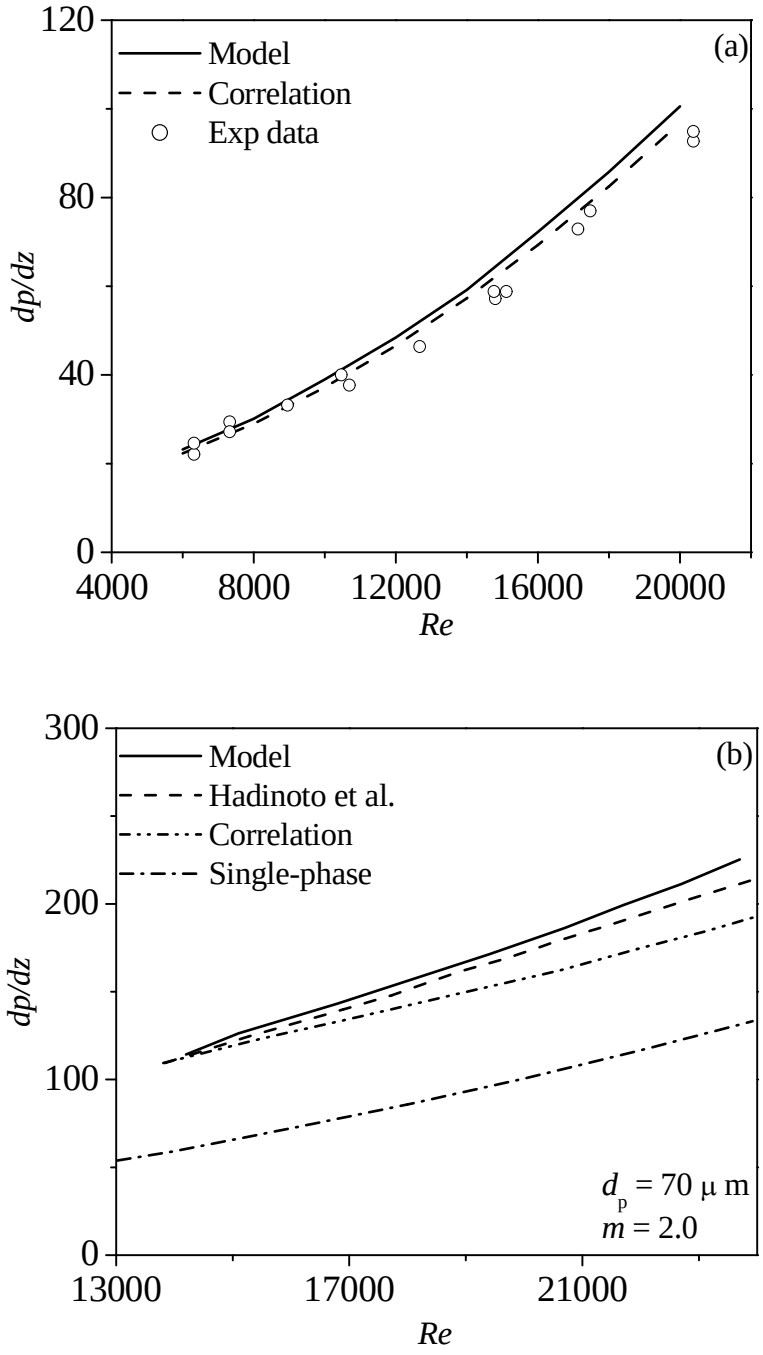

Figure 3.7 Comparison of the pressure gradient predictions for (a) single-phase flow with the data of Henthorn *et al.* (2005) and the correlation (eq. 3.5), and (b) two-phase flow with the correlation (eq. 3.4) and predictions of Hadinoto *et al*. (2004).

3.3.2 Effects of mass loading and Reynolds number

Figure 3.8 illustrates the effects of mass loading and Reynolds number on the pressure drop predictions. The pressure drop was predicted for 70 (Figure 3.8 a) and 200 μm (Figure 3.8 b) particles and different mass loadings *m*, at constant Reynolds numbers of *Re* = 15100 and 20400. The model predictions were compared with the experimental data of Henthorn *et al.* (2005), correlation (eq. 3.6) results and the numerical predictions of Hadinoto *et al*. (2004). The experimental measurements, correlation results, and both the model predictions show that the pressure drop increases with increasing mass loading and Reynolds number.

It is seen from Figure 3.8 that the present model predictions for both particles (70 and 200 μm) are in excellent agreement with the experimental data and the correlation (eq. 3.6) for the case where *Re* = 15100. The numerical results for both the models slightly over predicted the experimental data and the correlation results for *Re* = 20400. Figure 3.8 (a) illustrates that the numerical results of Hadinoto *et al*. (2004) are slightly better than the present model predictions for the 70 μm particles, whereas the pressure drop predictions for the 200 μm particles, shown in Figure 3.8 (b), are marginally better with the present model. It is observed that the pressure gradient increases with *m* at fixed *Re*. This increase in the pressure gradient is due to the increase in bulk solids concentration with increasing *m*. This increases the weight of the particle assembly in the pipe and reduces the overall pipe *Re*. A higher pressure gradient is therefore required to maintain the *Re* at the desired value.

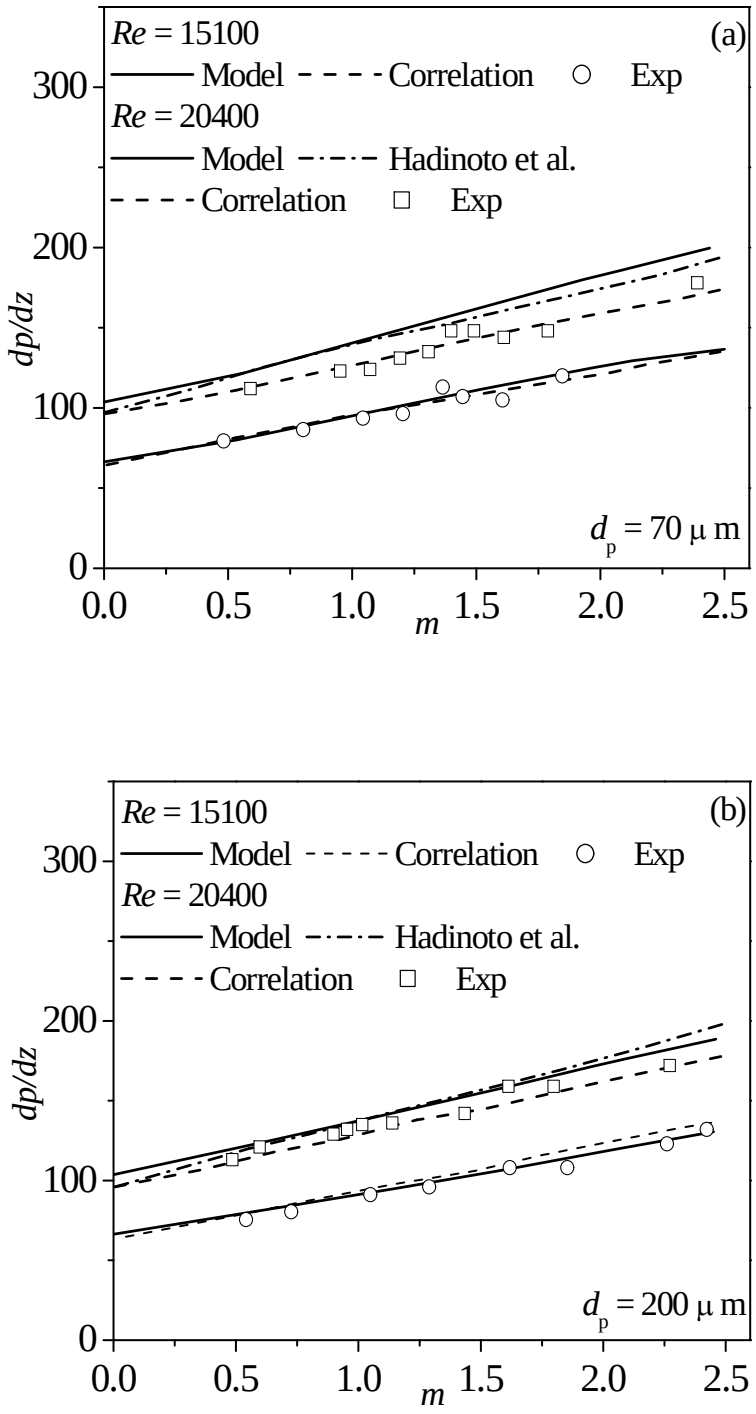

Figure 3.8 Comparison of the pressure gradient predictions with the data of Henthorn *et al.* (2005), the correlation (eq. 3.4) and the predictions of Hadinoto *et al.* (2004) for (a) 70 and (b) 200 particles at Re = 15100 and 20400.

Another interesting observation that can be made from Figure 3.8 (a) and (b) relates to the difference between the pressure drop values for the 70 and 200 μm particles. It is seen that although the particle size increased, the pressure drop increased only by a small amount. A detailed analysis of the effect of the size of the particles on the pressure drop is presented in the following section.

3.3.3 Effect of particle size

Figure 3.9 explores the effect of particle size on the pressure drop predictions. The model was analysed for 70, 200, and 275 μm glass spheres for Reynolds number Re = 15100, as shown in Figure 3.9 (a), and for 70, 200, and 500 μm glass spheres for *Re* = 20400, shown in Figure 3.9 (b). The predictions were compared with the experimental data of Henthorn *et al.* (2005).

It can be seen from Figure 3.9 that the pressure gradient predictions and experimental data increase with increasing mass loading for all particles. The experimental pressure gradient measurements, shown in Figure 3.9 (a), have a peculiar variation. They first decrease as particle size increases and then increase with increasing particle size at *Re* = 15,100. A similar behaviour was also reported by Wang *et al*. (2000) who observed that at low *Re* the pressure gradient first decreases as particle size increases and then starts increasing with particle size. The model predictions for the *Re* = 15100 case, shown in Figure 3.9 (a), also show a similar trend. According to Henthorn *et al.* (2005), the solids gravity term influences the pressure gradient to follow this trend. However, as *Re* increases, this trend is no longer followed.

The pressure gradient data for the case where *Re* = 20400, shown in Figure 3.9 (b), follow a slightly different trend. The data of Henthorn *et al.* (2005) show only an increase in the pressure gradient with increasing particle size as was also illustrated by the measurements of Nieuwland *et al*. (1997). The model pressure gradient predictions however, follow a trend similar to that shown in Figure 3.9 (a). The predicted pressure gradient first decreases as the particle size increases from 70 to 200 μm, and then starts increasing with increasing particle size. Since there was no increase in pressure gradient predicted for the 500 μm particles, larger particles of size 700 μm were also analysed for similar conditions, as shown in Figure 3.9 (b). The predicted pressure gradient for the 700 μm particles follows the trend discussed above, i.e. shows an increase in the pressure gradient. However, overall the model predicts minimal increase in pressure gradient with particle size.

The two-fluid model of Bolio *et al*. (1995) was in agreement with the experimental data of Henthorn *et al.* (2005) for lower Reynolds number of Re = 15,100. The predicted profiles for *Re* = 20400 were able to capture the trend exhibited by the data when the effects of *m* and *Re* were investigated. The model however, over-predicted the experimental measurements. The model predictions involving the effect of particle size on the pressure drop followed the trend shown by the data for the case where Re = 15,100. However, the model again failed to agree with the data for the Re = 20,400 case. It is therefore concluded that the two-fluid model of Bolio *et al.* (1995) performs well for limited flows.

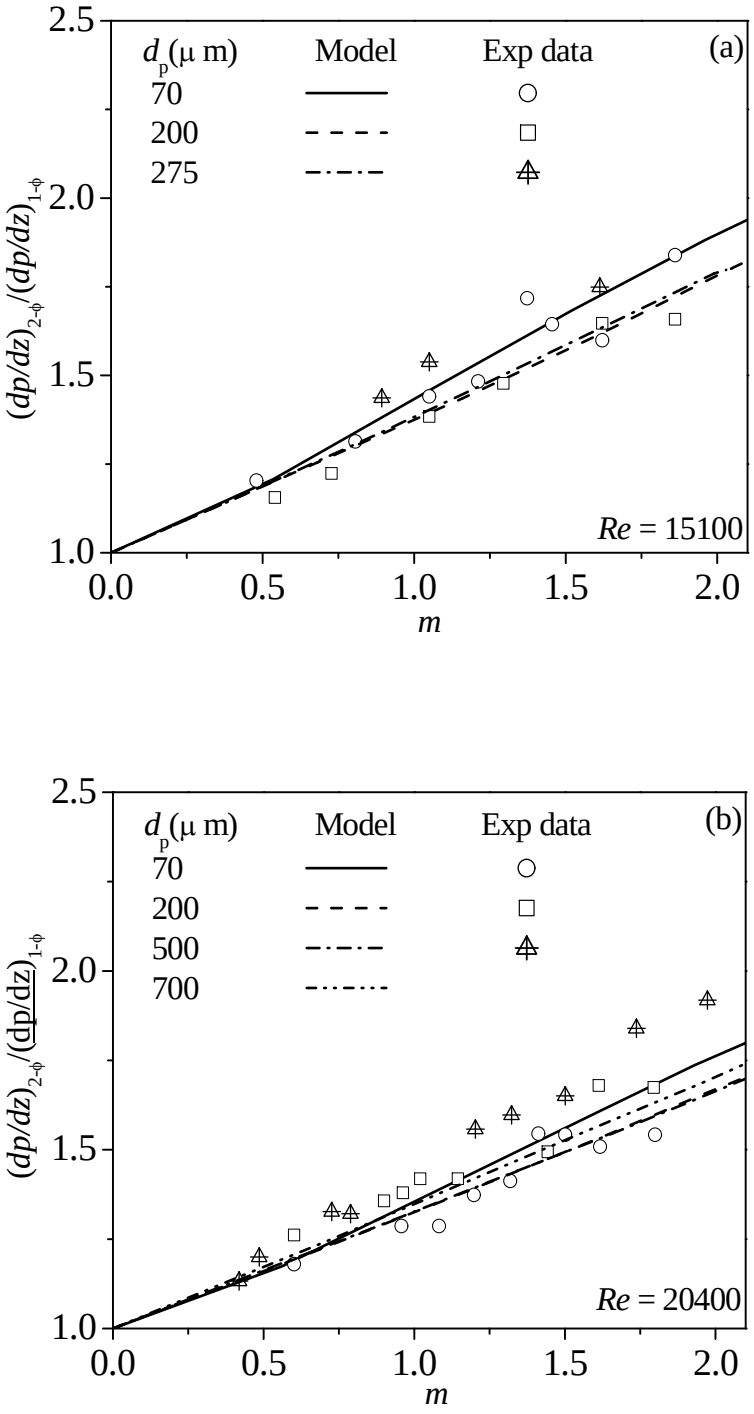

Figure 3.9 Comparison of the pressure gradient predictions with the data of Henthorn *et al.* (2005) for particles of different sizes at (a) Re = 15,100 and (b) Re = 20,400.

4 TWO-PHASE TURBULENT LIQUID-SOLID FLOW

Introduction

This chapter summarises predictions for fully-developed turbulent liquid-solid flow for bulk solids concentrations up to 40%. The turbulent two-fluid gas-solid flow model proposed by Bolio *et al.* (1995), with the turbulence interaction closure of Sinclair and Mallo (1998), was applied to the liquid-solid flow case. The turbulence interaction closure proposed by Sinclair and Mallo (1998) was used in this model instead of that employed by Bolio *et al*. (1995) as it significantly improved the liquid turbulence kinetic energy predictions. The numerical predictions obtained were compared with the experimental data of Alejbegovic *et al.* (1994) for cases where the bulk solids concentration was about 4% (which would be considered a dilute flow case) and Sumner *et al*. (1990) for higher concentrations (a dense flow case). This chapter also reports predictions for the liquid-solid flow pressure drop in a vertical pipe. The liquid phase in this study was water and the particle phase consisted of particles of different sizes and densities. The pressure drop predictions were compared with the experimental data of Shook and Bartosik (1994).

4.1 Dilute flow case

A dilute turbulent liquid-solid flow with bulk solids concentrations between 1 and 4% was investigated using the model proposed by Bolio *et al*. (1998). A co-current up-flow of a mixture of water and either ceramic or expanded polystyrene particles was considered for a vertical pipe with a diameter of 30.6 mm. The predictions were compared with the experimental data of Alejbegovic *et al*. (1994) for different total mass flow rates (*w*), which was calculated in the model as follows:

$$w = \left(\rho_f (1 - c_s) u_f + \rho_s c_s u_s\right) A \tag{4.1}$$

In the above equation, *A* is the cross-sectional area of the pipe. The flow and particle properties used for this simulation are listed in Table 4.1.

Table 4.1 Flow properties for the dilute flow case

1. Diameter of the pipe, D = 30.6 mm
2. Density of fluid, $\rho_f = 997.09\,\mathrm{kgm^{-3}}$
3. Viscosity of fluid, $\mu_f = 0.001\,\mathrm{Nsm^{-2}}$
4. Size of ceramic particles, $d_p = 2.32$ mm
5. Size of expanded polystyrene particles, $d_p = 1.79$ mm
6. Density of ceramic particles, $\rho_p = 2442.87\,\mathrm{kgm^{-3}}$
7. Density of expanded polystyrene particles, $\rho_p = 31.91\,\mathrm{kgm^{-3}}$

Alejbegovic *et al*. (1994) used a fiber-flow laser-Doppler anemometer (LDA) to measure the local velocities, turbulence intensities and Reynolds stresses for both phases (liquid and solid). The solids concentration in the vertical pipe, made of transparent fluorinated ethylene propylene, was measured using a single-beam Gamma-ray densitometer along with the LDA at different locations.

Figure 4.1 compares predicted and measured mean velocity (for both phases) and solids volume fraction/concentration profiles for 2.32 mm ceramic particles and different total mass flow rates. The predicted liquid-phase mean velocity profiles, shown in Figure 4.1 (a), are in good agreement with the experimental data while the solids mean velocity profiles are slightly under-predicted. The predicted slip between the liquid- and solid-phase velocities is higher than the slip shown by the data. Figure 4.1 (b) presents concentration predictions for the ceramic particles compared with the data of Alejbegovic *et al*. (1994). It is seen from the figure that the predicted solids concentration profiles are uniform across the pipe radius. The present simulations fail to predict the shape of the concentration profiles given by the experimental data in the near-wall region. There is a peak in the predicted solids concentration close to the wall as opposed to the data which decreases. As the mass flow rate increased, the difference between the data and the predictions was more pronounced in the near-wall region. Also, the measurements show a particle-free region near the pipe wall, but no such (particle-free) region is observed for the predictions. It should be noted that $c_{s,b} \sim 0.025$ for the predictions, while for the data $c_{s,b} \sim 0.041$. The total mass flow rate for the predictions was matched with that of the experimental data and this resulted in different bulk solids

concentrations for the data and the predictions. When the bulk solids concentrations were matched, higher values of total mass flow rates were obtained.

Figure 4.2 presents the fluid-phase turbulence kinetic energy, *k*, compared to the single-phase predictions and the solids-phase granular temperature profiles plotted against the experimental data for different total mass flow rates. Recall that the turbulence kinetic energy accounts for fluid-phase velocity fluctuations while the granular temperature represents solids-phase velocity fluctuations. It is seen from the turbulence kinetic energy profiles, shown in Figure 4.2 (a), that excellent agreement exists between the model predictions and the experimental data. The single-phase turbulence kinetic energy profiles, calculated using the two-equation low Reynolds number model of Myong and Kasagi (1990), is also in a close agreement with the two-phase flow *k* profiles. This implies that for liquid-solid flows, when bulk solids concentration is approximately 0.025, there is very little particle effect. The profiles peak at around $y^+ = 20$ (*y/R* ~ 0.02), suggesting that the production of *k* is maximum at this location. According to Alejbegovic *et al.* (1994), this may be due to particle-induced turbulence and vortex shedding behind the particles, which typically move faster than the liquid in the near-wall region. The turbulence kinetic energy is also driven by the velocity gradient which is high in the near-wall region. It is also observed from Figure 4.2 (a) that with increasing mass flow rate, *k* increases both at the wall and at the centre of the pipe.

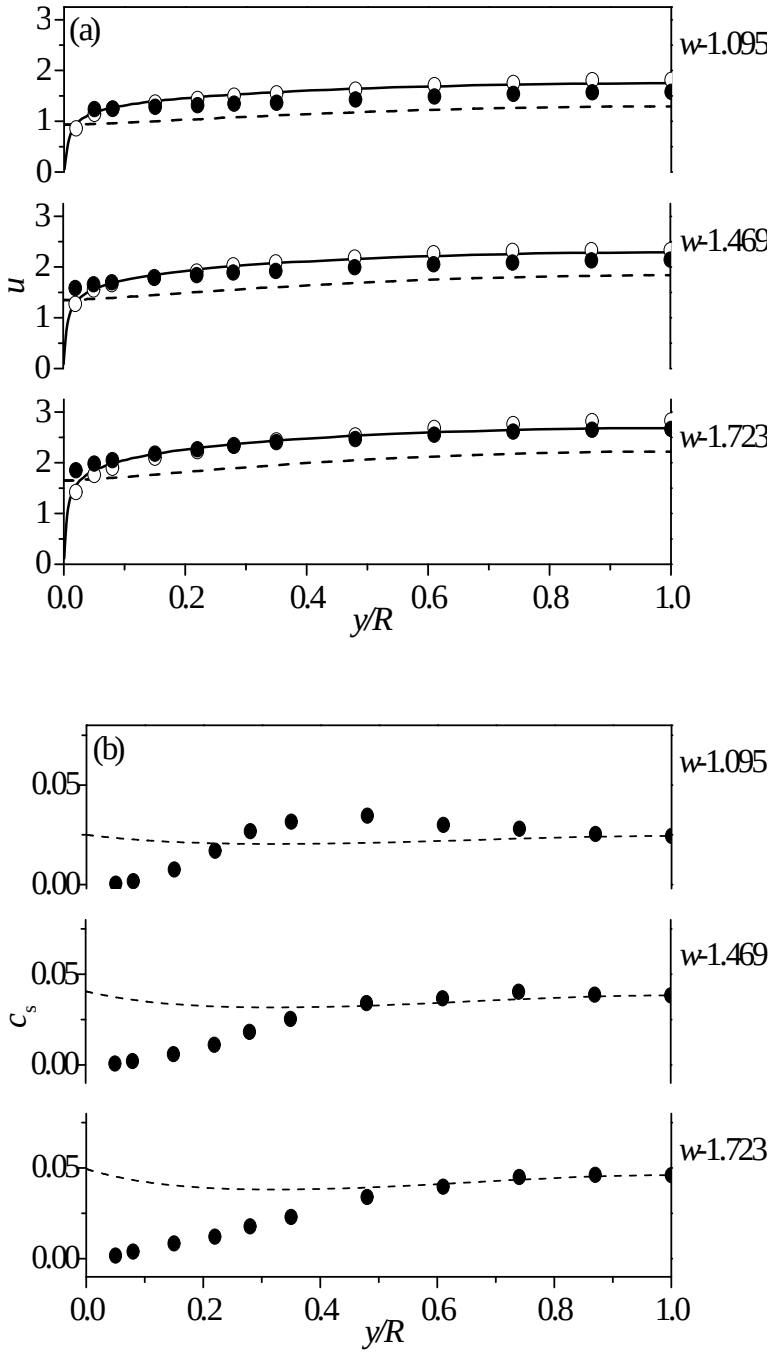

Figure 4.1 Comparison of the predicted (a) mean velocity profiles for both the phases and (b) solids volume fraction profiles for 2.32 mm ceramic particles for different total mass flow rates. Solid and dashed lines and open and closed symbols represent the fluid- and solids-phase predictions and data of Alejbegovic *et al*. (1994), respectively.

The solids granular temperature profiles, shown in Figure 4.2 (b), follow the trend exhibited by the experimental data but significantly over-predict the measurements. As the total mass flow rate increases, there is an overall increase in the level of both the measured and the predicted solids granular temperature. The discrepancy between the data and the predictions was observed to increase with increasing total mass flow rate. The profiles, for the data and the predictions, were flatter at lower total mass flow rates but as w increases (to 1.723), the data and the predictions show a peak value at approximately $y/R \sim 0.30$.

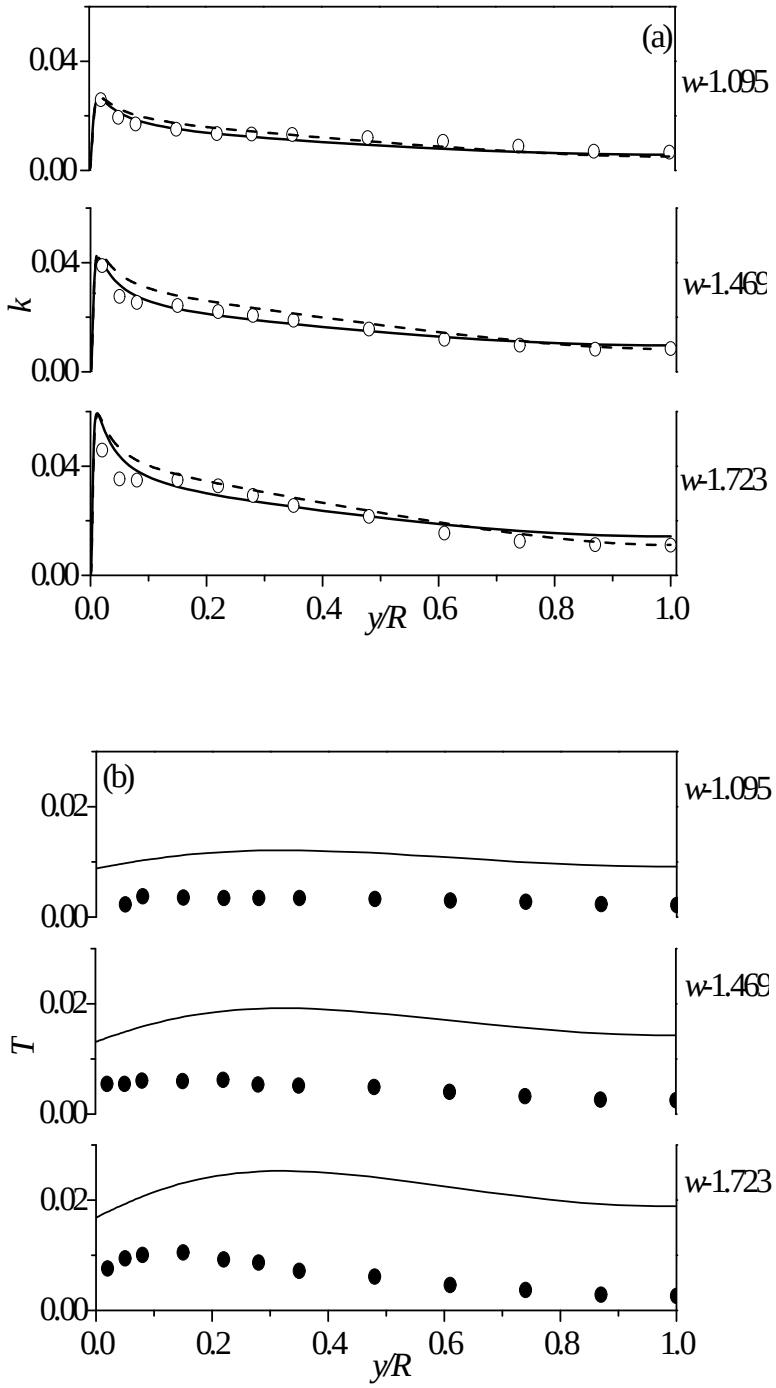

Figure 4.2 Comparison of predicted (a) fluid-phase turbulence kinetic energy and (b) solids-phase granular temperature with the data of Alejbegovic *et al*. (1994) for 2.32 mm ceramic particles for different total mass flow rates. Open and closed symbols represent the experimental data, dashed lines represent single-phase turbulence kinetic energy predictions and solid lines represent two phase flow predictions.

Eddy viscosity profiles for the ceramic particles are shown in Figure 4.3. The model predictions were compared with the single-phase eddy viscosity predictions obtained using the two-equation low Reynolds number model of Myong and Kasagi (1990). It is seen that the addition of particles seems to have only a minimal effect on the profiles at lower total mass flow rates.

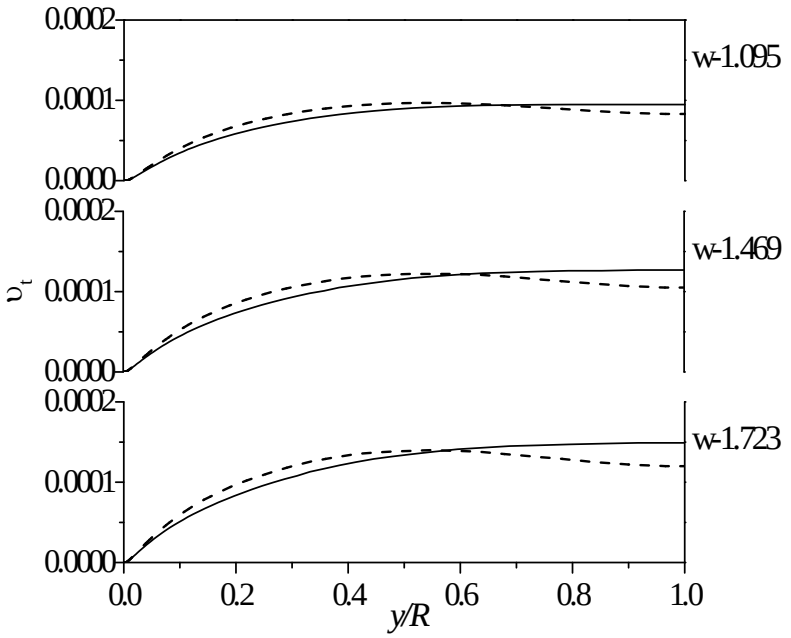

Figure 4.3 Eddy viscosity profiles for 2.32 mm ceramic particles at different total mass flow rates. Dashed lines represent the eddy viscosity predictions for a single-phase.

The liquid-solid flow predictions for smaller and lighter expanded polystyrene particles ($\rho_s = 31.91$ kgm^{-3}) are presented in Figure 4.4 and 4.5. Figure 4.4 (a) shows the predicted mean velocity profiles for 1.79 mm expanded polystyrene particles for different mass flow rates compared with the experimental data. It is seen from the figure that the solids velocity measurements exceed that of the fluid indicating that the particles

move faster than the liquid. According to Alejbegovic *et al.* (1994), positive buoyancy is responsible for this behaviour. However, the model predictions show almost equal velocities for both the phases. Both the data and the predictions show an increase in velocity throughout the pipe with increasing total mass flow rates.

Figure 4.4 (b) shows the solids concentration predictions for the expanded polystyrene particles. A large discrepancy in the value of the solids concentration, as seen from Figure 4.4 (b), is observed between the predictions and measurements in the near-wall region. A significant peak in the value of concentration at around $y/R = 0.1$ is shown by the data, while a much more uniform profile is shown by the predictions. The predicted solids concentration is maximum at the centre and minimum at the wall.

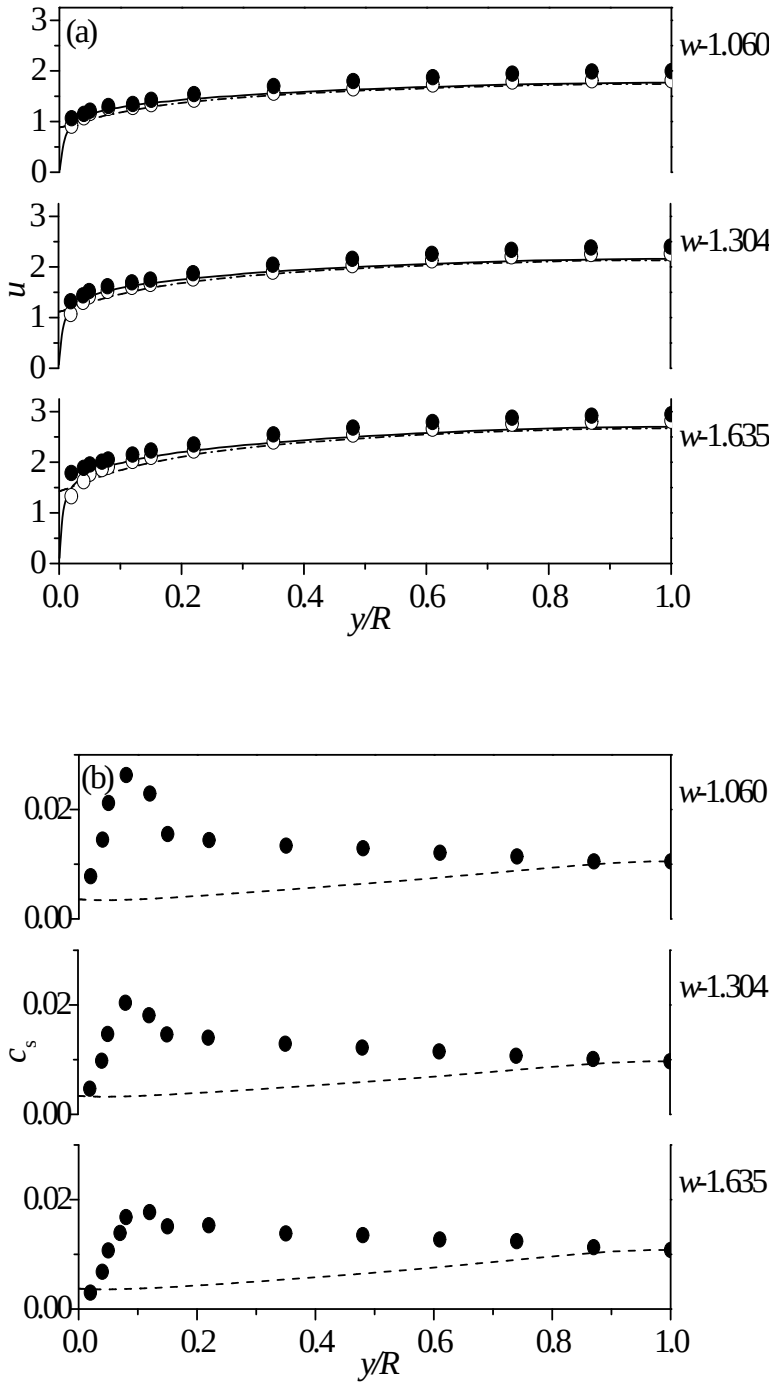

Figure 4.4 Comparison of the predicted (a) mean velocity profiles for both the phases and (b) solids volume fraction profiles for 1.79 mm expanded polystyrene particles for different total mass flow rates. Solid and dashed lines and open and closed symbols represent fluid- and solids-phase predictions and data, respectively.

Figure 4.5 presents the radial variation of fluid-phase turbulence kinetic energy for a single-phase flow and a liquid-solid flow and solids-phase granular temperature, compared with the experimental data of Alejbegovic *et al*. (1994). As was the case with the ceramic particles, the turbulence kinetic energy profiles for the expanded polystyrene particles shown in Figure 4.5 exhibit excellent agreement between the model predictions and the experimental data. The single-phase flow predictions agreed even better with the data and predictions for the expanded polystyrene particles than for the ceramic particles. This suggests that the addition of particles in the bulk solids concentration range of 0.01 with a density much lower than that of the fluid phase does not significantly affect the fluid turbulence structure.

The granular temperature predictions for the expanded polystyrene particles are shown in Figure 4.5 (b). The predictions and experimental data agree with each other except in the near-wall region, where the numerical results over-predict the data. As was the case with the ceramic particles, the difference between the predictions and the data, in the near-wall region, is seen to increase with increasing total mass flow rate. The profiles for the data are relatively flatter at lower *w* showing a distinct peak only at the highest value of *w*. The predictions, on the other hand, always show a peak close to the wall. Further, Figure 4.5 shows that with increasing total mass flow rate, both k and T increase throughout the pipe.

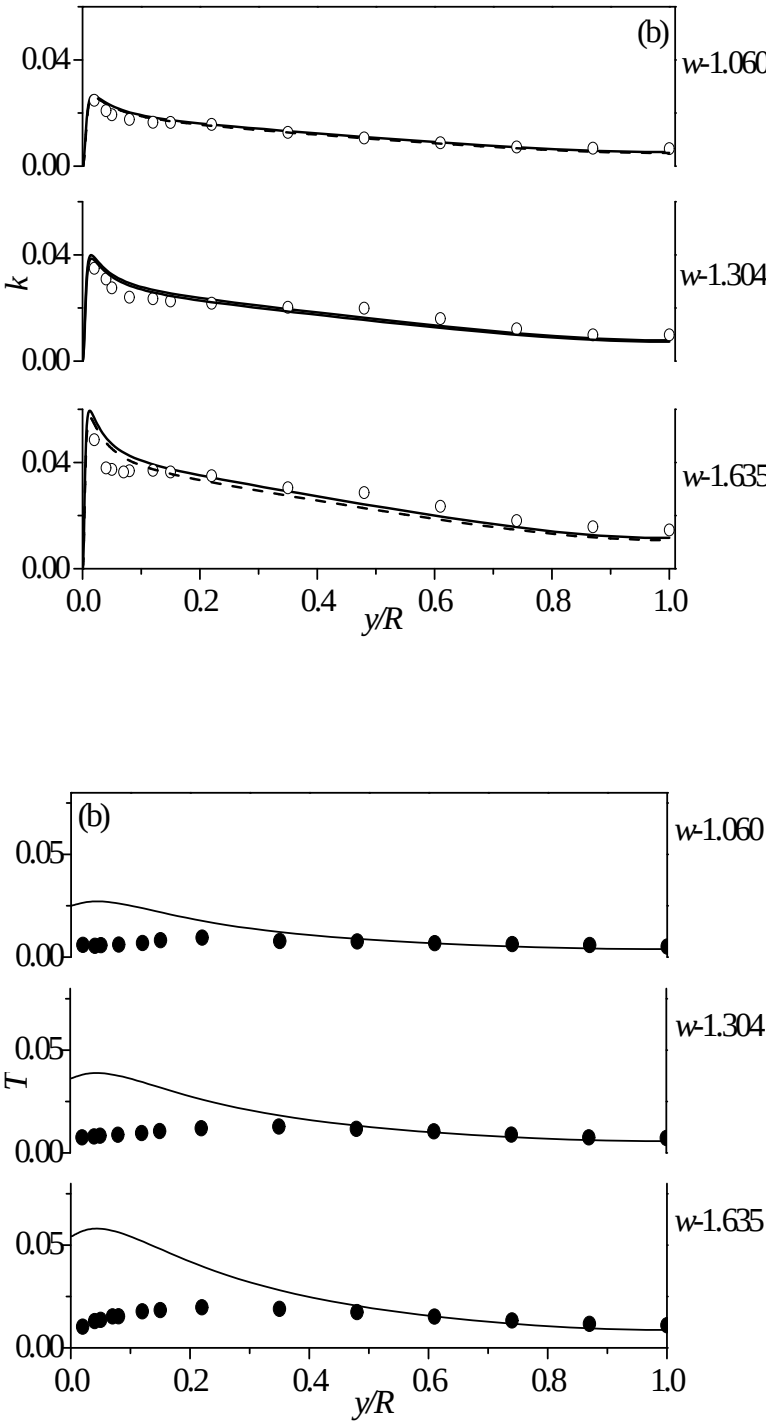

Figure 4.5 Comparison of predicted (a) fluid-phase turbulence kinetic energy and (b) solids-phases granular temperature with the data for 1.79 mm expanded polystyrene particles for different total mass flow rates. Closed symbols represent the data and dashed lines represent the single phase flow predictions.

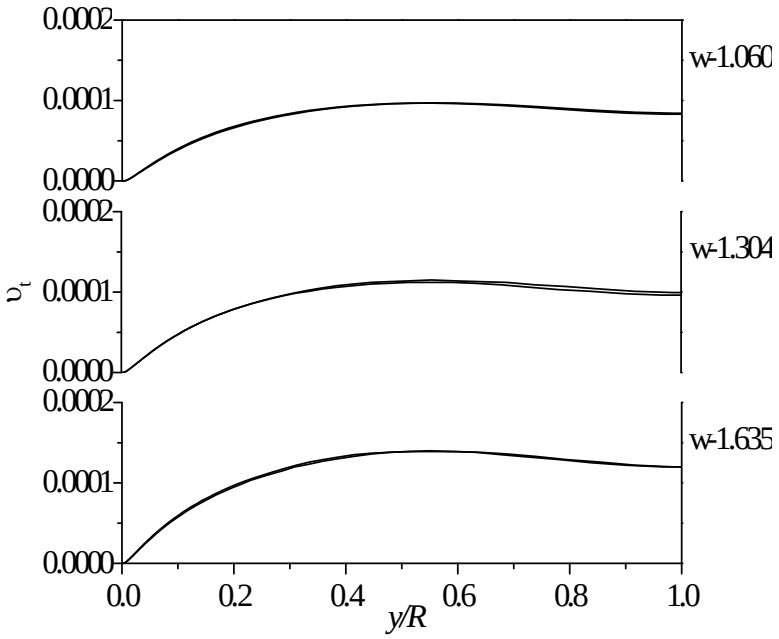

Figure 4.6 Eddy viscosity profiles for 1.79 mm expanded polystyrene particles at different total mass flow rates. Dashed lines represent the eddy viscosity predictions for a single-phase.

The eddy viscosity profiles for the expanded polystyrene particles, shown in Figure 4.6, resemble the ceramic particle profiles. The eddy viscosity increases at the centerline of the pipe as the total mass flow rate increases. The profiles for the present case are almost identical to the single-phase flow eddy viscosity distribution. The density of the particles and the bulk solids concentration (approximately 0.01) are the reasons for this behaviour.

4.2 Dense flow

The liquid-solid flow model was also investigated for concentrations ranging from 10 – 40%. The flow was investigated for five different particles transported through vertical

pipes of diameters 25.8 and 40 mm, at axial velocities in the range of $2 - 7\,\mathrm{ms}^{-1}$. The flow and particle properties are given in Table 4.2 and Table 4.3, respectively. The predictions for the mean solids velocity and concentrations were compared with the experimental data of Sumner *et al*. (1990).

Table 4.2 Flow properties for the dense flow case

1. Diameter of the pipe, D – 25.8 and 40.0 mm
2. Density of fluid, ρ_f – $997.09\,\mathrm{kgm}^{-3}$
3. Viscosity of fluid, μ_f – $0.001\,\mathrm{Nsm}^{-2}$

Table 4.3 Particle properties for the dense flow case

Particle	**diameter,** d_p (mm)	**density,** ρ_p (kgm^{-3})
Fine plastic	0.29	1050
Medium sand	0.47	2650
Coarse sand	0.78	2650
Coarse plastic	1.5	1050
Gravel	1.7	2650

Sumner *et al*. (1990) measured the solids mean velocity and concentration for six different sets of particles in vertical acrylic plastic pipes of diameters 25.8 and 40 mm.

An L-shaped conductivity probe and a wall probe were used to measure the local solids concentration and mean velocity. Measurements for dense liquid-solid flows were made for a variety of bulk solids velocities and concentrations (up to 50%).

4.2.1 Particle size effects

The effect of particle size on the mean velocity profiles is illustrated in Figure 4.7. The predicted mean velocity profiles for five different particles, with fine plastic and gravel being the finest and coarsest particles, respectively, in 40 and 25.8 mm acrylic plastic pipes are shown in Figure 4.7 (a) and (b). The bulk velocities of the particles in the 40 and 25.8 mm pipes were 4 and $3\,\mathrm{ms}^{-1}$, respectively, and the bulk concentration of the particles in both pipes was 10%. Note that in this section only mean velocity predictions are investigated. The model predictions will be compared to the experimental data in the later sections. It is seen from Figure 4.7 that for the fine plastic particles, which are the smallest among the five particles, the solids-phase velocity profile is the same as that of the liquid-phase, suggesting that the drag between the phases is minimal. However, with increasing particle size, the drag between the two phases is also observed to increase, with the coarsest gravel particles exhibiting a significant slip between the phases. This behaviour is physically realistic since smaller particles are lighter and follow the fluid flow, while larger particles are heavier and exhibit a slip velocity between the two phases.

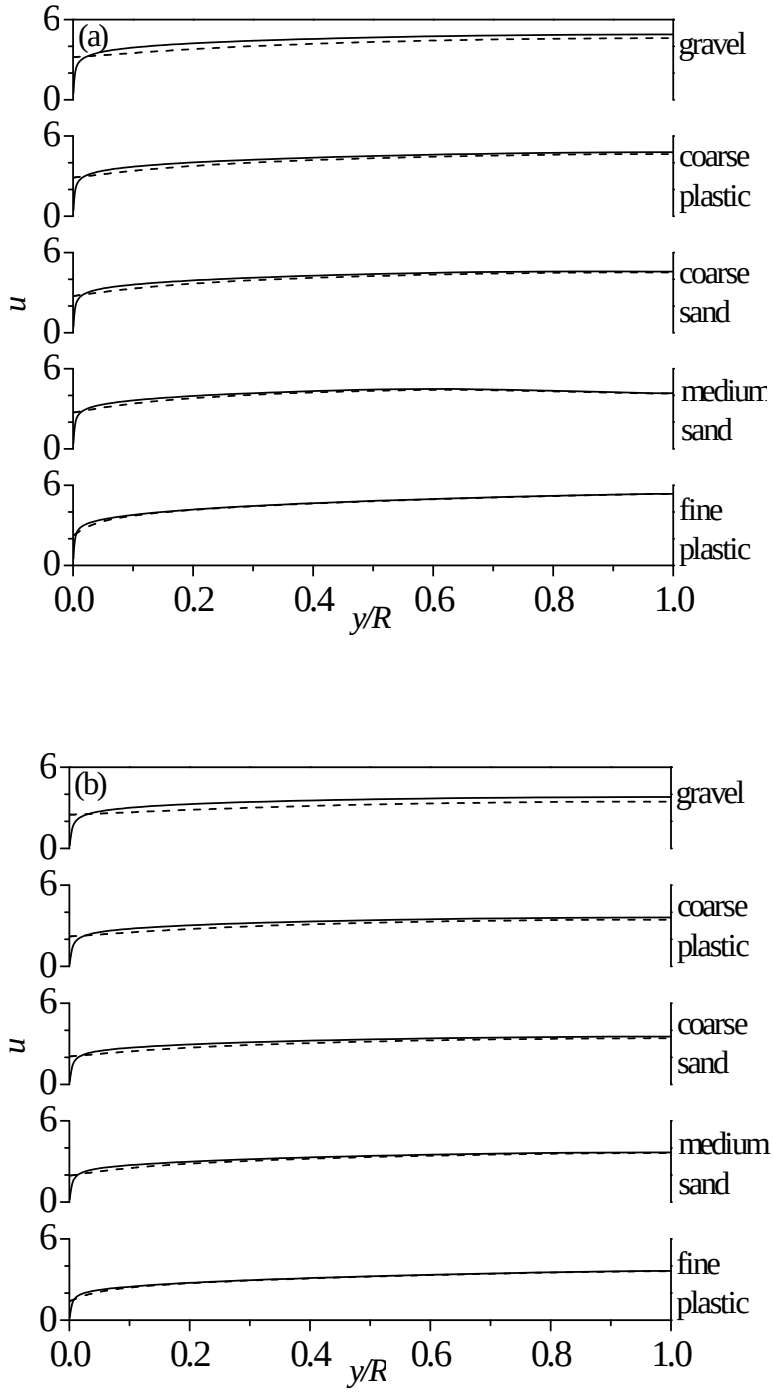

Figure 4.7 Particle size effects on mean velocity profiles for the numerical predictions in (a) 40 and (b) 25.8 mm acrylic plastic pipes for different particles and a bulk concentration of 10%. Solid and dashed lines represent the liquid- and solid-phase velocity predictions respectively.

Figure 4.8 presents the radial profiles of the mean solids velocity and concentration in a 40 mm vertical acrylic plastic pipe for a bulk solids velocity and concentration of $4\,\mathrm{ms}^{-1}$ and 10%, respectively. An agreement is observed to exist between the model predictions and the experimental data for the mean solids velocity shown in Figure 4.8 (a). The figure shows that the velocity distributions for all the particles are similar except that with increasing particle size a flatter velocity profile is assumed by the particles. It is seen from Figure 4.8 (a) that the velocity profiles for the coarsest gravel particles are flatter compared to the other velocity profiles.

The concentration predictions for different particles for the conditions specified (mean solids velocity and concentration of $4\,\mathrm{ms}^{-1}$ and 10%, respectively) are shown in Figure 4.8 (b). In general, the simulations show marginal agreement with the data. In the region closer to the centre of the pipe, the numerical results significantly over-predict the experimental data. This is because the solids concentration at the wall was under-predicted compared to the data and therefore, the solids concentration at the centre of the pipe was increased (input) to obtain bulk solids concentration of 10% for the flow case. Therefore, significantly higher values of solids concentration compared to the experimental data at the pipe centreline were predicted. In contrast, excellent agreement is seen to exist between the predictions and the data for the gravel particles at the centre region but not in the near-wall region. The data show that the concentration of the particles (gravel) is minimum at the wall, and increases toward the centre. The predicted concentration profile initially slightly decreases near the wall and then increases to a maximum value at the centreline.

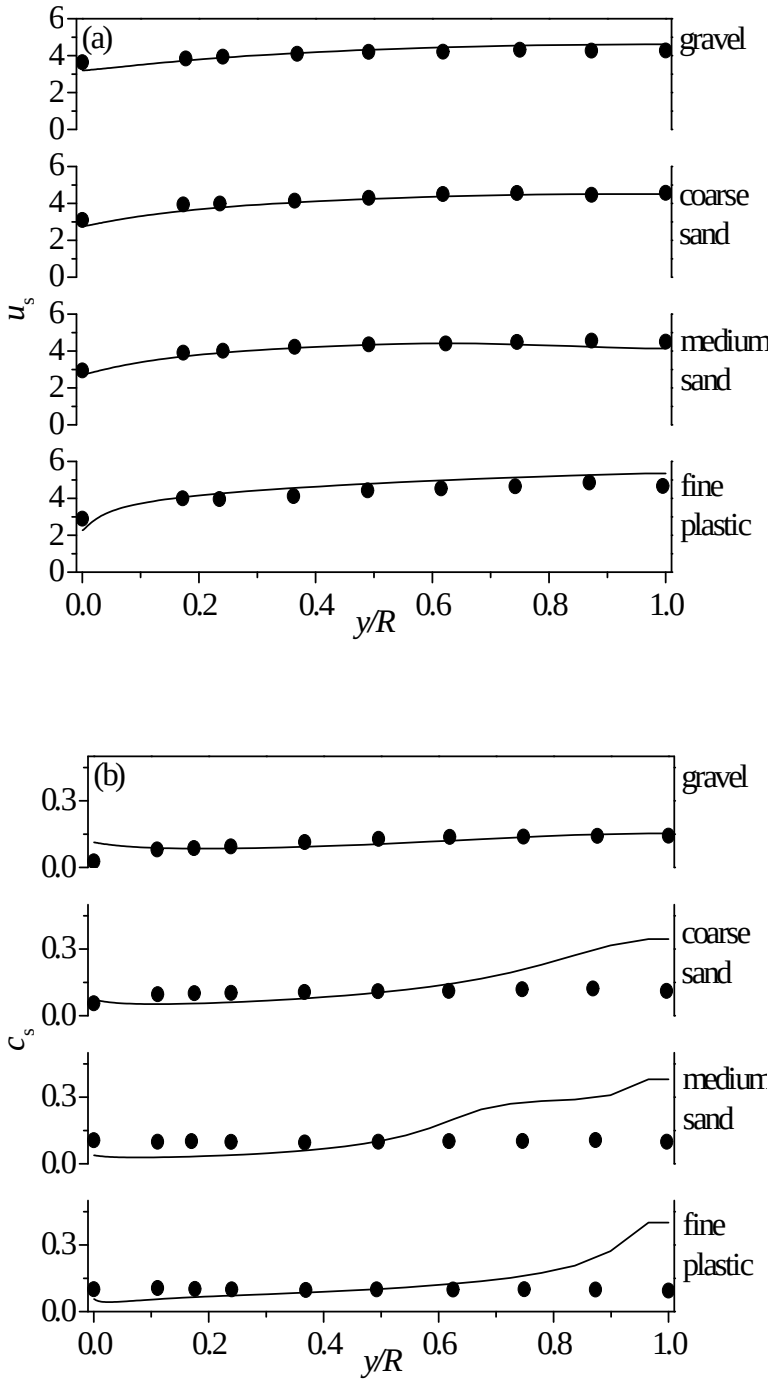

Figure 4.8 Comparison of (a) solids velocity and (b) solids concentration predictions for different particles in a 40 mm pipe for bulk velocity and concentrations of 4 ms^{-1} and 10% respectively. Closed symbols represent the data of Sumner *et al*. (1990).

The solids velocity and concentration distributions for different particles in the smaller 25.8 mm diameter acrylic plastic pipe are shown in Figure 4.9 and 4.10. The mean solids concentration in both figures is 10%, while the bulk solids velocities are 3 and $7\,\mathrm{ms}^{-1}$, respectively. The numerical predictions for the solids velocity and concentration are compared with the experimental data.

The predicted solids mean velocity profiles, shown in Figures 4.9 (a) and 4.10 (a), are in excellent agreement with the experimental data. The figures show that both the data and the predictions assume flatter profiles with increasing particle size, a behaviour which is more or less similar to that shown in Figure 4.8 (a). This leads to the conclusion that the mean velocity distribution is insensitive to the change in pipe diameter.

Figure 4.9 (b) and 4.10 (b) present solids concentration predictions for a bulk solids concentration of 10% and bulk solids velocities of 3 and $7\,\mathrm{ms}^{-1}$, respectively. Although reasonable agreement appears to exist between the levels of predicted concentration profiles and the experimental data, the predictions are missing the shape shown by the data in the near-wall region. The data show an increase in concentration from the wall to the centre of the pipe, while the predicted concentration profiles show a slight decrease in concentration near the wall, after which they increase and reach a maximum value at the centre. This behaviour of the concentration profiles warrants further investigation. In addition to the discrepancy in the near-wall region for smaller particles, differences between the data and the predictions also exist in the core region of the pipe.

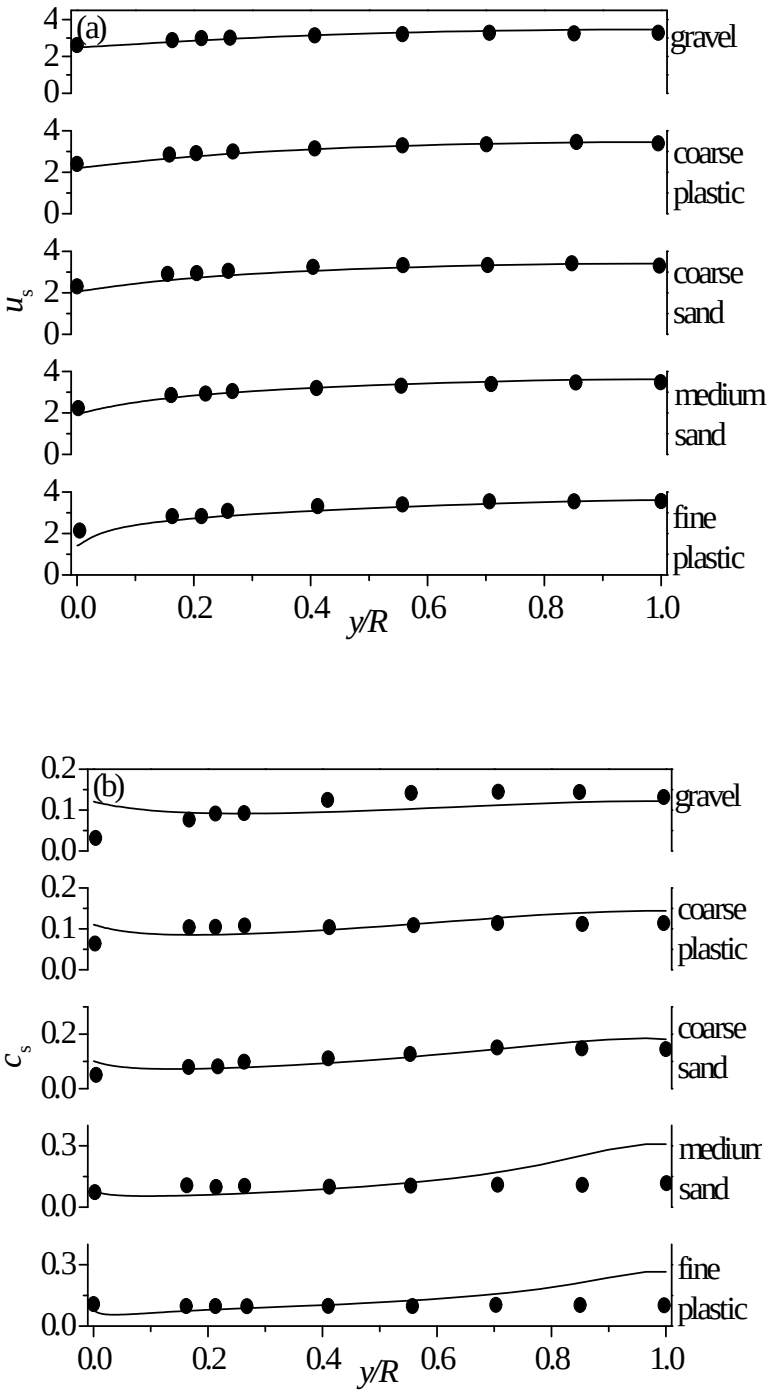

Figure 4.9 Comparison of (a) solids velocity and (b) solids concentration predictions for different particles in a 25.8 mm pipe for bulk velocity and concentrations of $3\,\mathrm{ms}^{-1}$ and 10%, respectively. Closed symbols represent the data of Sumner *et al*. (1990).

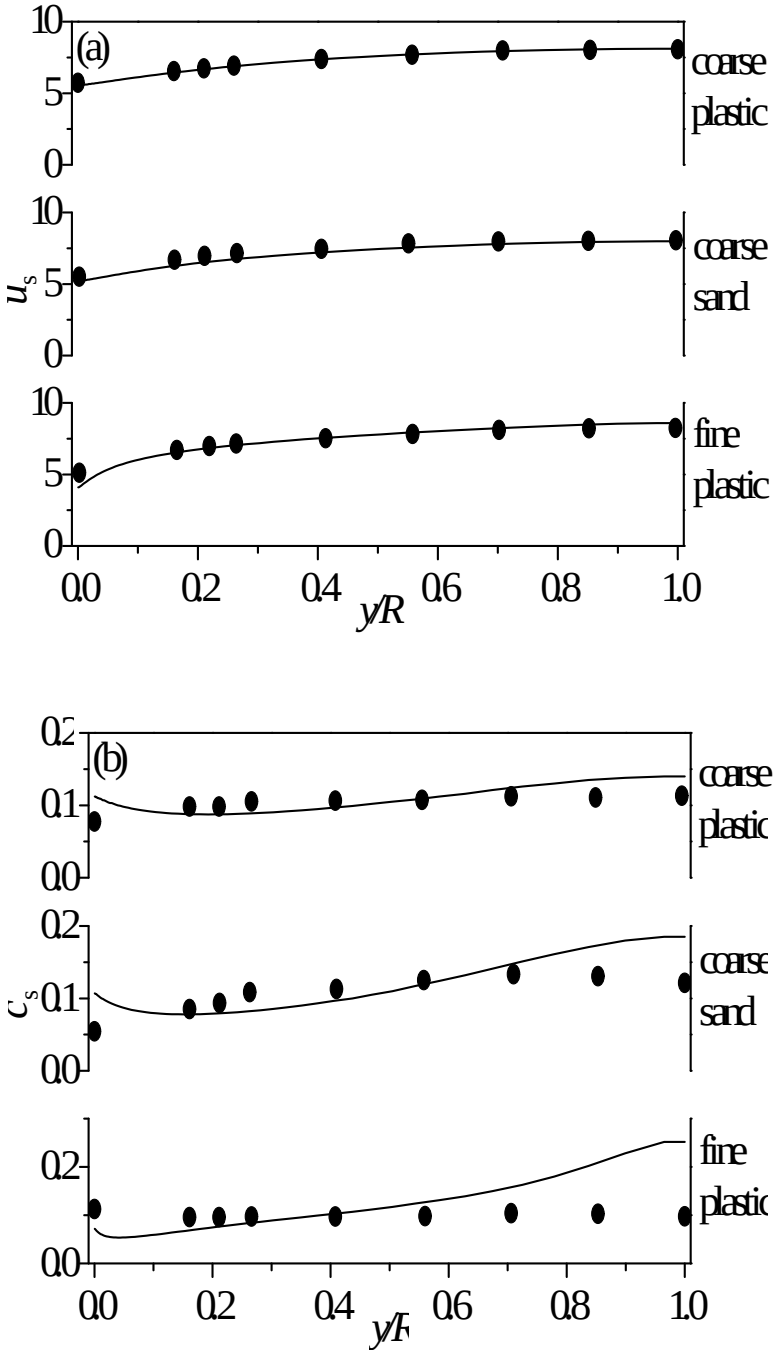

Figure 4.10 Comparison of (a) solids velocity and (b) solids concentration predictions for different particles in a 25.8 mm pipe for bulk velocity and concentrations of 7 ms^{-1} and 10%, respectively. Closed symbols represent the data of Sumner *et al*. (1990).

The numerical results significantly over-predict the experimental data at the centre of the pipe for the fine plastic and medium sand particles, shown in Figure 4.9 (b), and the fine plastic and coarse sand particles shown in Figure 4.10 (b), as did the solids concentration profiles observed in Figure 4.8 (b). The concentration profiles seem to be insensitive to the pipe diameter as were the velocity profiles.

4.2.2 Concentration effects

The effect of bulk solids concentration on the mean velocity and concentration profiles is explored in this section. Figure 4.11 shows the solids velocity and concentration predictions for coarse plastic particles and different bulk solids concentrations in a 40 mm pipe. Coarse plastic particles were used for investigating concentration effects, since the model predictions that agreed with the data were only obtained for this particular particle. The velocity predictions shown in Figure 4.101 (a) are in good agreement with the experimental data, as was the case with all the previous figures (Figures 4.8-4.10). Note the similar shape of the solids-phase mean velocity distribution for different concentrations. The concentration seems to have marginal effect on the velocity profile. The behaviour of the concentration profiles shown in Figure 4.11 (b) is similar to that shown in previous figures (Figures Figure 4.8-4.10). Note that the experimental profiles change shape as the bulk solids concentration increases but the predicted profiles do not. Surprisingly, the concentration predictions are in reasonable agreement with the experimental data, for the 40% case. However, the shape of the predicted profile is incorrect at the wall and the centreline.

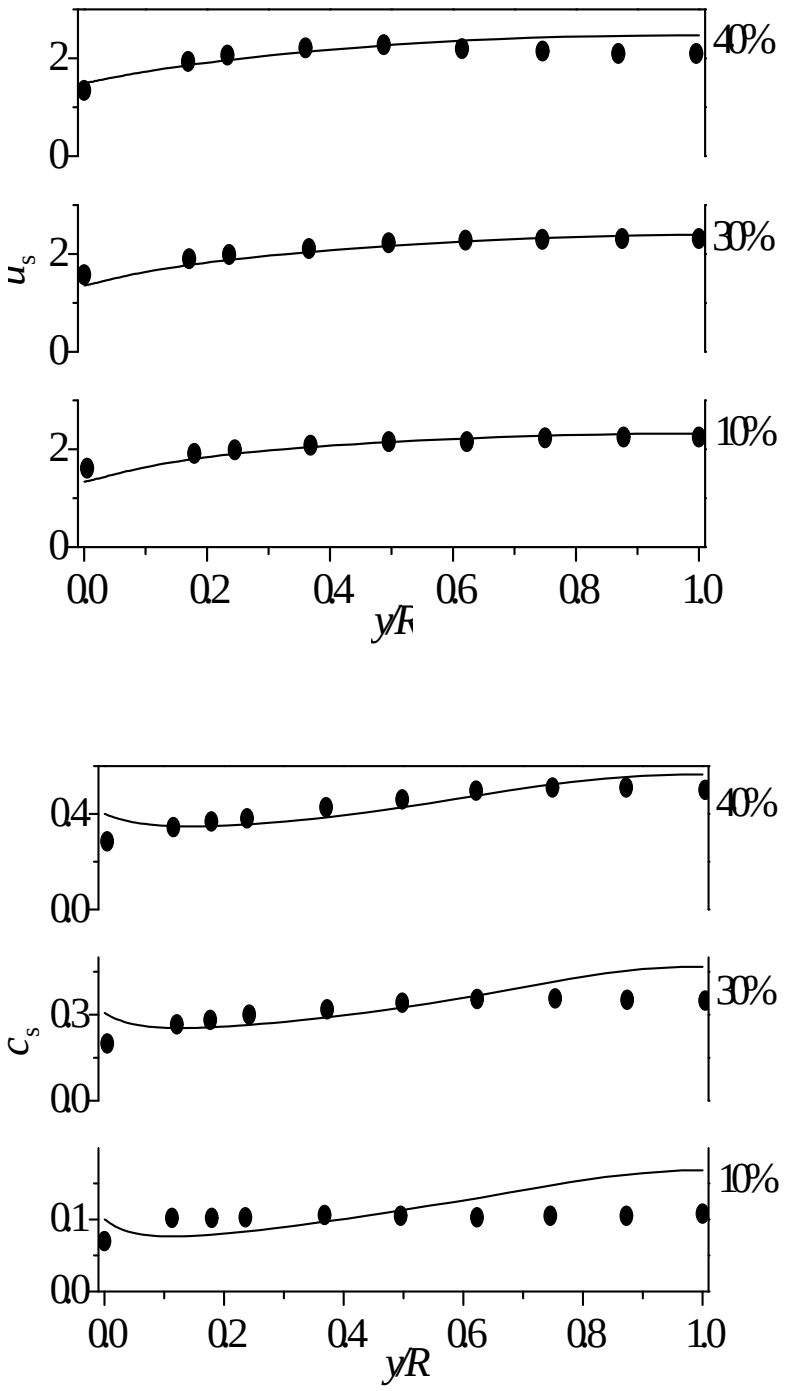

Figure 4.11 Comparison of (a) solids velocity and (b) solids concentration predictions for coarse plastic particles in a 40 mm pipe for different mean solids concentrations at a bulk velocity of 2 ms^{-1}. Closed symbols represent the data of Sumner *et al*. (1990).

4.2.3 Velocity fluctuations

Figure 4.12 shows the liquid-phase turbulence kinetic energy, *k*, and solids-phase granular temperature, *T*, predictions for different particles at bulk solids velocity and concentration of $4\,\mathrm{ms}^{-1}$ and 10%, respectively. It is seen from Figure 4.12 (a) that both turbulence enhancement at the centre and suppression in the near-wall region are observed with increasing particle size (fine plastic to gravel). For larger particles, i.e. coarse sand, coarse plastic and gravel, only turbulence enhancement is observed both at the centre and in the near-wall region (small enhancement), and the turbulence kinetic energy assumed a flatter profile. This behaviour is similar to that observed in the gas-solid flow of Tsuji *et al*. (1984).

As shown in Figure 4.12 (b), the *T* profile behaves similar to that of *k*. With increasing particle size, the granular temperature predictions assumed flatter profiles. Figure 4.12 (b) shows a reduced value of *T* in the near-wall region and an enhanced value at the centre of the pipe as the particle size increases. Note that since *T* influences c_s, through the radial balance equation (eq. 2.44), and the profiles of concentration are incorrect, perhaps the profiles of granular temperature are not realistic.

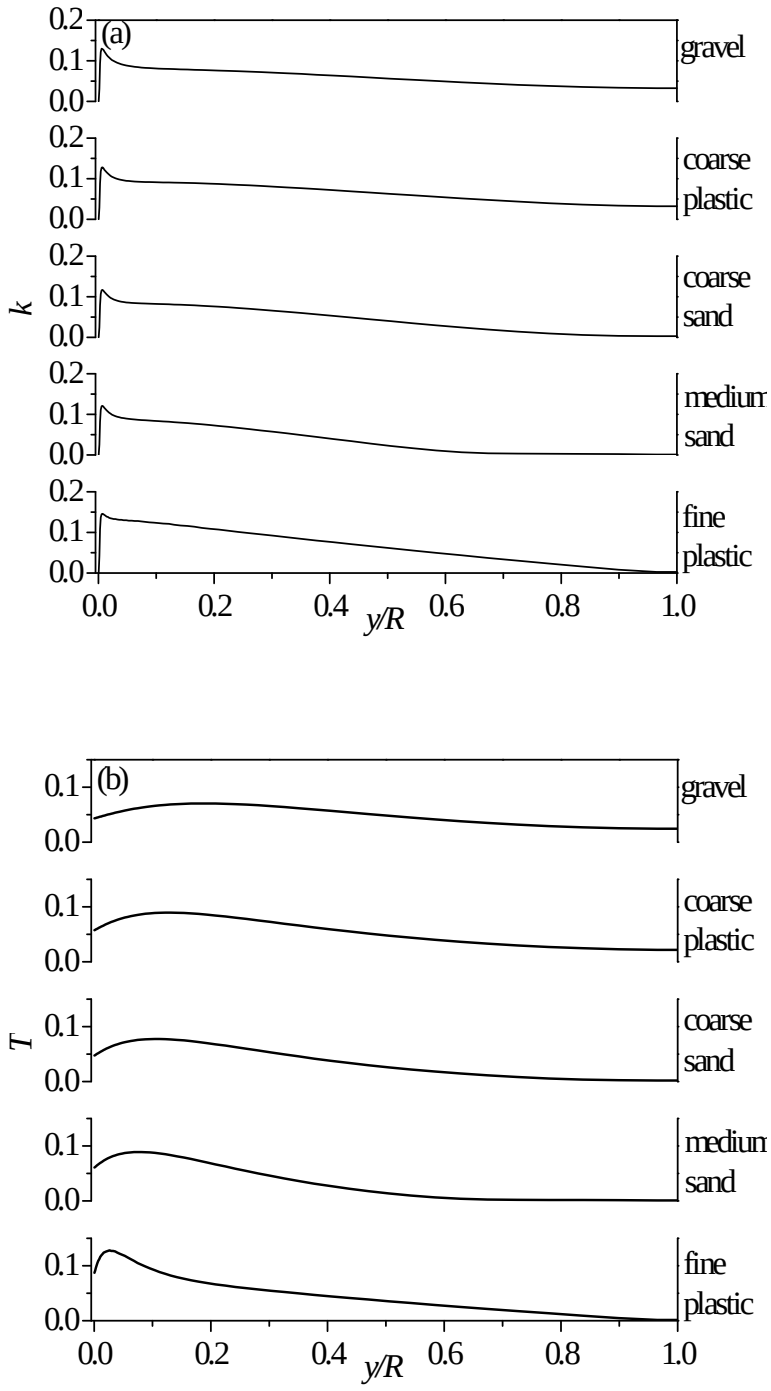

Figure 4.12 (a) Liquid-phase turbulence kinetic energy and (b) solids-phase granular temperature predictions for different particles in a 40 mm pipe for a mean solids concentration of 10% at a bulk velocity of $4\,\mathrm{ms}^{-1}$.

4.2.4 Eddy viscosity profiles

The eddy viscosity profiles predicted for different particles are shown in Figure 4.13. The bulk solids concentration and velocity are 10% and $4\,\mathrm{ms}^{-1}$, respectively. For the smaller fine plastic particles, the eddy viscosity is zero at the wall and gradually increases until $y/R \sim 0.4$. Thereafter it gradually decreases to approximately zero at the centre of the pipe. For the medium sand particles, the peak at $y/R \sim 0.30$ moves towards the wall, and the eddy viscosity is reduced to almost zero from $y/R \sim 0.55$ until the centre of the pipe. As particles of larger size were considered, the peak for the eddy viscosity again starts to shift towards the centre. A large increase in the eddy viscosity values was observed for the coarse plastic and gravel particles. The peak value of the eddy viscosity for both these particles was located at approximately $y/R \sim 0.6$, which then reduces slightly towards the centre of the pipe.

It is concluded from the liquid-solid flow mean and fluctuating velocity investigations that the present model, which was developed for dilute gas-solid flows, is inadequate when liquid-solid flows are considered. For the mean velocity predictions for both the dilute and dense flow cases, the greatest variation between the data and the predictions is 10%; however predictions for the solids mean concentration failed to match the data. The granular temperature profiles for the dilute flow case also failed to match the data, although it did follow the overall trend.

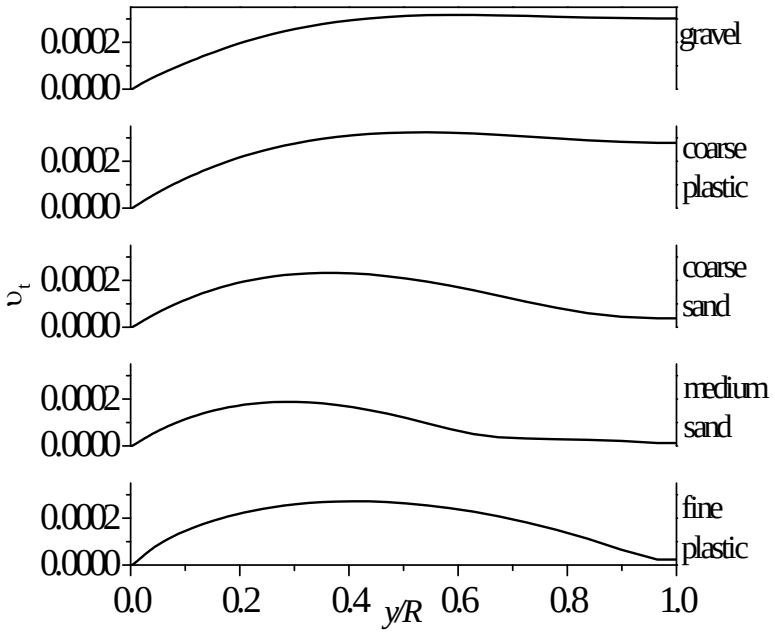

Figure 4.13 Liquid-phase eddy viscosity profiles for different particles in a 40 mm pipe for a bulk solids concentration and velocity of 10% and 4 ms^{-1}, respectively.

4.3 Pressure drop predictions

This section reports predictions for the liquid-solid flow pressure drop in a vertical pipe. The liquid-phase in this study was water and the particle phase consisted of coarse sand, polystyrene, and PVC granules of different sizes and concentrations. The particle properties are referenced in Table 4.4.

The predictions were compared with the experimental vertical pipe flow data of Shook and Bartosik (1994). They measured the liquid-solid flow pressure drop in two different PVC plastic pipes of diameters 26 and 40 mm. A magnetic flux flowmeter was used to

measure the bulk velocities for both phases while the pressure drop was measured using a calibrated variable reluctance transducer.

Table 4.4 Particle properties for the pressure gradient analysis

Particle	**diameter,** d_{p} (mm)	**density,** $\rho_{\mathrm{p}}\,(\mathrm{kgm}^{-3})$
Coarse sand	1.37	2650
Polystyrene	1.5	1045
PVC granules	3.4	1400

The relation used to calculate the pressure gradient following Shook and Bartosik (1994) is as follows:

$$-\frac{dp}{dz} = \rho_m g + i_m \rho_f g \tag{4.1}$$

where dp/dz is the pressure gradient, $\rho_m = \rho_f (1 - c_s) + \rho_p c_s$ is the mixture density and i_m is the frictional head loss of the liquid-solid mixture. For fully-developed pipe flow,

$$i_m \rho_f g = \frac{4\tau_{\mathrm{w}}}{D} \tag{4.2}$$

where the total shear stress, $\tau_{\mathrm{w}} = \left(\tau_f + \tau_p\right)_{\mathrm{wall}}$ is the sum of the fluid- and particle-phase wall shear stresses. For the two-fluid model used here, the fluid- and particle-phase wall shear stresses are calculated as follows:

$$\tau_f = (1 - c_s)\mu_f \left.\frac{du_f}{dy}\right|_{\mathrm{wall}} \tag{4.3}$$

$$\tau_s = \mu_s (wg_1 + g_2) \left. \frac{du_s}{dy} \right|_{\text{wall}} \tag{4.4}$$

The pressure gradient analysis for the liquid-solid flow is presented by plotting the mixture frictional head loss versus the mean mixture velocity, which is calculated by the following relation:

$$u_{\text{mix}} = \frac{1}{A} \int_A (u_f (1 - c_s) + u_s c_s) dA \tag{4.5}$$

Figure 4.14 shows the frictional head loss, i_m, predictions for coarse sand particles for different concentrations in a vertical pipe of diameter 26 mm compared with the experimental data of Shook and Bartosik (1994). The frictional head loss predictions for pure water, i.e. c_s = 0, in Figure 4.14 (a) were calculated using a single-phase flow with the $k - \varepsilon$ turbulence model of Myong and Kasagi (1990). In general, both the experimental data and predictions show that the friction increases with increasing mixture velocity and concentration. It is also observed that at constant i_m, the mixture velocity decreases as the bulk solids concentration increases. Good agreement exists between the model predictions and the data for the single-phase flow, as shown in Figure 4.14 (a). However, for higher mean solids concentrations, shown in Figure 4.14 (a) and 4.14 (b), the model under predicts the data. The slope of the predicted curve is also seen to be steeper than the experimental data for the 20 and 30% mean solids concentrations.

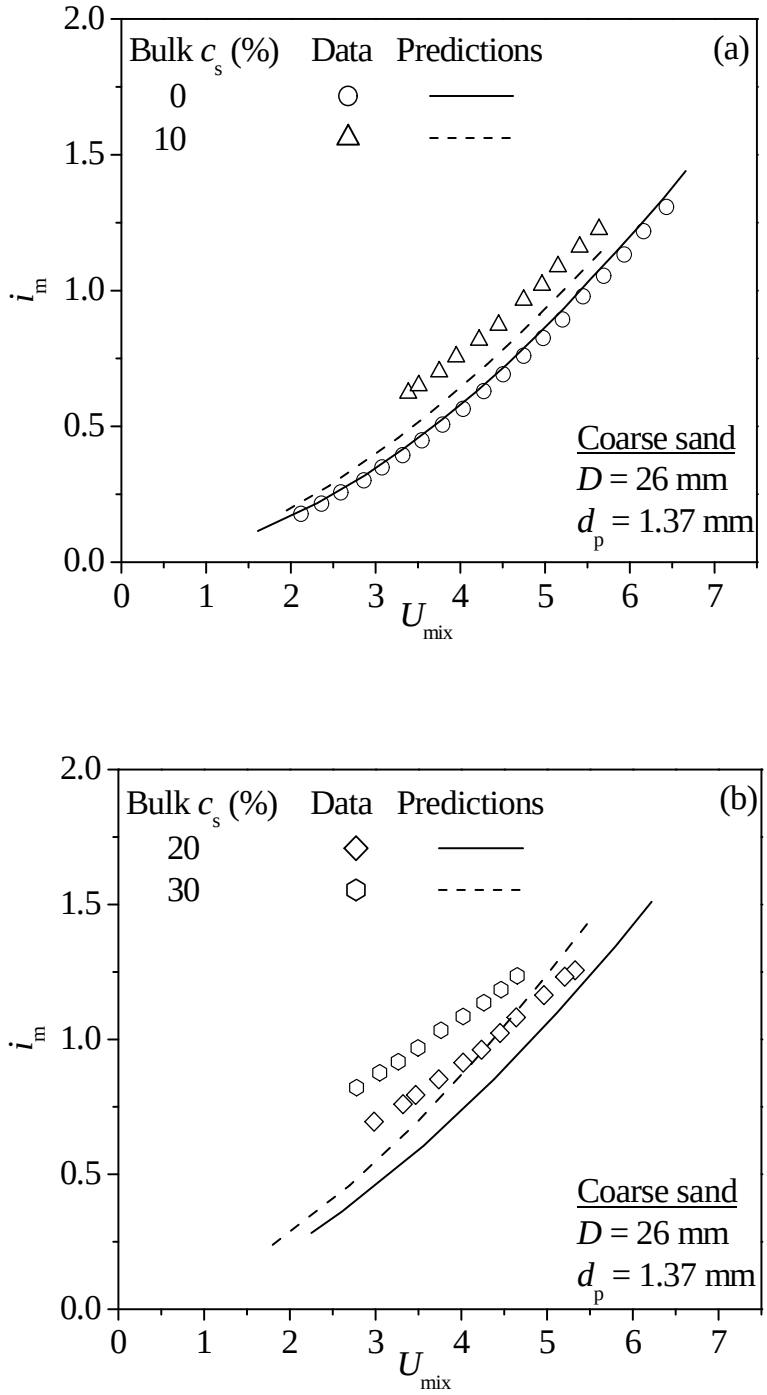

Figure 4.14 Comparison of the frictional head loss predictions for the coarse sand for (a) single-phase flow and 10% concentration, and (b) 20 and 30% concentrations with the experimental data of Shook and Bartosik (1994).

The frictional head loss predictions for polystyrene particles of size d_p = 1.5 mm for different solids concentrations are shown in Figure 4.15. The experimental data in Figure 4.15 show that i_m increases with increasing mixture velocity. The two-phase frictional head loss is almost equal to the single-phase at lower mixture velocities except for the 50% case, for which it is higher. It is also observed that the frictional head loss data for the cases where the bulk solids concentrations are 10 and 20% are slightly less than the single-phase flow data at high mixture velocities. According to Shook and Bartosik (1994), this may be due to the particle-phase effect on the fluid-phase wall shear stress. The model predictions for i_m in Figure 4.15 (a) and (b) significantly over-predict the data. It is observed from Figure 4.15 that the predicted solids-phase wall shear stress is a non-linear function of concentration as suggested by Shook and Bartosik (1994).

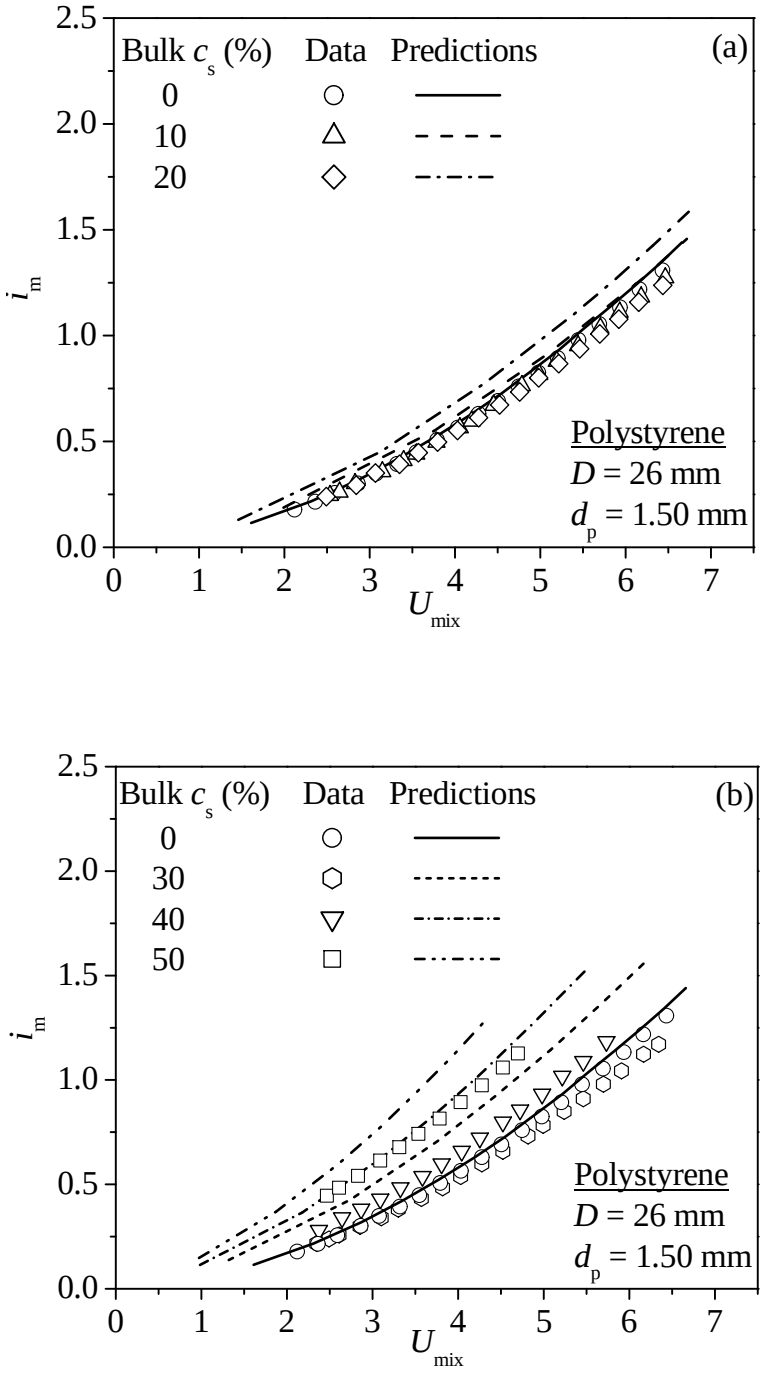

Figure 4.15 Comparison of the frictional head loss predictions for polystyrene particles for (a) Single-phase flow, 10% and 20% concentrations, and (b) 30, 40 and 50% concentrations with the experimental data of Shook and Bartosik (1994).

Figure 4.16 presents the frictional pressure drop predictions compared with the data for 3.4 mm PVC granules (ρ_s =1400 kgm^{-3}) in a vertical pipe of diameter 26 mm. It is seen from Figure 4.16 that the model over-predicts the experimental measurements for the PVC granules. It is observed from Figure 4.16 that the frictional head loss, which is the sum of wall shear stresses, τ_{w} , for the fluid and particle phases, increases non-linearly with solids concentration. This behaviour is verified in Figure 4.17, where predictions of τ_{w} for polystyrene particles of diameter d_{p} = 1.50 mm in a 26 mm pipe for different bulk solids concentration are presented. It is observed that as bulk solids concentration increases, both the fluid and particle wall shear stresses increase but in a non-linear fashion.

Some interesting observations based on Figures 4.14-4.16 are the dependence of i_m on particle density and particle size. The predicted and measured values of i_m are observed to increase with increasing particle density. As the particle size increases, for particles of the same density, i_m also increases.

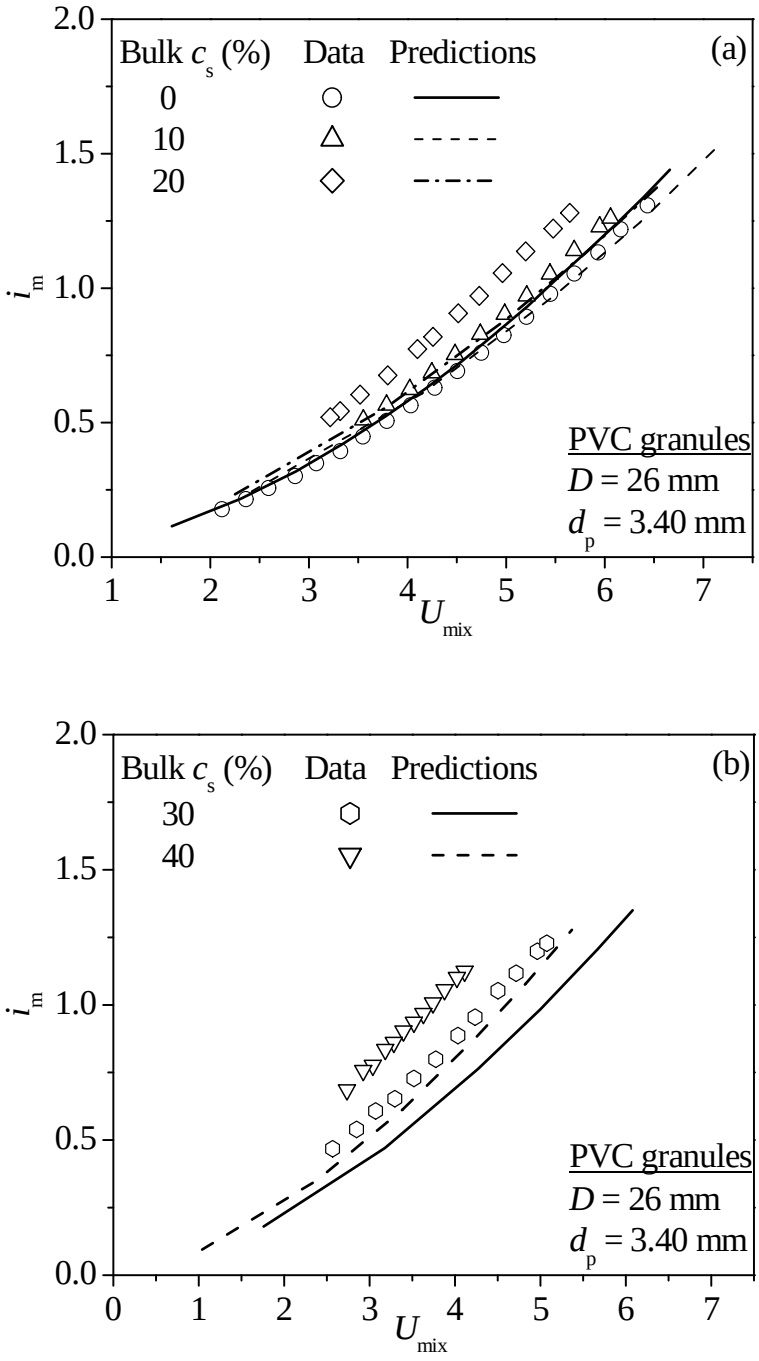

Figure 4.16 Comparison of the frictional head loss predictions for PVC granules for (a) single-phase flow, 10% and 20% concentrations, and (b) 30 and 40% concentrations with the experimental data of Shook and Bartosik (1994).

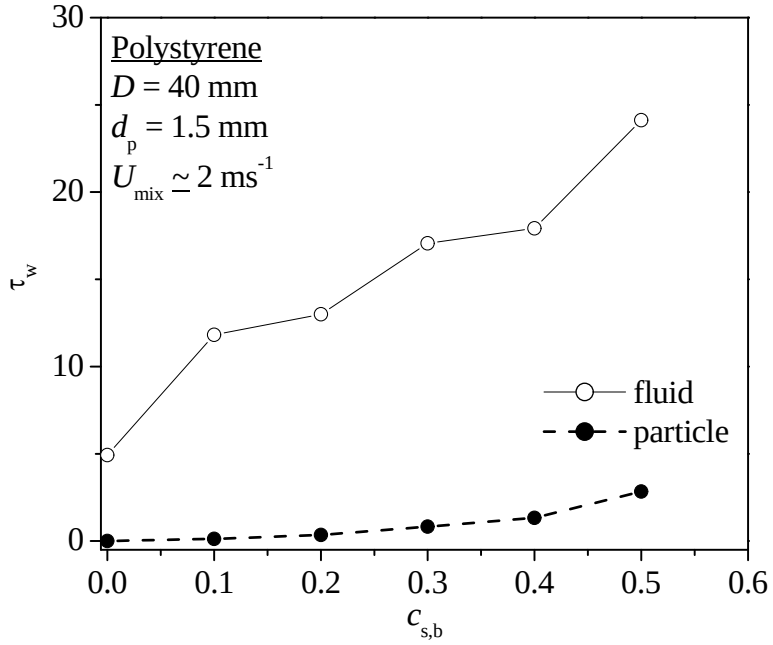

Figure 4.17 Effect of bulk solids concentration on wall shear stress for both phases for polystyrene particles of diameter d_p = 1.5 mm in a 40 mm vertical pipe.

The results for polystyrene particles of diameter 2.8 mm in a 40 mm vertical pipe are shown in Figure 4.18. It is observed from the figure that the data and the predictions for i_m increase with increasing mixture velocity but the data, unlike the predictions, retain the single-phase flow i_m values for bulk solids concentrations of 10 and 20%. Figure 4.18 (a) shows that the simulated results for the 10% case under-predict the experimental data at higher mixture velocities and the predictions for the 20% case are slightly higher than the data at lower mixture velocities but as mixture velocities increase, they reduce and become equal to the single-phase flow predictions. A reasonable agreement is observed to exist between the data and the predictions except for the 45% case where the simulation results were slightly under-predicted.

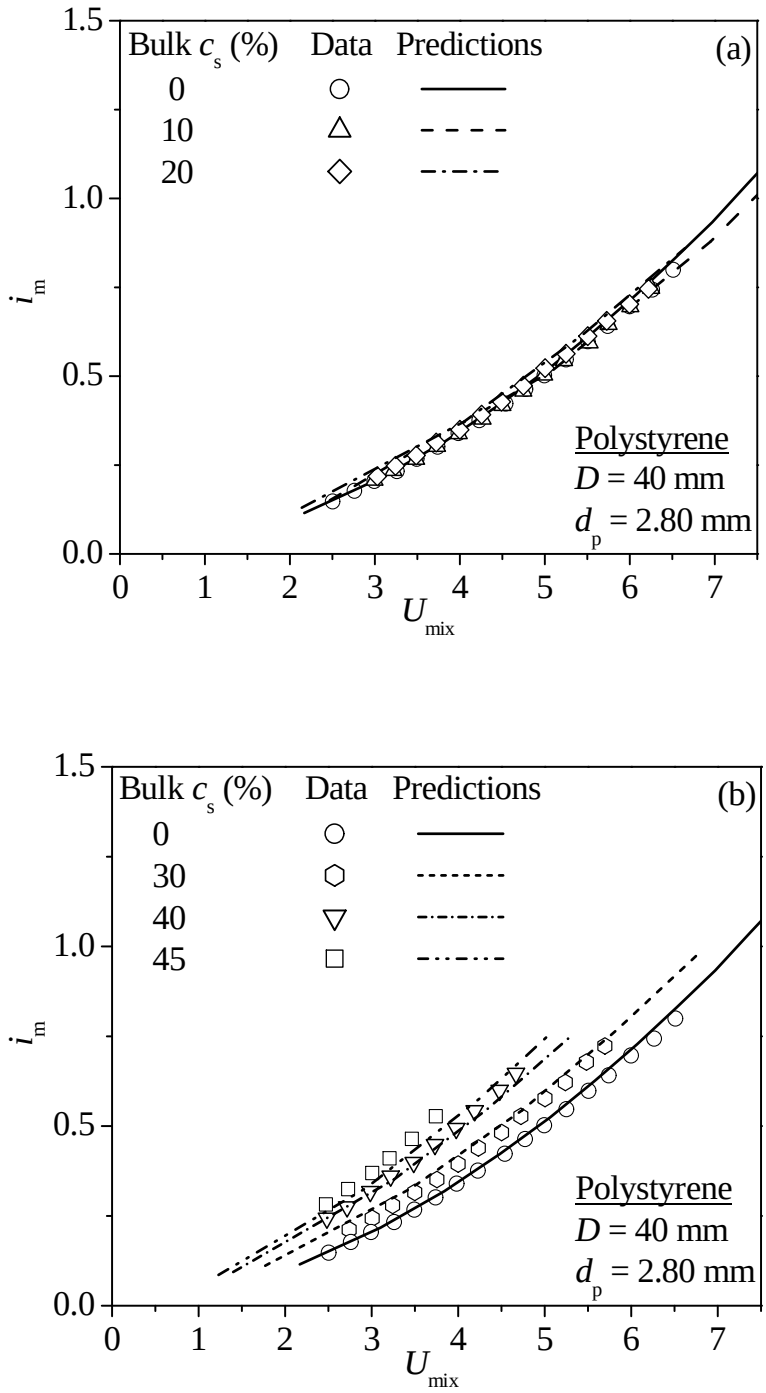

Figure 4.18 Comparison of the frictional head loss predictions for (a) single-phase flow, 10% and 20% concentrations, and (b) 30, 40 and 45% concentrations with the experimental data of Shook and Bartosik (1994).

It is concluded that the model significantly over-predicted the liquid-solid flow pressure drop measurements for all the particles investigated in this work. It is observed that at constant frictional head loss, i_m, the mixture velocity, U_{mix}, decreased as bulk solids concentration, $c_{s,b}$, increased and at constant U_{mix}, i_m increased as $c_{s,b}$ increased. A non-linear increase in the frictional head loss with increasing bulk solids concentration was observed from the predictions, which was verified through Figure 4.17. Overall, the two-fluid gas-solid flow model of Bolio *et al.* (1995), which was applied to the liquid-solid flow, was able to capture the trend shown by the experimental data but failed to match them.

5 HORIZONTAL FLOW

Introduction

A prediction for fully developed turbulent flow of a dense liquid-solid mixture in a horizontal channel using a two-fluid model is reported in this chapter. The simulations included inter-particle and particle-wall interactions. The mixture velocity and solids volume fraction (or concentration) predictions were compared with the experimental data of Salomon (1965) for different particle sizes and flow conditions. The mean velocities for both phases, solids-phase granular temperature and liquid-phase turbulence kinetic energy profiles for different flow conditions are also presented.

Salomon (1965) measured mean mixture velocities and solids concentrations for solid particles in the size range of 1.58 mm to 2.03 mm and densities of 2632 to 10838 kgm^{-3} in a horizontal rectangular channel. A flow divider that separates the flow into two streams was used to measure the mixture velocity. The volume flow rate of the lower stream was measured at different heights above the channel bed to determine the mixture velocity at different locations. A gamma-ray densitometer was used to measure the solids concentration. The study presents a large database of experimental data for the distribution of mixture velocity and solids concentration along the channel cross-section for seven different particles with different densities and sizes. However, in this study

only three particles were used, the properties of which are presented in Table 5.1. The remaining data sets involved packed beds.

Table 5.1 Particle properties for horizontal channel flow

Particle	**diameter,** d_p (mm)	**density,** ρ_p (kgm^{-3})
Sand 3	0.5283	2632.32
Sand 4	0.3505	2632.32
Sand 5	0.1524	2632.32

The governing equations were derived from a force balance on fluid and particle elements (shown in Appendix C) of a horizontal channel with a height H, the geometry for which is shown in Figure 5.1.

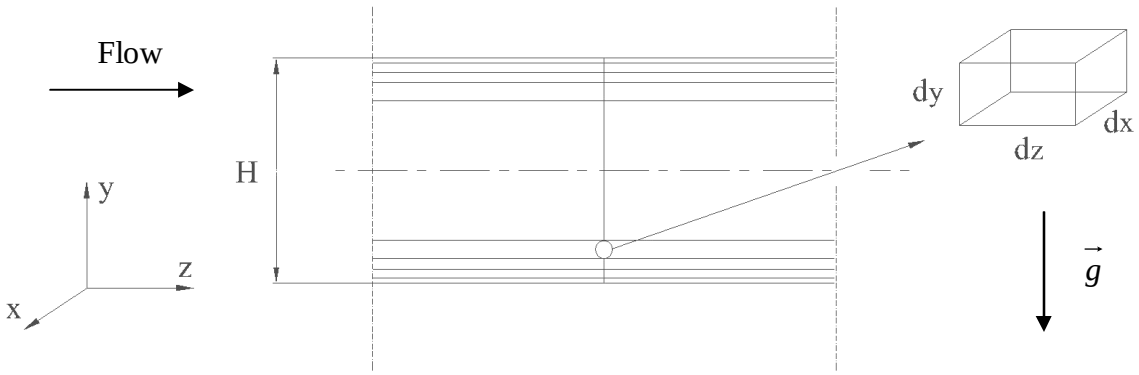

Figure 5.1 Horizontal channel geometry and differential fluid element

The transport equations for the fluid and solid phases are as follows:

$$0 = -\frac{\partial p}{\partial z} - \beta\left(u_f - u_s\right) + \frac{\partial}{\partial y}\left(\frac{\partial \tau_{xy}}{\partial y}\right) \tag{5.1}$$

$$0 = \beta\left(u_f - u_s\right) + \frac{\partial}{\partial y}\left(\frac{\partial \sigma_{xy}}{\partial y}\right) \tag{5.2}$$

$$0 = \frac{\partial \sigma_{yy}}{\partial y} - \rho_s c_s g \tag{5.3}$$

$$0 = -\sigma_{xy}\frac{\partial u_s}{\partial y} - \gamma + \beta\left(\overline{u'_{fi}u'_{si}} - 3T\right) - \frac{\partial}{\partial y}\left(\Gamma\frac{\partial T}{\partial y}\right) \tag{5.4}$$

In these equations, the fluid phase axial momentum balance is given by equation (5.1) while equations (5.2), (5.3) and (5.4) represent solids phase axial and radial momentum balance, and granular temperature, respectively. The closure expressions for the solid-phase stresses and granular temperature were adopted from the turbulent gas-solid flow model proposed by Bolio *et al.* (1995). The turbulence model equations used for the horizontal flow case are the same as those used for the turbulent gas-solid flow model given in Chapter 2. The flow domain (channel height of 25.4 mm) was meshed with a non-uniform grid using 60 control volumes. The mesh refinement was the same at both walls, and the grid was symmetric about the channel centreline (refer to Figure 5.1). A pseudo-transient solution method was considered and the field variables were advanced in time until a steady-state solution was obtained. A no-slip boundary condition was specified for the fluid-phase at both walls, while a flux boundary condition, adopted from Bolio *et al.* [1], was used for the solids-phase velocity and granular temperature at both walls. Simulations of the liquid-solid flow were performed for three different particle sizes and a variety of bulk mixture velocities and solids concentrations. The mixture velocity is calculated as follows:

$$U_{mix} = \frac{1}{A}\int_A \left(u_f\left(1 - c_s\right) + u_s c_s\right) \mathrm{d}A \tag{5.5}$$

5.1 Mean solids volume fraction profiles

The solids concentration/volume fraction predictions for particles of different sizes and bulk solids volume fractions were investigated. The solids concentration profiles are presented since the behaviour of the mean velocity profiles can be explained better by first studying the concentration predictions. Figure 5.2 shows solids volume fraction predictions for sand particles of size d_p = 0.1524 mm for mean solids concentrations and mixture velocities of 0.019, and 0.062, and 3.74 ms^{-1} and 3.66 ms^{-1}, respectively. The experimental data show a gradual increase in concentration with depth with a more rapid increase as the bottom wall of the channel is approached. The predictions show a somewhat different behaviour. The concentration is zero at the top wall of the channel, then increases to a local maximum at *y/H* ~ 0.1. Thereafter, it decreases and then sharply increases to a peak value at the bottom wall. It is thus observed from Figure 5.2 that the data indicates particles at the top wall while the model does not. Also, the data show a concave profile while the model predictions are convex (to the right) in nature in the bottom half of the channel. It is therefore concluded, from Figure 5.2, that the model predictions exhibit a more complex behaviour than shown by the experimental data.

The solids concentration profile for a bulk concentration of 0.084 is shown in Figure 5.3 (a). The behaviour of the predictions is similar to that exhibited in Figure 5.2. Figure 5.3 (b), shows predictions for a bulk solids concentration of 0.151, which exhibit a slightly different trend. The concentration is maximum at the bottom wall (> 50%), and then decreases by approximately 20% over a short distance. The profile is uniform for a small vertical distance, before gradually decreasing with height. Finally it exhibits a sharp

gradient reaching almost zero concentration at a height of approximately $y/H \sim 0.8$. The solids concentration in the lower half of the channel is very high, especially right at the wall, compared to the top half. Note that there were no data available for this particular case.

Figures 5.4Figure 5.4 and 5.5 show the predicted mean solids volume fraction profiles for sand 4 particles ($d_p = 0.3505$ mm) for different bulk solids concentrations compared with the data of Salomon (1965). The data show a different trend compared to the smaller sand 5 particles in the near-wall region at the bottom of the channel. A gradual increase in the solids concentration from the top of the channel is observed until a location where the concentration decreases slightly (about 2%) up to the wall. This local maximum is at a distance of $y/H \sim 0.05$ for the case where the bulk solids concentration is 0.043, which increases to approximately $y/H \sim 0.10$ for the case of $c_{s,b} = 0.139$. The solids volume fraction is zero at the top wall for the lower bulk concentration (0.043), but increases as bulk solids concentration increases. The model predictions, however, show behaviour similar to that for the sand 5 case, i.e. an almost zero concentration at the top of the channel which gradually increases with depth before reducing slightly and sharply increasing to a maximum value at the bottom wall. Note that the predictions in Figure 5.5 (b) show a profile that is similar to that in Figure 5.3 (b).

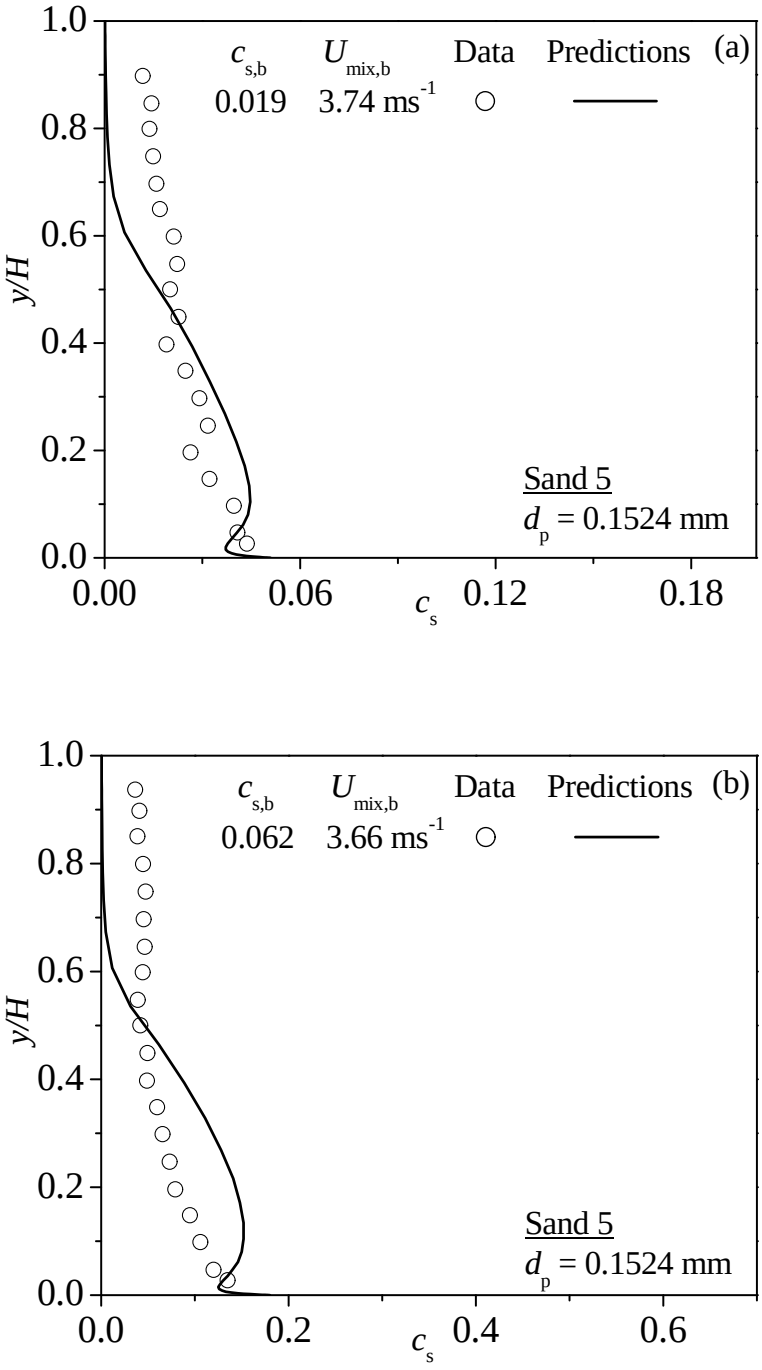

Figure 5.2 Mean solids volume fraction profiles for sand 5 particles for bulk solids concentrations of (a) 0.019 and (b) 0.062 compared with the data of Salomon (1965).

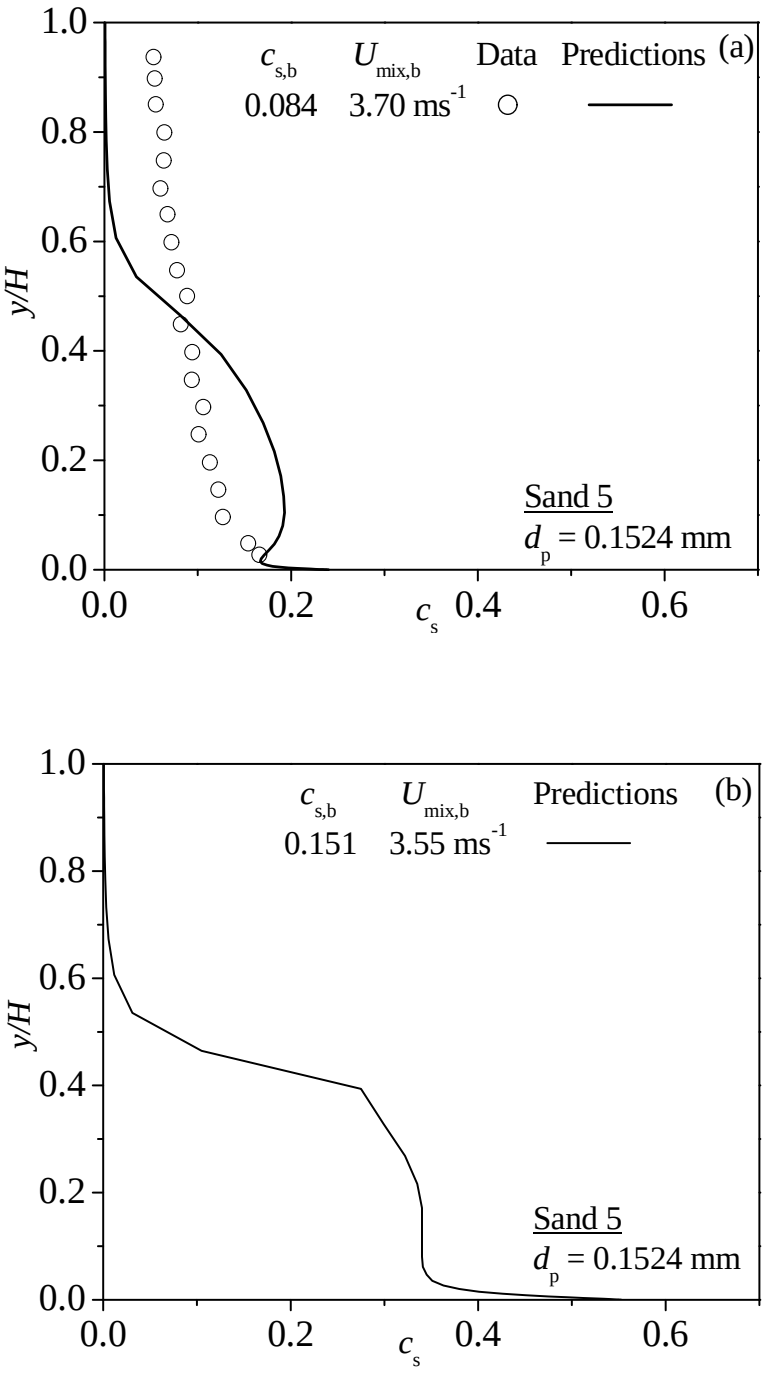

Figure 5.3 Mean solids volume fraction profiles for sand 5 particles for bulk solids concentrations of (a) 0.084 and (b) 0.151 compared with the data of Salomon (1965).

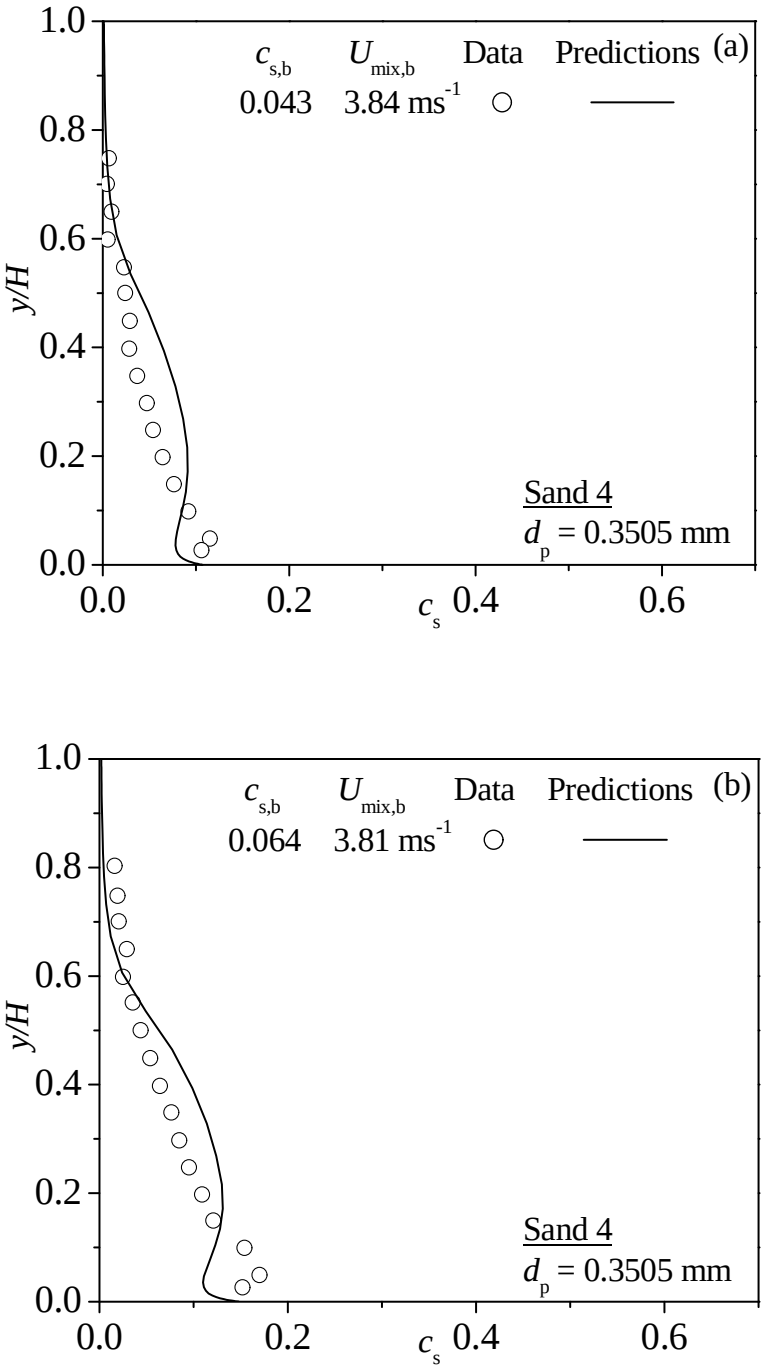

Figure 5.4 Mean solids volume fraction profiles for sand 4 particles for bulk solids concentrations of (a) 0.043 and (b) 0.064 compared with the data of Salomon (1965).

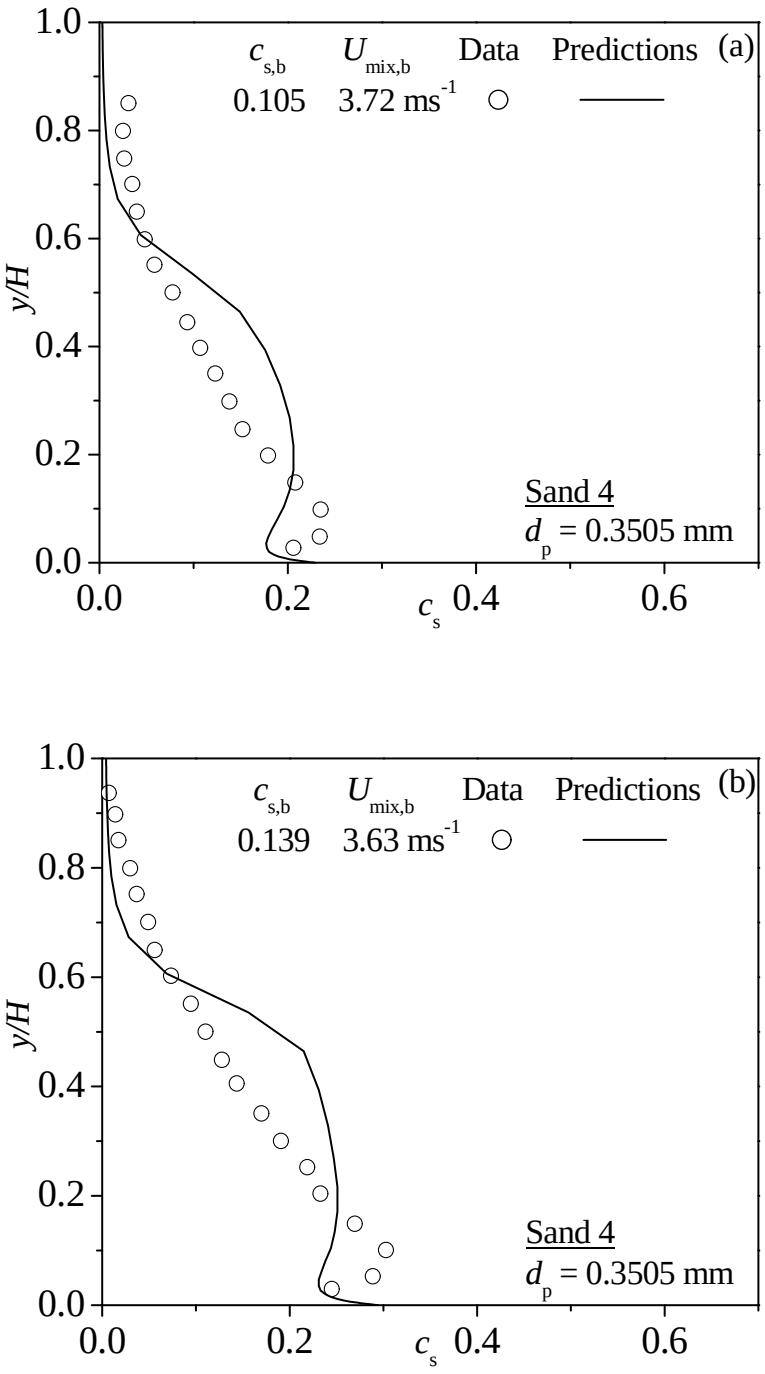

Figure 5.5 Mean solids volume fraction profiles for sand 4 particles for bulk solids concentrations of (a) 0.105 and (b) 0.139 compared with the data of Salomon (1965).

Figures 5.6 and 5.7 present the mean solids volume fraction profiles for 0.5283 mm sand particles (sand 3) for different bulk solids concentrations compared to the data of Salomon (1965). Both the data and the predictions in the figures show behaviour similar to that shown in Figure 5.4 and 5.5, but with a more extensive particle-free region. Another interesting observation that can be made from Figure 5.6 and 5.7 is that the model, unlike the previous cases (Figures 5.2 and 5.3), predicts higher concentration than the data in the top half of the channel. This may be due to the increase in the particle size.

The behaviour of the experimental data changes with bulk solids concentration for the bigger sand 4 and sand 3 particles, as seen from the above figures. At lower bulk solids concentrations, a particle-free region was predicted near the top wall which extended in size as the particle diameter increased. As the bulk solids concentration increased, the data indicate particles near the top wall. The model predicts particles throughout the channel for all cases. Overall, the behaviour of the predicted solids concentration is more complex than the experimental data.

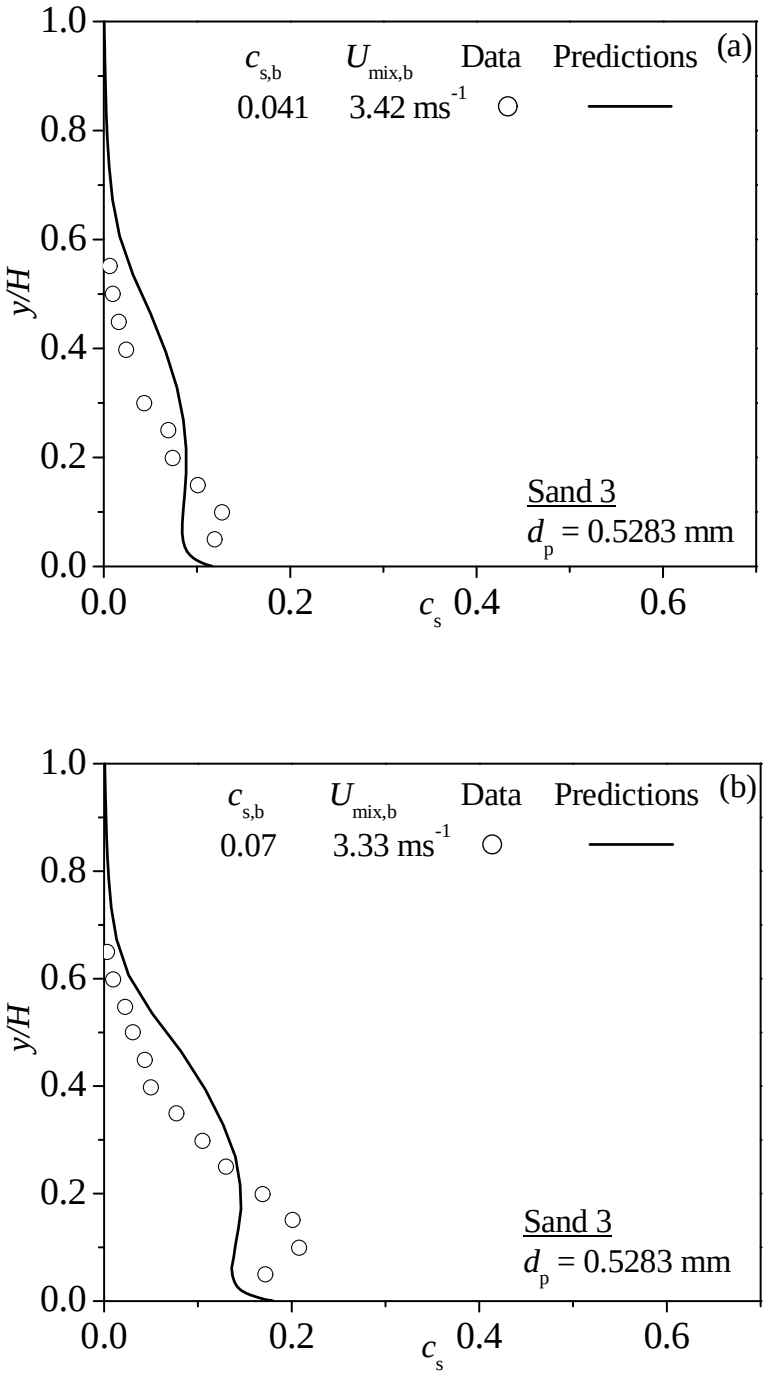

Figure 5.6 Mean solids volume fraction profiles for sand 3 particles for bulk solids concentrations of (a) 0.041 and (b) 0.070 compared with the data of Salomon (1965).

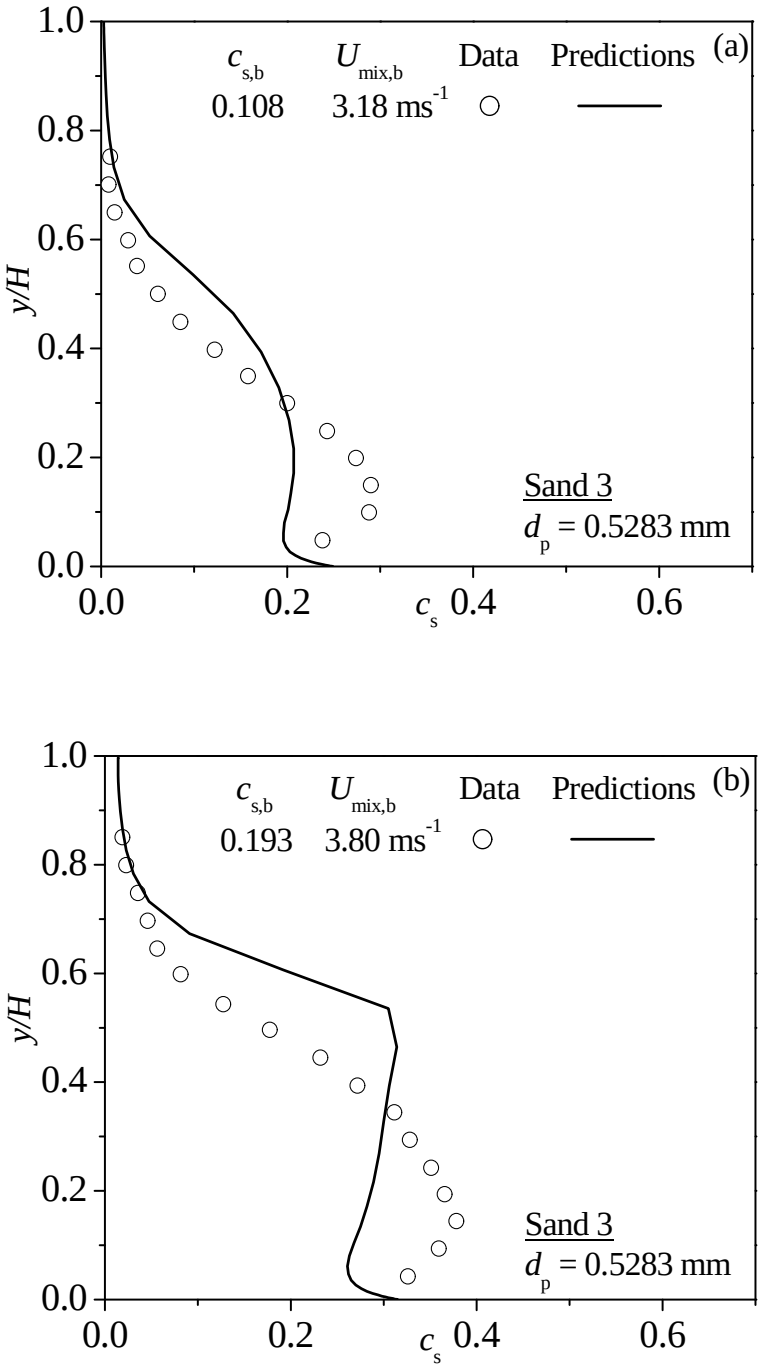

Figure 5.7 Mean solids volume fraction profiles for sand 3 particles for bulk solids concentrations of (a) 0.108 and (b) 0.193 compared with the data of Salomon (1965).

5.2 Mean velocity profiles

The mean velocity profiles for both phases for different particle sizes and mean solids concentrations are reported in this section. Figure 5.8 shows mean velocity profiles for sand particles of size d_p = 0.1524 mm (sand 5) for bulk solids concentration and mixture velocity of 0.019 and 3.74 ms^{-1}, respectively. The mean velocities for both phases are almost equal throughout the channel except in the near-wall regions where the solid particles have a higher velocity than the fluid. A single-phase mean velocity profile is also shown in Figure 5.8 (a). It is seen that unlike the single-phase mean velocity profile which is symmetric along the centreline of the channel, the velocities for both the phases are asymmetric with maximum values just above the centre of the channel.

An interesting observation from Figure 5.8 (b) & (c) relates to the behaviour of the velocity profiles in the near-wall region. The solids-phase velocity is finite and higher than that of the fluid at the top wall, shown in Figure 5.8 (b), and the bottom wall, seen from Figure 5.8 (b). Note that the difference in the mean velocities of the two phases is higher near the top wall than at the bottom. The reason for this can be understood from Figure 5.2 (a), which is the corresponding solids concentration profile. The predicted solids concentration at the bottom wall is observed to be much higher than at the top wall of the channel, which results in higher drag, hence, the slower movement of the mixture in the near-wall region at the bottom wall. Therefore, even though the solids velocity is higher than the fluid at the bottom wall, it is comparatively lower than that at the top wall.

Figure 5.8 (d) shows mean velocity profiles for the sand 5 particles for a higher bulk solids concentration of 0.151. It is seen that both phasic velocity profiles now exhibit a steep gradient in the lower half of the channel unlike the case with the lower 0.019 concentration (Figure 5.8 a). This can be understood from the solids volume fraction profiles for both cases (Figures 5.2 and 5.3). The concentration in the bottom half of the channel for the 0.151 case (from y/H ~ 0.4 to 0), shown in Figure 5.3 (b), is approximately 0.3 which then increases to 0.53 at the bottom wall. Thus, the lower half gradually becomes more dense which results in sharp velocity gradients in the region below the centre of the channel.

Figures 5.9 and 5.10 present mean velocity profiles for both phases for larger particles with d_p = 0.3505 mm and 0.5283 mm, respectively, and for a range of concentrations. The behaviour of the profiles is similar to that of the sand 5 particles, i.e. uniform velocity profiles for the cases where the solids concentration is low and a sharp gradient in the lower half of the channel for higher concentrations.

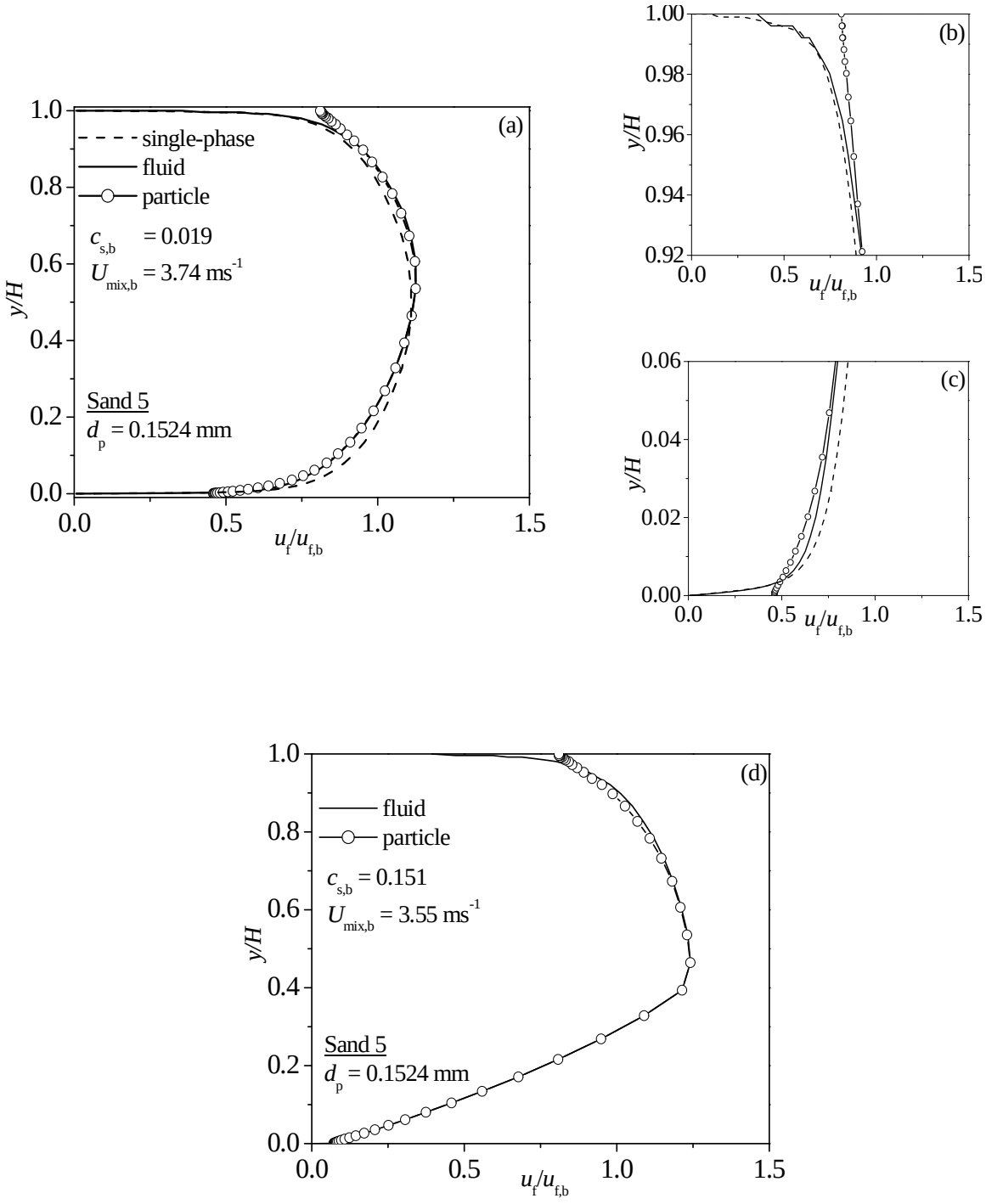

Figure 5.8 Mean velocity profiles for sand 5 particles for bulk solids concentrations of (a), (b) & (c) 0.019, and (c) 0.151 compared with the data of Salomon (1965).

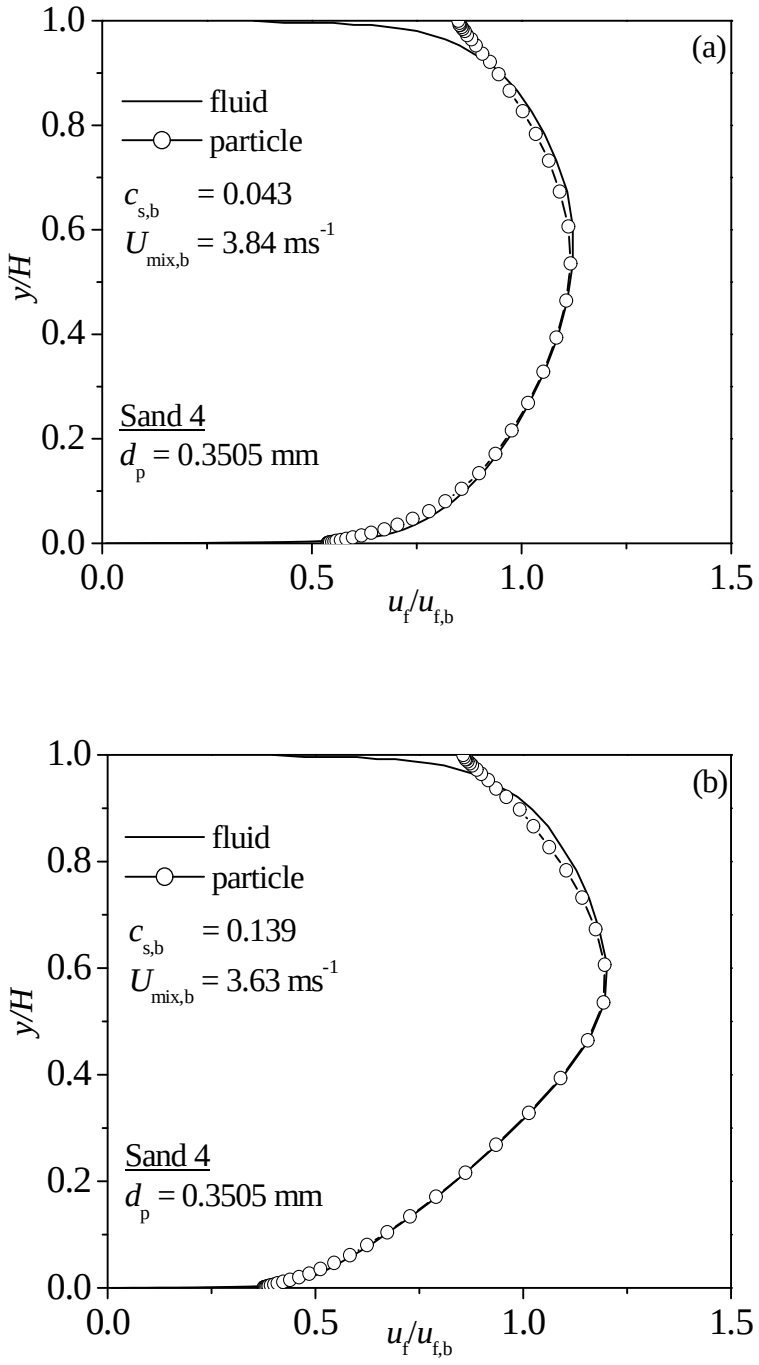

Figure 5.9 Mean velocity profiles for sand 4 particles for bulk solids concentrations of (a) 0.043 and (b) 0.139 compared with the data of Salomon (1965).

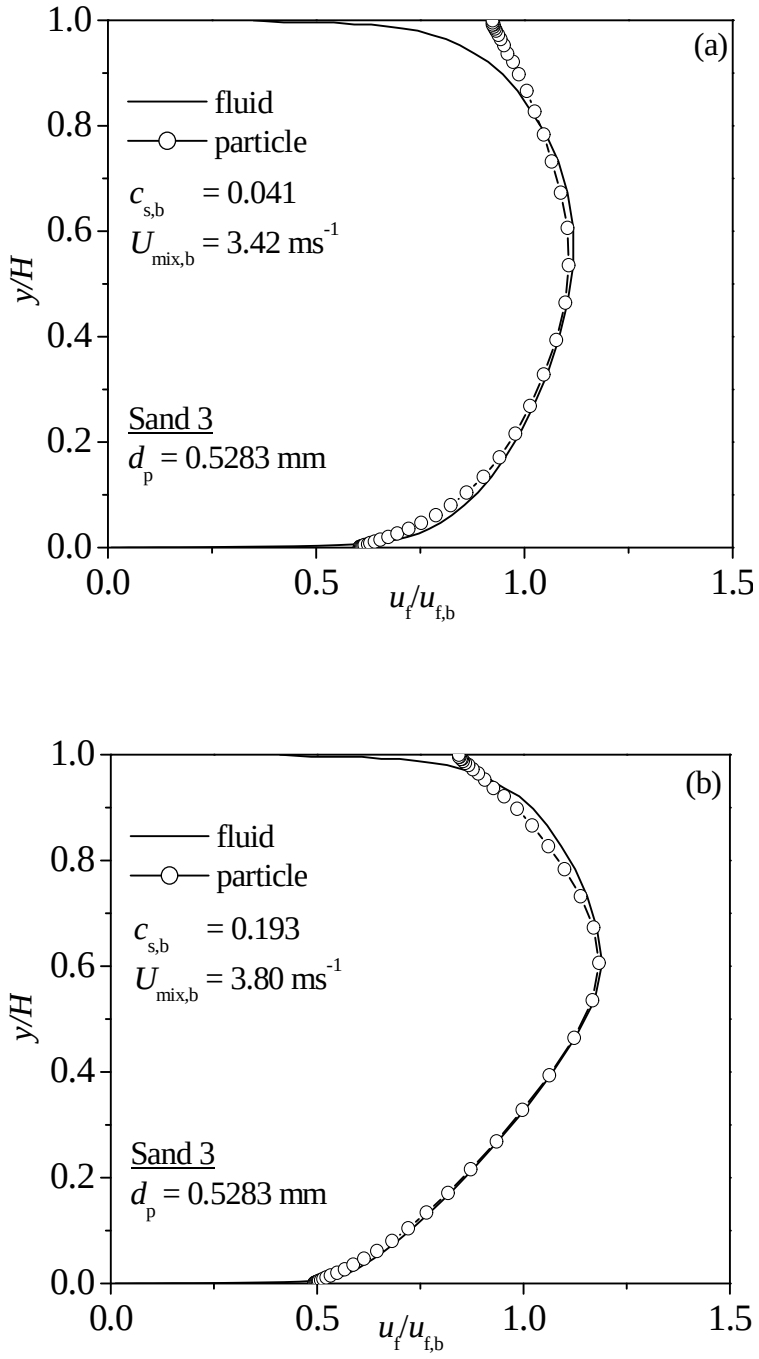

Figure 5.10 Mean velocity profiles for sand 3 particles for bulk solids concentrations of (a) 0.041 and (b) 0.193 compared with the data of Salomon (1965).

5.3 Mixture velocity profiles

The mixture velocity profiles for different particle sizes and solids volume fractions are presented in this section. Figure 5.11 shows the predictions for sand 5 particles of size d_p = 0.1524 mm for bulk solids concentrations and mixture velocities of 0.084 and, 0.151, and 3.70 ms^{-1} and, 3.55 ms^{-1}, respectively. The single-phase mean velocity profiles for similar flow conditions are included in Figure 5.11 (a). The single-phase velocity profile is symmetric with respect to the centre of the channel but the mixture velocity profile is asymmetric due to the addition of particles. Only partial agreement was observed between the data and the predictions. Both the predictions and the measurements show a peak value (i.e. maximum mixture velocity) near the centre of the channel. The model prediction is slightly above the measured peak location in Figure 5.11 (a) and vice versa in Figure 5.11 (b).

An interesting observation from Figure 5.11 is that the model predicted a sharp velocity profile in the lower half of the channel. This can be understood by observing the corresponding concentration profile (Figure 5.3) for the sand particles. The concentration increases as the bottom wall is approached and has a maximum value at the bottom wall of the channel. This result in a greater reduction of the mixture velocity at the bottom wall compared to the top wall, where the concentration is lower.

Figure 5.12 and Figure 5.13 present the mixture velocity profiles for sand 4 and sand 3 particles with d_p=0.3505 mm and 0.5283 mm, respectively, compared with the data of Salomon (1965) for different solids concentrations. The behaviour of the profiles is

similar to that shown in Figure 5.11. Both the data and model predictions show that the maximum velocity shifts above the centre of the channel as the particle size increases. The predicted mixture velocity profile becomes less steep as particles of larger size are considered. The simulated mixture velocity always over predicted the data near the top wall.

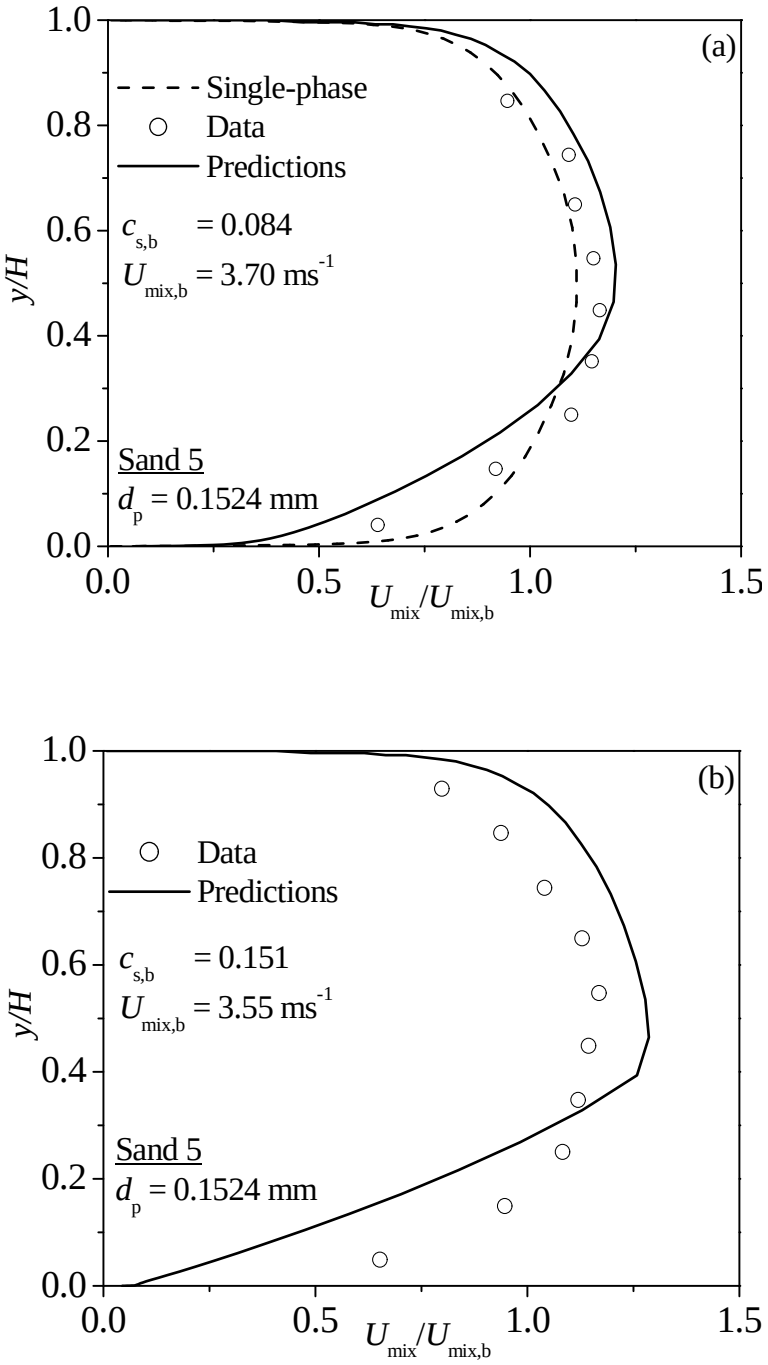

Figure 5.11 Mixture velocity profiles for sand 5 particles compared with the experimental data of Salomon (1965) for bulk solids concentrations of (a) 0.084 and (b) 0.151

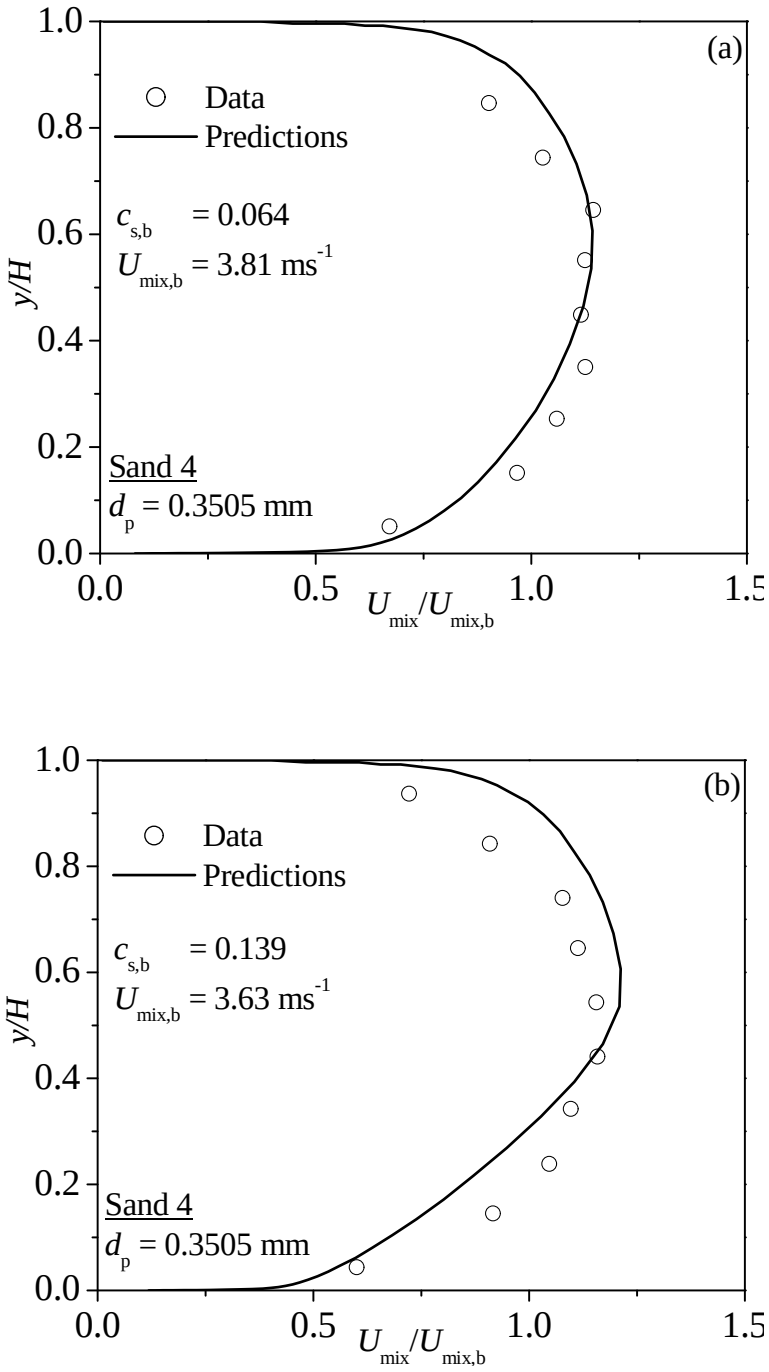

Figure 5.12 Mixture velocity profiles for sand 4 particles compared with the experimental data of Salomon (1965) for bulk solids concentrations of (a) 0.064 and (b) 0.139

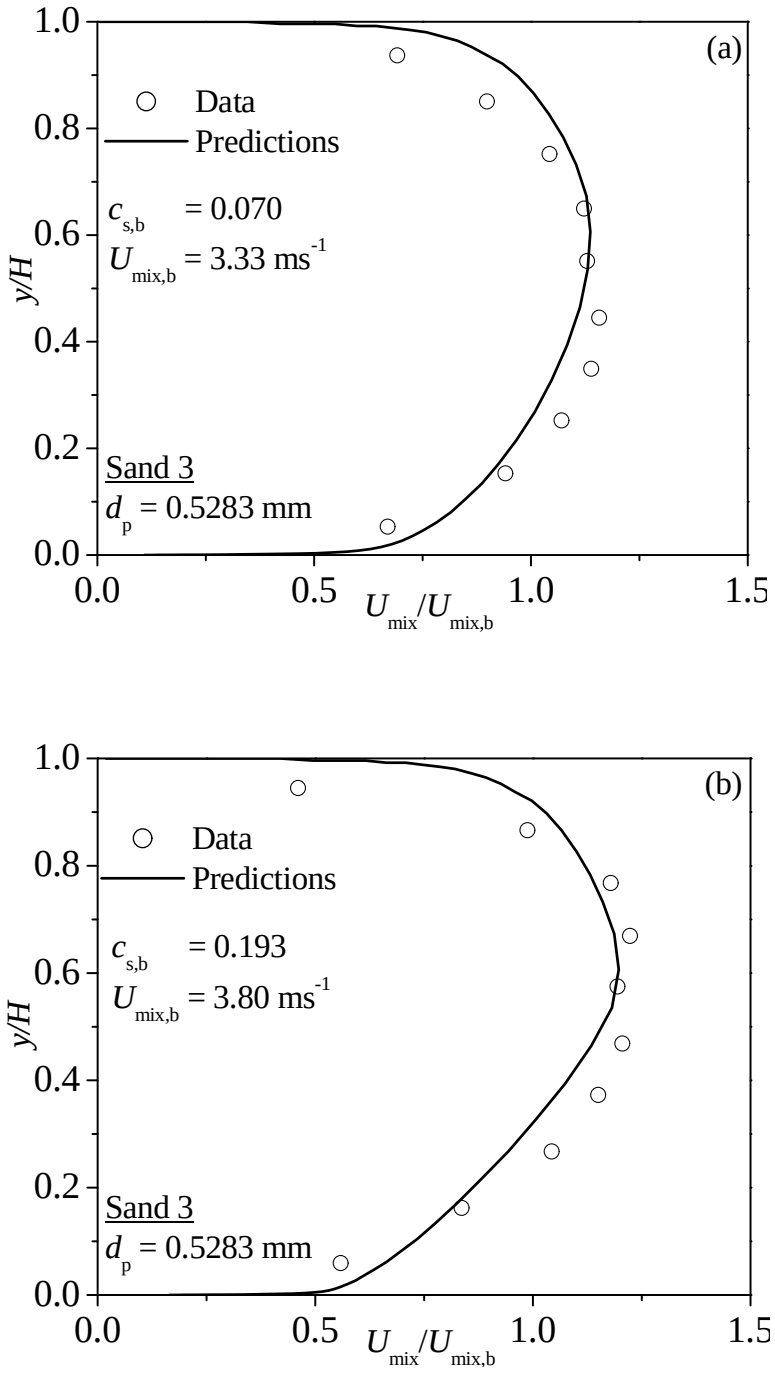

Figure 5.13 Mixture velocity profiles for sand 3 particles compared with the experimental data of Salomon (1965) for bulk solids concentrations of (a) 0.070 and (b) 0.193

5.4 Granular temperature predictions

Figure 5.14 shows granular temperature, *T*, predictions for sand particles of different size for different concentrations. The granular temperature predictions for all three sizes of sand particles are essentially similar. The profiles have a minimum value at the bottom wall, then increase to a local maximum after which they decrease to a local minimum near the centre of the channel, and finally attain a maximum value at the top of the channel. This behaviour is most likely due to the production term (2^{nd} term on the right hand side of eq. 2.44), the profile of which is presented in Appendix D.

It can be observed from comparing Figures 5.2 – 5.7 (solids volume fraction profiles) to Figure 5.14 (*T* profiles) that the behaviour of the granular temperature is in general opposite to that of the solids volume fraction. The predicted solids volume fraction is minimum at the top wall whereas the solids granular temperature is maximum close to the top wall. At the bottom wall, where the solids granular temperature is maximum, the granular temperature is typically less than at the top wall. The reason for this behaviour can be understood from the radial balance equation (equation 2.37), which shows that an inverse relation exists between the solids granular temperature and concentration. Figure 5.14 also shows that in general the granular temperature decreased as the mean solids volume fraction increased, i.e. with increasing solids concentration, the solids velocity fluctuations were reduced. Note that the change in granular temperature with changes in diameter and bulk solids concentration is not completely uniform.

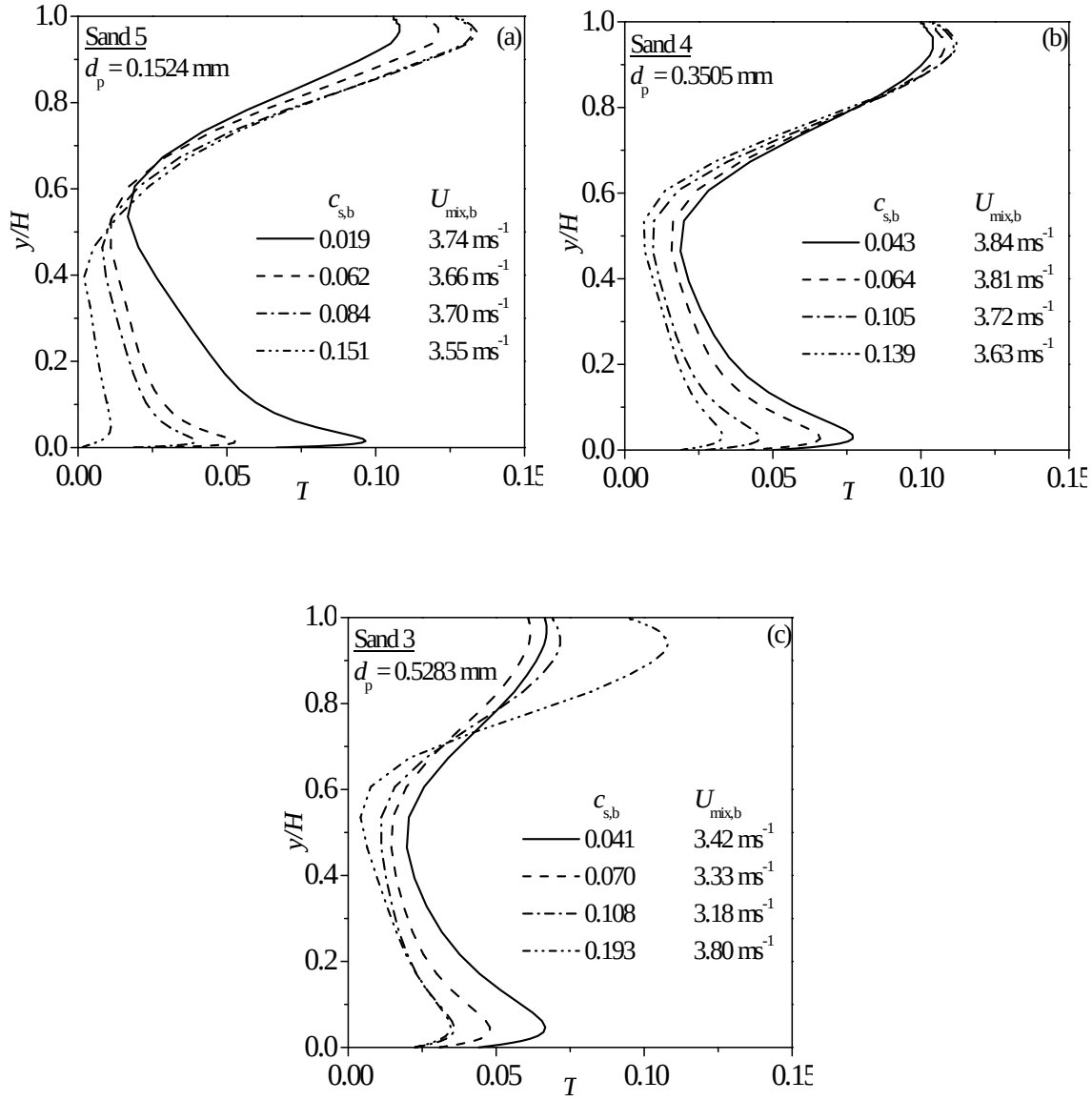

Figure 5.14 Granular temperature profiles for (a) sand 5, (b) sand 4 and (c) sand 3 particles for different bulk solids concentrations compared with the data of Salomon (1965).

The particle size effect on granular temperature is illustrated in Figure 5.15. For sand particles of larger size, an increase in the granular temperature is observed at the bottom of the channel. The top of the channel shows the opposite behaviour, but it may not be as important since the concentration of particles is very low in this region.

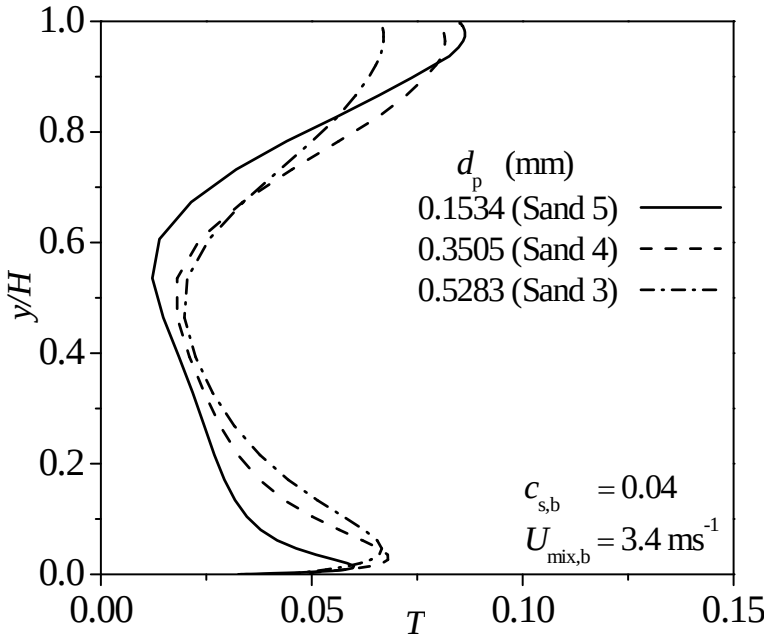

Figure 5.15 Particle size effect on granular temperature

5.5 Turbulence kinetic energy profiles

Figure 5.16 presents predictions of the normalised fluid-phase turbulence kinetic energy, *k* for three types of sand particles for different bulk solids volume fractions and mixture velocities. Single-phase as well as two-phase turbulence kinetic energy predictions are shown for sand 5 particles in Figure 5.16 (a). The turbulence kinetic energy was reduced as particles were added to the flow, especially for high concentration. The one exception is for the bulk solids concentration $c_{s,b} = 0.019$ case, for which *k* was slightly higher than the predicted single-phase flow *k* values near the core region of the channel. The reason for the increase in *k* was due to the additional generation of turbulence which in turn was due to the turbulence modulation term, included in the *k* equation to account for the solids-phase effects on fluid-phase turbulence.

From Figure 5.16 (a) the turbulence kinetic energy profiles peak at $y/H \sim 0.006$ near the bottom wall and $y/H \sim 0.99$ near the top wall for the $c_{s,b} = 0.019$ case. As the bulk solids concentration is increased, the *k* values are reduced and the location of the peak value of *k* moves away from the bottom wall, in a non-linear fashion. With reference to the fluid- and solids-phase velocities, the value of *k* peaks at the location where the mean velocities for both phases cross-away from the bottom wall as shown in Figure 5.8. The peak near the top wall in the upper half of the channel remains unchanged even with an increase in bulk solids concentration. As the bulk solids concentration increased, the maximum concentration in the near-wall region moves closer to the bottom wall (Figure 5.2 - Figure 5.7). For the dense particle region close to the bottom wall, the inter-particle spacing is less and the particles suppress turbulence. Therefore, as the bulk solids

concentration is increased, the turbulence in the fluid-phase was observed to reduce. However, the behaviour of *k* is different at the top wall. At the top of the channel, as the concentration increased, the turbulence level also increased, but not for all particle sizes. When particles of larger size are considered, a different behaviour was observed, i.e. the turbulence first decreased with increasing concentration and then increased with a further increase in concentration as shown in Figure 5.16 (c). The reason for this behaviour can be attributed to turbulence modulation.

Another interesting behaviour observed in Figure 5.16 relates to the peak values. The value of *k* near the bottom of the channel is larger for the case where the mean solids volume fraction is less, but as the bulk solids concentration increases, a relatively denser mixture flows in the region close to the bottom wall and the fluid-phase turbulence is attenuated. In contrast *k* values at the top wall remain unchanged, since, even with increasing bulk solids concentration, the local solids concentration in the region close to the top wall does not change significantly.

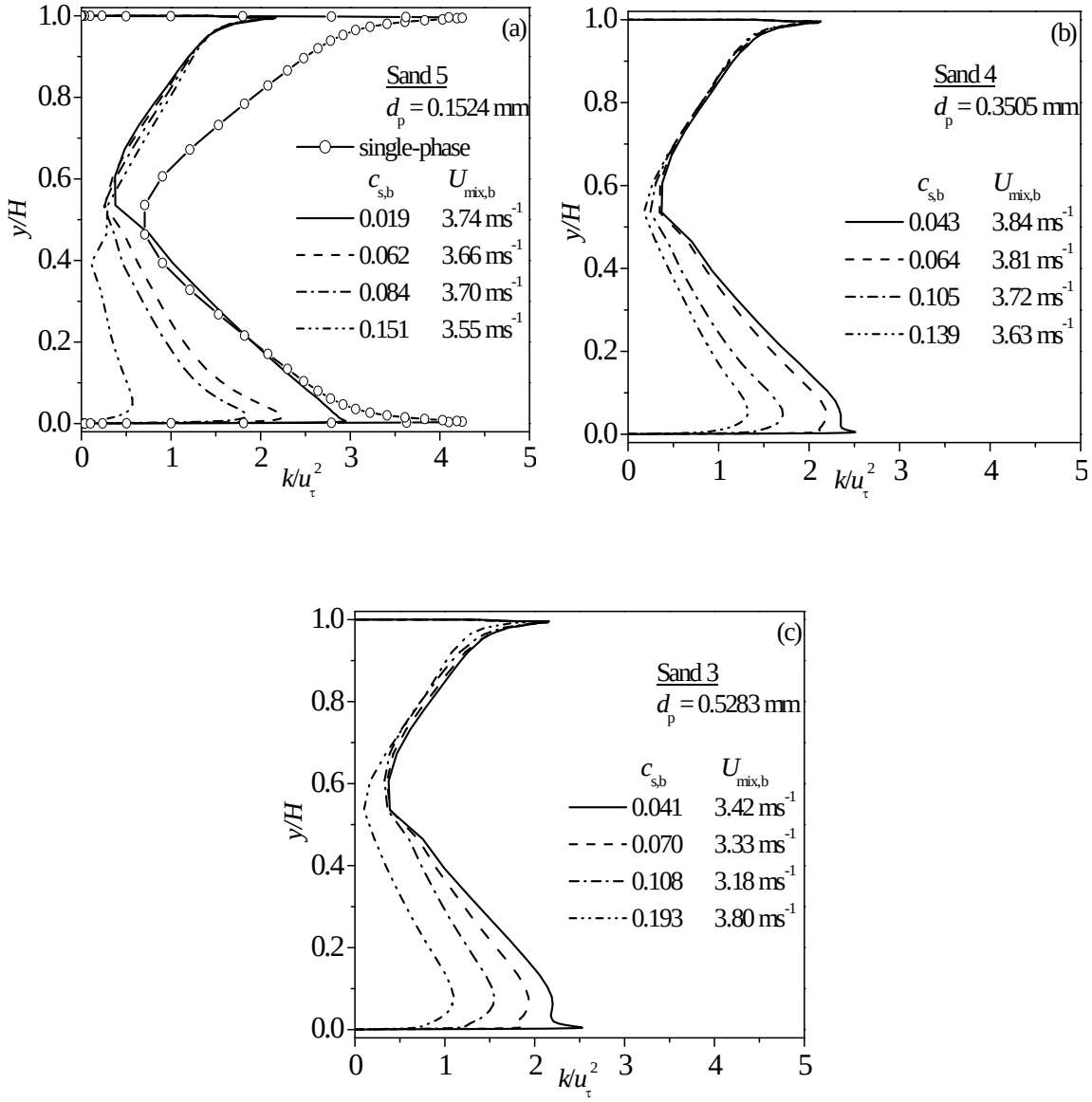

Figure 5.16 Fluid-phase turbulence kinetic energy profiles for (a) sand 5, (b) sand 4 and (c) sand 3 particles for different bulk solids concentrations.

The behaviour of *k* with increasing particle size is shown in Figure 5.17. Here particles of three different sizes are considered for a mean solids concentration and mixture velocity of about 0.04 and 3.4 ms^{-1}, respectively. The turbulence kinetic energy was observed to increase with increasing particle size (from sand 5 to sand 4), but the increase in *k* from sand 4 to sand 3 is much lower. Also, the behaviour of *k* is similar to that of the particle-turbulence interaction closure; the figure pertaining to the behaviour of the closure can be referred from *Appendix D*.

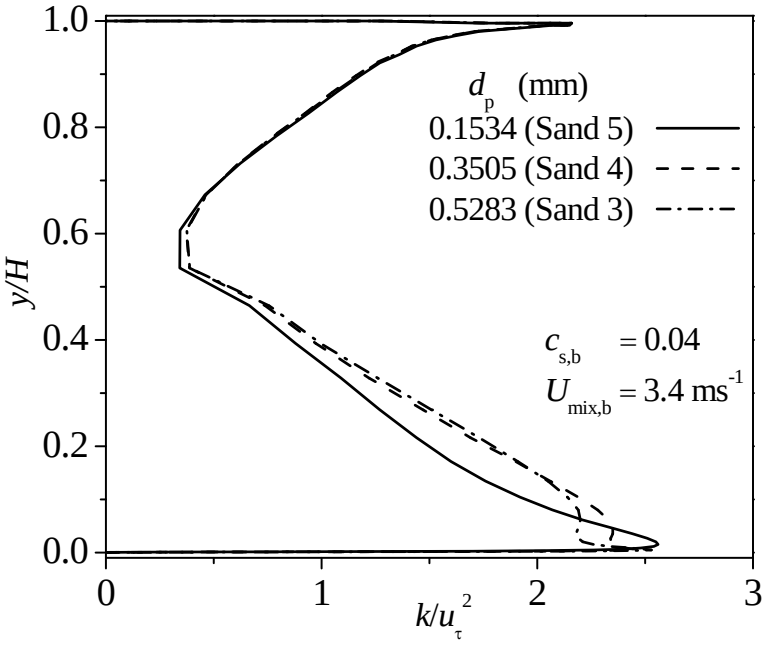

Figure 5.17 Particle size effect on turbulence kinetic energy

5.6 Eddy viscosity profiles

The eddy viscosity profiles for sand 5 particles for different bulk solids concentrations are shown in Figure 5.18, together with single-phase flow predictions. When solid particles of bulk solids concentration $c_{s,b} = 0.019$ are added to a single-phase flow, the eddy viscosity increases in the bottom half of the channel. When the bulk solids concentration is further increased, the eddy viscosity reduces in the bottom half. For the highest bulk solids concentration of $c_{s,b} = 0.151$, the eddy viscosity is uniformly small throughout the lower half of the channel. This suggests that the velocity profile in the bottom half of the channel for this case may be laminar. In the top half, the trend is different. The eddy viscosity for the $c_{s,b} = 0.019$ is the least which then increases as $c_{s,b}$ increases. This behaviour is an artefact of the turbulence kinetic energy which follows a similar trend (Figure 5.16 a).

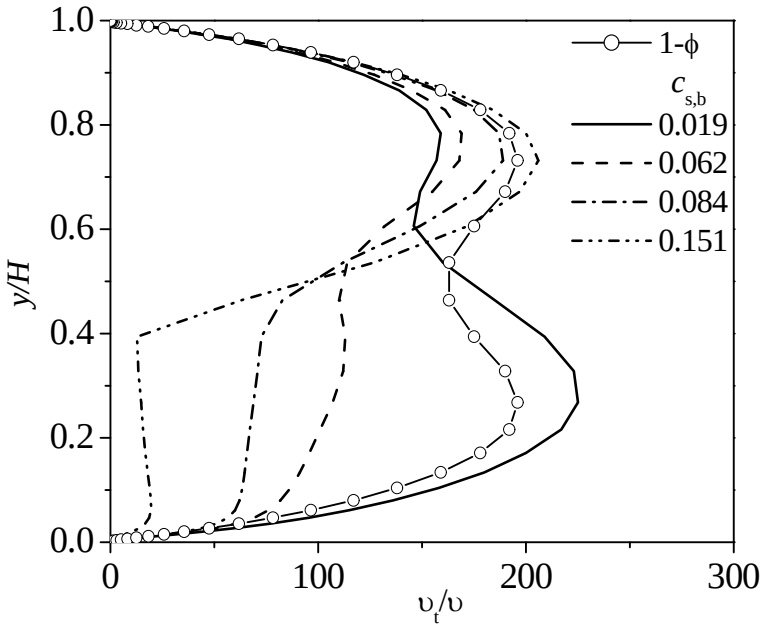

Figure 5.18 Fluid-phase eddy viscosity profiles for single-phase and sand 5 particles for different bulk solids concentrations.

6 CONCLUSIONS AND FUTURE WORK

Summary

This thesis reports two-phase flow predictions for gas-solid and liquid-solid flows in vertical pipes and horizontal channels. The two-fluid gas-solid flow model of Bolio *et al*. (1995), developed for dilute turbulent gas-solid flows in vertical pipes, was employed to investigate gas-solid and liquid-solid flows in a vertical pipe and liquid-solid flows in a horizontal channel. The solids phase model included inter-particle and particle-wall collisions, and was based on the kinetic theory of granular flows.

6.1 Conclusions

Gas-solid flow predictions in a vertical pipe

The mean velocity profiles for both phases were in close agreement and within 10% of the experimental data, but a noticeably narrower near-wall region was evident in the gas-phase velocity predictions compared to the data. There were no data available to evaluate the solids phase volume fraction predictions. The numerical results for the axial gas velocity fluctuations significantly under-predicted the turbulence intensity data. The solids velocity fluctuations were in reasonable agreement with the data at lower mass loadings, while at higher mass loadings, the numerical results slightly over predicted the data.

The turbulent two-fluid gas-solid flow model of Bolio *et al*. (1995) did a reasonable job with the pressure drop predictions. The effects of Reynolds number, mass loading and particle size on the pressure drop predictions were investigated and it was found that the model predictions followed the trend shown by both the data and an empirical correlation and were within a range of 10% of the data. The particle size effects on the pressure drop at Re = 15,100 compared well with the data but the predictions at Re = 20400 showed a slightly different trend. The predicted pressure drop initially decreased with increasing particle size and then started increasing unlike the experimental pressure drop data which increased with increasing particle size. The predictions of Hadinoto *et al*. (2004) also showed behaviour similar to that of the model predictions. The reason for this behaviour is not clear and further investigation in this regard is needed.

Liquid-solid flow predictions in a vertical pipe

Liquid-solid flow with inter-particle and particle-wall interactions was investigated using the turbulent gas-solid flow model of Bolio *et al*. (1995) and the particle-turbulence interaction closure of Sinclair and Mallo (1998). The numerical predictions were compared with the experimental data of Alejbegovic *et al*. (1994) for bulk solids concentrations in the range of 0.04 and Sumner *et al*. (1990) for bulk concentrations of above 0.10. The mean solids velocity and liquid turbulence kinetic energy predictions were in excellent agreement with the experimental data of Alejbegovic *et al*. (1994), while the solids concentration profiles failed to show a reasonable agreement with the data. The granular temperature predictions followed the trend shown by experimental data but over-predicted the measurements.

The model predictions for the cases where the solids concentrations were of the order of 10 – 40% were compared with the experimental data of Sumner *et al*. (1990). Excellent agreement was found between the data and the solids velocity predictions. The model predictions for the solids concentration did not match the experimental data.

The pressure gradient predictions were investigated for particles of different size and concentration in vertical pipes of two different diameters, and the simulation results were compared with the experimental data of Shook and Bartosik (1994). The predictions for coarse sand particles and PVC granules were not in agreement with the data. The predictions were significantly over predicted and exhibited a different slope (with respect to the mixture velocity). The simulated frictional head loss results for the 2.80 mm polystyrene particles, however, were in better agreement with the data (with respect to the mixture velocity). The data and predictions for the frictional head loss, i_m showed an increase in their values with increasing mixture velocity, particle concentration and density. The simulations showed a non-linear relation between the solids-phase wall shear stress and concentration.

The present model formulation (of Bolio *et al*., 1995) was used to predict pressure gradient for mean solids concentrations as high as 50%. However, the model significantly over predicted the data for the cases where the solids-phase density was much higher than that of water (liquid-phase). The model employed in this investigation is typically used for analysing dilute turbulent gas-solid flows. Hence, further investigation of the source terms and closures is needed to improve the predictions for

the liquid-solid flow case. The model of Hadinoto *et al*. (2004), which accounts for the interstitial fluid effects, may improve the liquid-solid flow predictions.

Horizontal channel flow case

Preliminary simulations for horizontal channel flow for particles with different sizes and densities were reported in this thesis. The model constants and closures used in the analysis of dilute vertical gas-solid flow proposed by Bolio *et al*. (1995) were used in this application. Mixture velocity and solids volume fraction profiles were compared with the experimental data of Salomon (1965). The mean mixture velocity profiles were in generally good agreement with the experimental data but the solids volume fraction profiles exhibited some differences.

Other flow parameters such as the mean velocity profiles for both phases, turbulence kinetic energy, granular temperature, eddy viscosity, etc. were also analysed. The behaviour of these parameters provided some insight into the physics of the flow for the horizontal channel flow case.

Overall, the dilute turbulent gas-solid flow model of Bolio *et al*. (1995) did a reasonable job with liquid-solid flow predictions for both vertical pipe and horizontal channel flow cases when mean velocities were predicted, but the model failed to predict solids concentration profiles that matched the experimental data. The model was found to be deficient when liquid-solid flows were investigated, and hence additional modelling work needs to be done to improve the predictions.

6.2 Future work

Numerical two-fluid models for gas-solid and liquid-solid flows were investigated, and the mean and fluctuating velocities, solids concentration, and pressure drop were predicted. Based on the comparisons with experimental data, the first step is to work on model improvement which includes solids concentration, pressure gradient and the fluctuating velocity predictions. Further, the following research is also proposed to improve predictions for liquid-solid flows:

1. The solids radial balance equation, which responds to *T*, is used to calculate solids concentration, c_s, for fully-developed flow in this work. The physics involved with this equation needs to be explored further.
2. Models for turbulence modulation that include both augmentation and attenuation should be explored.
3. The two-fluid model should be modified to include the effects of interstitial fluid.
4. An extensive study of horizontal channel flow should be performed to investigate the solids concentration predictions including the bed effects, eddy viscosity distribution and wall shear stress for both phases. The present study evaluated the model predictions with the data of Salomon (1965) where the local measurements were missing.
5. A thorough literature review should be performed to identify if any experimental data are available for (a) solids concentration for gas-solid flows, (b) fluctuating velocity for liquid and solid phases for a liquid-solid flow in both a vertical pipe and a horizontal channel for dense flows and (c) pressure drop for horizontal

liquid-solid flows. The present work focussed mainly on Sinclair's group and has not used the major review papers of other groups.

6. Finally, the effect of wall roughness on various flow parameters and fluid-solid flows that includes particles of different diameters and shapes in the flow at the same time should also be investigated.

REFERENCES

Alejbegovic, A., A. Assad, F. Bonetto and R.T. Lahey, Jr. Phase distribution and turbulence structure for solid/fluid upflow in a pipe. *Int. J. Multiphase Flow*, 20 (3): 453–459, 1994.

Anderson, T. and R. Jackson. Fluid mechanical description of fluidized beds: comparison with theory and experiment. *I & EC Fund.*, 6: 527–539, 1967.

Bohnet, M. and O. Triesch. Influence of particles on fluid turbulence in pipe and diffuser gas-solid flows. *Chem. Eng. Technol.*, 26: 1254–1261, 2003.

Bolio, E.J. and J.L. Sinclair. Gas turbulence modulation in the pneumatic conveying of massive particles in vertical tubes. *Int. J. Multiphase Flow*, 21 (6): 985–1001, 1995.

Bolio, E.J., J.A. Yasuna, and J.L. Sinclair. Dilute turbulent gas-solid flow in risers and particle-particle interactions. *AIChE Journal*, 41 (6): 1375–1388, 1995.

Cao, J. and G. Ahmadi. Gas-particle two-phase turbulent flow in a vertical duct. *Int. J. Multiphase Flow*, 21 (6): 1203–1228, 1995.

Comer Jr., J.K. Computational two-phase flow analyses and applications to gas-liquid and gas-solid flows. PhD. *Diss., North Carolina State University*, North Carolina, 1998.

Crowe, C.T. On models for turbulence modulation in fluid-particle flows. *Int. J. Multiphase Flow*, 26: 719–727, 2000.

Ding, J., R.W. Lyczkowski, W.T. Sha, S.A. Altobelli and E. Fukushima. Numerical analysis of liquid-solids suspension velocity and concentrations obtained by NMR imaging. *Powder Tech.*, 77: 301–312, 1993.

Elgobashi, S. Particle-laden turbulent flows: direct simulation and closure models. *Appl. Scientific Res.*, 48: 301–314, 1991.

Elgobashi, S. and T. Abou-Arab. A two-equation turbulence model for two-phase flows. *Phys. Fluids*, 26 (4): 931–938, 1983.

Gore, R.A. and C.T. Crowe. Effect of particle size on modulating turbulent intensity. *Int. J. Multiphase Flow*, 15 (2): 279–285, 1989.

Hadinoto, K. and J.S. Curtis. Effect of interstitial fluid on particle-particle interactions in kinetic theory approach of dilute turbulent fluid-solid flow. *Ind. Eng. Chem. Res.*, 43: 3604–3615, 2004.

Henthorn, K.H., K. Park and J.S. Curtis. Measurement and prediction of pressure drop in pneumatic conveying: Effect of particle characteristics, mass loading, and Reynolds number. *Ind. Eng. Chem. Res.*, 44: 5090–5098, 2005.

Hrenya, C.M., E.J. Bolio, D. Chakrabarti and J.L. Sinclair. Comparison of low Reynolds number $k-\varepsilon$ turbulence models in predicting fully developed pipe flow. *Chem. Engr. Science*, 50 (12): 1923–1941, 1995.

Hui, K., P. Haff, J. Ungar and R. Jackson. Boundary conditions for high shear grain flows. *J. Fluid Mech.*, 145: 223–238, 1984.

Johnson, P. and R. Jackson. Frictional-collisional constitutive relations for granular materials, with application to plane shearing. *J. Fluid Mech.*, 176: 67–93, 1987.

Kenning, V.M. and C.T. Crowe. On the effect of particle on carrier phase turbulence in gas-solid flow. *Int. J. Multiphase Flow*, 23 (2): 403–408, 1997.

Koch, D. Kinetic theory for a monodisperse gas-solid suspension. *Phys. Fluid A*, 2: 1711 – 1723, 1990.

Konno, H. and S. Saito. Pneumatic conveying of solids through straight pipes. *Journal of Chem. Eng. Jpn.*, 2 (2): 211–217, 1969.

Krampa-Morlu, F.N., D.J. Bergstrom, J.D. Bugg, R.S. Sanders and J. Schaan. Numerical simulation of dense coarse particle slurry flows in a vertical pipe. *5th International Conference on Multiphase Flow, ICMF'04*, Yokohama, Japan. 1–14, May 31-June 3, 2004.

Krampa-Morlu, F.N., A.K. Yerrumshetty, D.J. Bergstrom, J.D. Bugg, R.S. Sanders and J. Schaan. A study of turbulence modulation models for gas-particle flows. *5th International Symposium on Turbulence, Heat & Mass Transfer*, Dubrovnik, Croatia, September 25–29, 2006.

Lee, S. and F. Durst. On the motion of particles in turbulent duct flows. *Int. J. Multiphase Flow*, 8: 125–146, 1982.

Louge, M.Y., E. Mastorakos and J.T. Jenkins. The role of particle collisions in pneumatic transport. *J. Fluid Mech.*, 231: 345–359, 1991.

Lun, C.K.K, S.B. Savage, D.J. Jeffrey and N. Chepurniy. Kinetic theories for granular flow: inelastic particles in Couette flow and slightly inelastic particles in a general flow field. *J. Fluid Mech.*, 140: 223–256, 1984.

Matousek, V. Pressure drops and flow patterns in sand-mixture pipes. *Exp. Thermal and Fluid Science*, 26: 693–702, 2002.

Myong, H.K. and N. Kasagi. A new approach to the improvement of turbulence model for wall-bounded shear flows. *JSME Int. J.* (Series II), 33 (1): 63–72, 1990.

Nagano, Y. and M. Tagawa. An Improved Model for Boundary Layer Flows. *ASME, J. Fluids Engr.*, 112: 33–39, 1990.

Nieuwland, J.J., E. Delnoij, J.A.M. Kuipers, W.P.M. van Swaaij. An engineering model for dilute riser flow. *Powder Tech.*, 90: 115–123, 1997.

Patankar, S.V. *Numerical Heat Transfer and Fluid Flow*. Hemisphere Publishing Corporation, New York, 1980.

Plasynski, S., G. Klinzing, and M. Mathur. High-pressure vertical pneumatic transport investigation. *Powder Tech.*, 79: 95–109, 1994.

Rimon, Y. and S.I. Cheng. Numerical solution of a uniform flow over a sphere at intermediate Reynolds numbers. *Phys. Fluids*, 12 (5): 949–959, 1969.

Salomon, D.M. Flow of suspensions in a rectangular channel. Ph.D. Diss., University of Saskatchewan, 1965.

Sheen, H.-J., Y.-Z. Chang and Y.-S. Chinag. Two-dimensional measurements of flow structures in a two-phase vertical pipe flow. *Proc. Natl. Sci. Counc. ROC (A)*, 17: 200–213, 1993.

Shook, C.A. and A.S. Bartosik. Particle-wall stresses in vertical slurry flows. *Powder Tech.*, 81: 117–124, 1994.

Sinclair, J.L. Vertical transport of gas and solids with radial solid density variations. Ph.D. Diss., Princeton Uni., 1989.

Sinclair J.L. and R. Jackson. Gas-particle flow in a vertical pipe with particle-particle interactions. *AIChE Journal*, 35: 1473–1486, 1989.

Sinclair J.L. and T. Mallo. Describing particle-turbulence interaction in a two-fluid modeling framework. *Proc. of ASME Fluids Engineering Division Summer Meeting (FEDSM'98)*, Washington, DC, June 21–25, 1998.

Singh, B. Analysis of pressure drop in the vertical pneumatic conveying. Generalized approach for gas-particle and liquid-particle systems. *Powder Tech.*, 32: 179–181, 1982.

Sumner, R.J., M.J. McKibben and C.A. Shook. Concentration and velocity distributions in turbulent vertical slurry flows. *Ecoulements Solide Liquide*, 2 (2): 33–42, 1990.

Tsuji, Y., Y. Morikawa and H. Shiomi. LDV measurement of an air-solid two-phase flow in a vertical pipe. *J. Fluid Mech.*, 139: 417–434, 1984.

Wang, F.-J., J.-X. Zhu and J.M. Beeckmans. Pressure gradient and particle adhesion in the pneumatic transport of cohesive fine powders. *Int. J. Multiphase Flow*, 26: 245–265, 2000.

Wilcox, D. C. Turbulence modeling for CFD. *La Canada, Calif.: DCW Industries*, 2002.

Yuan, Z. and E.E. Michaelides. Turbulence modulation in particulate flows - A theoretical approach. *Int. J. Multiphase Flow*, 18 (5): 779–785, 1992.

Zhang, Y. and J.M. Reese. Particle-gas turbulence interactions in a kinetic theory approach to granular flows. *Int. J. Multiphase Flow*, 27: 1945–1964, 2001.

Zhang, Y. and J.M. Reese. Gas turbulence modulation in a two-fluid model for gas-solid flows. *AIChE Journal*, 49 (12): 3048–3065, 2003.

APPENDIX A

Discretization of momentum equations:

This section presents the solution method for the momentum equations using the finite volume technique of Patankar (1980). The axial momentum equation for the fluid phase has been solved in the model as follows:

$$\underbrace{\frac{\partial(\rho_f u_f)}{\partial t}}_{1} = \underbrace{\frac{1}{r}\frac{\partial}{\partial r}\left(r\mu_{eff}\frac{\partial u_f}{\partial r}\right)}_{2} - \underbrace{\frac{\partial p}{\partial z} - \beta(u_f - u_s)}_{3} \qquad \text{(A.1)}$$

where 1 is the pseudo-transient part, 2 is the diffusion part and 3 is the source term. Following Patankar (1980), the discretized form of the above equation is obtained by integrating both sides by volume, v, and time, t.

$$1 \Rightarrow \int_{\Delta v}\int_{\Delta t}\frac{\partial(\rho_f u_f)}{\partial t}dt\,dv = \rho_f(u_f - u_f^o)\Delta v$$

$$= \int_{\Delta v}\int_{\Delta t}\frac{\partial(\rho_f u_f)}{\partial t}dt\,dv = \rho_f(u_f - u_f^o)\frac{\Delta v}{\Delta t}$$

The above equation (left hand side of eq. A.1) was divided by time since all the terms on the right hand side of equation A.1 will have this term (after discretization) and by doing this the repetitive use of this term can be avoided.

$$2 \Rightarrow \int_{\Delta v}\frac{1}{r}\frac{\partial}{\partial r}\left(r\mu_{eff}\frac{\partial u_f}{\partial r}\right)dv = \int_w^e \frac{1}{r}\frac{\partial}{\partial r}\left(r\mu_{eff}\frac{\partial u_f}{\partial r}\right)rdr = r\mu_{eff}\frac{\partial u_f}{\partial r}\Big|_w^e$$

$$= r_e\mu_e\left(\frac{u_e - u_p}{\Delta r_e}\right) - r_w\mu_w\left(\frac{u_p - u_w}{\Delta r_w}\right)$$

$$= \frac{r_e\mu_e}{\Delta r_e}u_e + \frac{r_w\mu_w}{\Delta r_w}u_w - \left(\frac{r_e\mu_e}{\Delta r_e} + \frac{r_w\mu_w}{\Delta r_w}\right)u_p$$

$$3 \Rightarrow \int_{\Delta v} s \, dv = (s_u + s_p \phi_p) \Delta v$$

$$\int_{\Delta v} \left(-\beta (u_f - u_s) - \frac{\partial p}{\partial z} \right) dv$$

$$s_u = \beta u_s - \frac{\partial p}{\partial z} \quad \& \quad s_p = -\beta$$

By substituting the discretized equations for all terms in equation A.1, we have

$$\rho_f (u_f - u_f^o) \frac{\Delta v}{\Delta t} = \frac{r_e \mu_e}{\Delta r_e} u_e + \frac{r_w \mu_w}{\Delta r_w} u_w - \left(\frac{r_e \mu_e}{\Delta r_e} + \frac{r_w \mu_w}{\Delta r_w} \right) u_p + \left(\beta u_s - \frac{\partial p}{\partial z} - \beta u_{fp} \right) \Delta v$$

$$\left(\rho_f \frac{\Delta v}{\Delta t} + \frac{r_e \mu_e}{\Delta r_e} + \frac{r_w \mu_w}{\Delta r_w} + \beta \Delta v \right) u_{fp} = \frac{r_e \mu_e}{\Delta r_e} u_{fe} + \frac{r_w \mu_w}{\Delta r_w} u_{fw} + \rho_f \frac{\Delta v}{\Delta t} u_{fp}^o + \left(\beta u_{sp} - \frac{\partial p}{\partial z} \right) \Delta v$$

$$a_e = \frac{r_e \mu_e}{\Delta r_e}, \; a_w = \frac{r_w \mu_w}{\Delta r_w}, \; a_p^o = \rho_f \frac{\Delta v}{\Delta t}, \; s_u = \beta u_{sp} - \frac{\partial p}{\partial z}, \; s_p = -\beta$$

$$a_p = a_e + a_w + a_p^o - s_p$$

The momentum equations for the fluid-phase turbulence kinetic energy and its dissipation, solids-phase axial balance and granular temperature are all solved in a similar way.

Radial balance equation:

The solids-phase momentum balance in the radial direction used to calculate solids concentration is in the form of an algebraic equation. This equation is solved using

Newton-Raphson method for obtaining solids concentration. The solids-phase radial balance equation is given as follows:

$$\frac{1}{r}\frac{\partial}{\partial r}(r\sigma_{rr}) - \frac{\sigma_{\theta\theta}}{r} = 0 \tag{A.2}$$

$$\Rightarrow \frac{1}{r}\left[r\frac{\partial \sigma_{rr}}{\partial r} + \sigma_{rr} \right] - \frac{\sigma_{\theta\theta}}{r} = 0$$

$$\sigma_{rr} = \sigma_{\theta\theta}, \ \therefore \frac{\partial \sigma_{rr}}{\partial r} = 0$$

Integrating both sides and substituting the expression for σ_{rr}

$$\int \frac{\partial \sigma_{rr}}{\partial r} dr = \int 0 \, dr$$

$$\int \frac{\partial}{\partial r}\left[\rho_s c_s T\left(w + 4\eta c_s g_0\right)\right] dr = 0$$

$$\rho_s \int \frac{\partial}{\partial r}\left[c_s T\left(w + 4\eta c_s g_0\right)\right] dr = 0$$

$$\rho_s \neq 0; \int \frac{\partial}{\partial r}\left[c_s T\left(w + 4\eta c_s g_0\right)\right] dr = 0$$

$$c_s T\left(w + 4\eta c_s g_0\right) = I_c \tag{A.2.1}$$

Solve using Newton-Raphson method.

Step 1: Let $g_7 = wc_s + 4\eta c_s^2 g_0$

and $dg_7 = wd(c_s) + c_s d(w) + 4\eta\left(c_s^2 d(g_0) + g_0 d\left(c_s^2\right)\right)$

$$F = g_7 * T - I_c$$

$$F' = dg_7 * T$$

$$c_s^n = c_s - \text{wf} * \frac{F}{F'}$$

where wf is the weight function. In this work, wf = 0.7.

$$\text{If}\left[Abs\left(\frac{c_s^n - c_s}{c_s} \right) > 10^{-6} \right] \text{then} \quad c_s = c_s^n \quad \text{go to Step 1}$$

$$\text{else } c_s = c_s^n$$

For a horizontal flow, the weight of the particles also features in the radial balance equation, which is shown as follows:

$$\frac{\partial \sigma_{yy}}{\partial y} - \rho_s c_s g = 0 \tag{A.3}$$

Let $\sigma_{yy} \left(= \rho_s c_s \left(w + 4\eta c_s g_0\right) T\right) = f \Rightarrow \frac{\partial f}{\partial y} = \rho_s c_s g$

The solids mean concentration, c_s, is known at the first node in the near-wall region of the top wall ($y_1 = H - y_{ie}$) of the channel, since c_s at the top wall is used as an input to the flow. Therefore, f and $\frac{\partial f}{\partial y}$ are known at the first node. Using Taylor's series approximation, f at the remaining nodes is calculated as follows:

$$f\left(y_1 + y_2\right) = f\left(y_1\right) + \left.\frac{\partial f}{\partial y}\right|_{y=y_1} * y_2 \tag{A.3.1}$$

In the above equation, $y_2 \left(= y_{ie} - y_{ie-1}\right)$ is the distance between the first and the second node from the top wall, and is a known value.

In the equation (A.3.1), $f(y_1)$, $\left.\frac{\partial f}{\partial y}\right|_{y=y_1}$ and y_2 are known. Therefore, equation (A.3.1) takes the form of equation (A.2.1) and the solids concentration at y_2 is calculated using the solution technique similar to the one employed to calculate solids concentration for the vertical pipe flow case. Using the value of solids concentration at y_2, c_s at y_3 is calculated which is then used to find out c_s at y_4, and so on.

Boundary conditions

This section provides the details of the implementation of boundary conditions for the solids mean velocity and granular temperature in this work.

Solids velocity:

$$\frac{\rho_s \pi u_s \phi \sqrt{T}}{2\sqrt{3}\left(\frac{C_o}{c_s} - \left(\frac{C_o}{c_s}\right)^{2/3}\right)} = -\frac{5\sqrt{\pi} d_p \rho_s \sqrt{T}}{96}(w g_1 + g_2)\frac{\partial u_s}{\partial r}$$

$$\left.\frac{\partial u_s}{\partial r}\right|_{wall} = -\frac{16\sqrt{3}\phi}{5 d_p (w g_1 + g_2)_{wall}} \cdot \frac{1}{\left.\left(\frac{C_o}{c_s} - \left(\frac{C_o}{c_s}\right)^{2/3}\right)\right|_{wall}} \cdot u_s|_{wall}$$

$$\text{let, } B_{sv} = \frac{16\sqrt{3}\phi}{5 d_p (w g_1 + g_2)_{wall}} \cdot \frac{1}{\left.\left(\frac{C_o}{c_s} - \left(\frac{C_o}{c_s}\right)^{2/3}\right)\right|_{wall}} \text{ and } v = u_s$$

$$\left.\frac{\partial v}{\partial r}\right|_{wall} = -B_{sv} \cdot v\big|_{wall} \Rightarrow \quad \frac{v_E - v_P}{\Delta r_e - \Delta r_p} = -B_{sv}\left(\frac{v_E + v_P}{2}\right)$$

It is assumed that the fictitious node is placed at a distance equal to that of the first node but on the other side of the wall. Also, the solids velocity at the fictitious node is assumed to be the same to that at the first node.

$$\frac{v_E - v_P}{-2\Delta r_p} = -B_{sv}\left(\frac{v_E + v_P}{2}\right) \Rightarrow (1 + B_{sv})v_P = (1 - B_{sv})v_E$$

$$a_P = 1 + B_{sv}\Delta r_p,\ a_E = 1 - B_{sv}\Delta r_p,\ b = 0$$

Granular temperature:

$$-\frac{25\sqrt{\pi} d_p \rho_s \sqrt{T}}{128}(wg_3 + g_4)\left.\frac{\partial T}{\partial r}\right|_{wall} = \left(\frac{\sqrt{3}\rho_s \pi (1 - e_w^2) T^{3/2}}{4} - \frac{\rho_s \pi u_s^2 \phi \sqrt{T}}{2\sqrt{3}}\right)\Bigg|_{wall} * \frac{1}{\left(\frac{C_o}{c_s} - \left(\frac{C_o}{c_s}\right)^{2/3}\right)\Big|_{wall}}$$

$$\left.\frac{\partial T}{\partial r}\right|_{wall} = -B_{st}T + C_{st}$$

where $B_{st} = \dfrac{64\sqrt{3\pi}(1 - e_w^2)}{50 d_p (wg_3 + g_4)} \cdot \dfrac{1}{\left(\frac{C_o}{c_s} - \left(\frac{C_o}{c_s}\right)^{2/3}\right)}$ and

$$C_{st} = \frac{64\sqrt{\pi}\phi u_s^2}{25\sqrt{3} d_p (wg_3 + g_4)} \cdot \frac{1}{\left(\frac{C_o}{c_s} - \left(\frac{C_o}{c_s}\right)^{2/3}\right)}$$

$$\frac{T_E - T_P}{-2\Delta r_P} = -B_{st}\left(\frac{T_E + T_P}{2}\right) + C_{st} \Rightarrow (1 + B_{st}\Delta r_P)T_P = (1 - B_{st}\Delta r_P)T_E + 2C_{st}\Delta r_P$$

$$a_P = 1 + B_{st}\Delta r_p,\ a_E = 1 - B_{st}\Delta r_p,\ b = 2C_{st}\Delta r_p$$

APPENDIX B

Grid Sensitivity

The following figures depict that the algorithm used in this work was not sensitive to the number of grids used. The algorithm was tested for a gas-solid flow with 200 µm glass particles at a mass loading of 1.0 and Reynolds number of 39,600. The mean velocity profiles for both phases and solids concentration profiles for the cases where the number of control volumes were 60 and 100 were exactly similar proving that the model is grid insensitive.

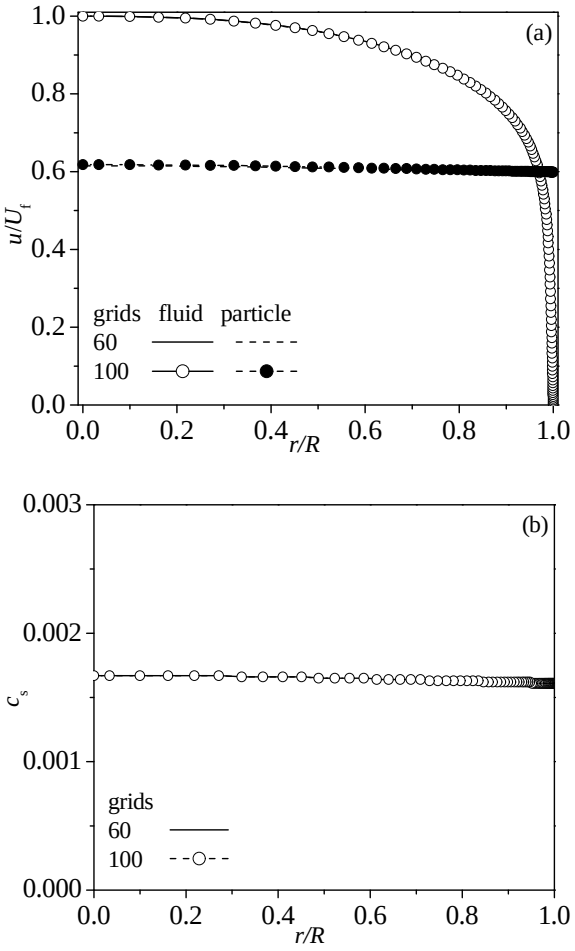

Figure B.1 Grid sensitivity analysis for 200 µm glass particles in a 42 mm glass pipe for (a) Mean velocities for both phases and (b) solids concentration for 60 and 100 control volumes.

APPENDIX C

Liquid-phase axial momentum balance:

This section shows the derivation of momentum equations for the horizontal channel flow in this work. The following figure represents an element of fluid in the channel:

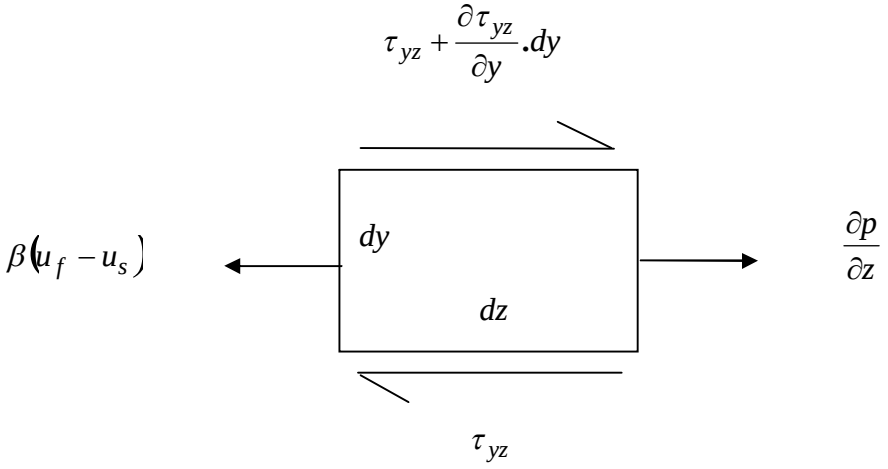

Figure C.1 Force balances on a differential fluid element in a horizontal channel flow

From the above figure, the force balances on the liquid element can be written as follows:

$$\left(\tau_{yz} + \frac{\partial \tau_{yz}}{\partial y} dy\right) dz + \frac{\partial p}{\partial z} dydz - \tau_{yz} dz - \beta\left(u_f - u_s\right) dydz = 0 \qquad \text{(C.1)}$$

Simplifying eq. (C.1), the momentum balance for the liquid-phase in the axial direction is derived and is given as follows:

$$0 = \frac{\partial \tau_{yz}}{\partial y} - \frac{\partial p}{\partial z} - \beta\left(u_f - u_s\right) \qquad \text{(C.2)}$$

The momentum equation for the solids phase in the axial direction is also derived in a similar fashion. The final form of the equation is as follows:

$$0 = \frac{\partial \sigma_{yz}}{\partial y} + \beta \left(u_f - u_s \right) \tag{C.3}$$

Solids-phase radial momentum balance:

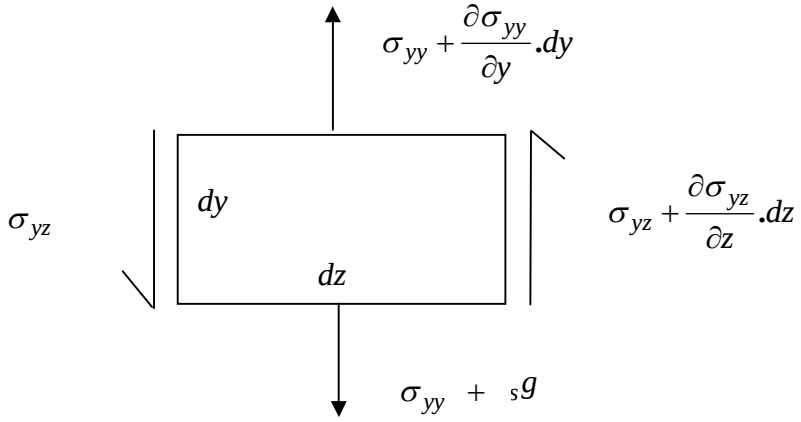

Figure C.2 Force balances on a differential solid element in a horizontal flow

The force acting on the differential solid particle can be written as follows:

$$\left(\sigma_y + \frac{\partial \sigma_y}{\partial y} dy \right) dz + \left(\sigma_{yz} + \frac{\partial \sigma_{yz}}{\partial z} dz \right) dy - \sigma_{yz} dy - \sigma_y dz - \rho_s c_s g \, dy dz = 0 \tag{C.4}$$

After simplifications, the radial balance equation is given by the following equation:

$$\frac{\partial \sigma_y}{\partial y} + \frac{\partial \sigma_{yz}}{\partial z} - \rho_s c_s g = 0 \tag{C.5}$$

For a fully developed flow,

$$\frac{\partial \sigma_{yz}}{\partial z} = 0 \tag{C.6}$$

Therefore, the radial balance equation for a fully-developed flow in a horizontal channel is given as follows:

$$\frac{\partial \sigma_y}{\partial y} - \rho_s c_s g = 0 \qquad \text{(C.7)}$$

APPENDIX D

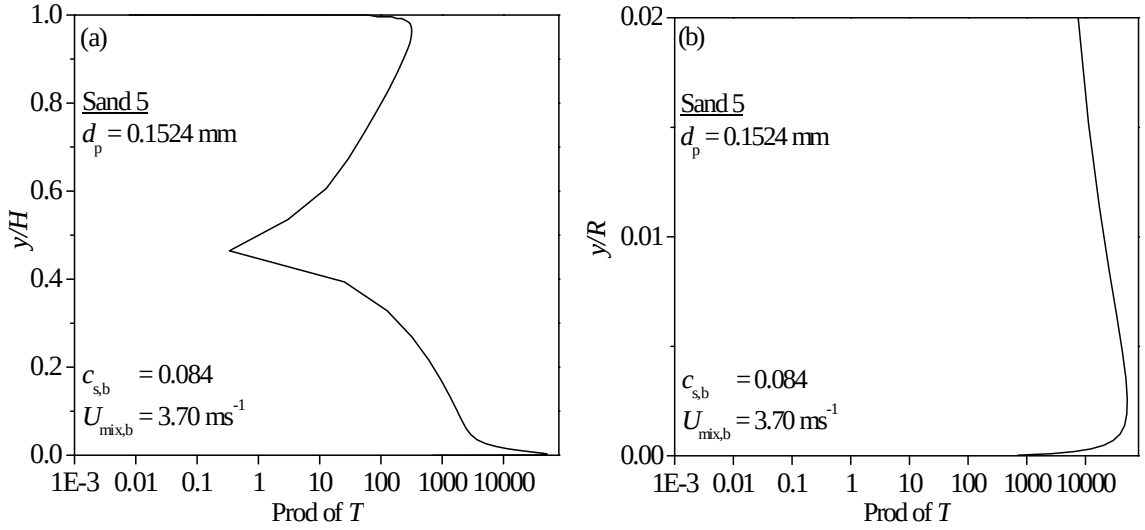

Figure D.1 Production term for the granular temperature for sand 5 particles at a mean solids concentration of 0.084

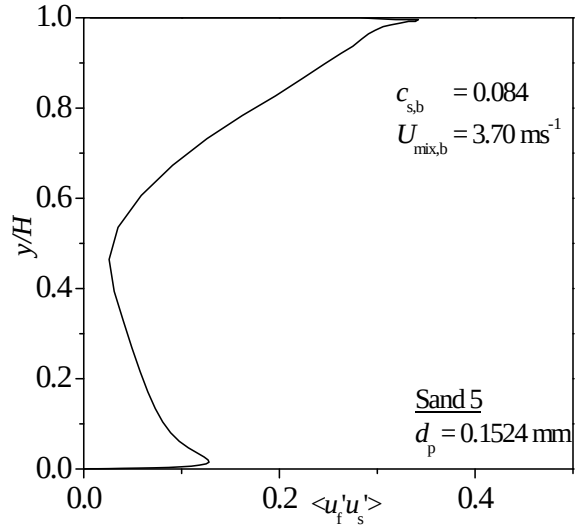

Figure D.2 Particle turbulence interaction closure for sand 5 particles at a mean solid concentration of 0.084